

Technical Report on the Beam Induced Backgrounds in the H1 Detector

H1 background working group

V. Andreev, W. Bartel, J. Bracinik, A. Buniatian, E. Elsen, R. Felst, J. Ferencei, P. Fleischmann, J. Gayler, T. Greenshaw, M. Kapishin, M. Klein, C. Kleinwort, V. Lendermann, S. Levonian, B. List, R. Lopez-Fernandez, L. Lytkin, N. Malden, C. Niebuhr, D. Pitzl, E. Rizvi, A. Schöning, H.-C. Schultz-Coulon, A. Specka, R. Stamen, F. Tomasz, I. Tsurin, K. Urban, P. Van Mechelen, K. Wacker.

Abstract

This report describes studies of the beam induced backgrounds that presently prevent operation of the H1 detector with the design HERA II beam currents. Measurements are presented and compared with Monte Carlo simulations that provide a reasonable description of the backgrounds in H1 arising from synchrotron radiation and proton beam-gas interactions. A detailed evaluation is given of various measures that reduce these backgrounds. Significant improvements require a substantially better vacuum in the region around the H1 interaction region, extending to at least $z \simeq -12$ m.

Contents

1	Introduction	3
1.1	Changes with Respect to Previous Version of Report	3
1.2	Structure of Report	4
1.3	The H1 Detector and Coordinate System	4
1.4	Limits on Chamber Currents and Radiation Doses	5
2	Experimental Investigation of the Backgrounds in H1	6
2.1	Introduction	6
2.2	Dependence of Chamber Currents on Beam Currents	6
2.3	Contribution of Synchrotron Radiation and Positron Beam-Gas Interactions to CJC Current	8
2.4	Effects of Positron Beam on Vacuum in North Right	14
2.5	Vacuum Quality and Proton Induced Background	16
2.6	Positron-Proton Operation	19
2.7	Extrapolation to Design Currents	21
2.8	Summary	21
3	Positron Induced Background	23
3.1	Introduction	23
3.2	Synchrotron Radiation	23
3.3	Backscattering from Absorber 4	23
3.4	Thickness of Collimators C5B and C5A	23
3.5	Backscattering from Collimator C5A	24
3.6	Reducing the Amount and the Effects of Back-Scattered Synchrotron Radiation	27
3.7	Study of Sources of Synchrotron Radiation Entering the CJC	29
3.7.1	Comparison of Contributions of Lost Positrons and Synchrotron Radiation	32
3.7.2	Contributions of Synchrotron Radiation and Lost Positrons to Currents in the CJC	34
3.7.3	Particle and Synchrotron Radiation Induced Background During Electron-Proton Running.	36
3.8	Summary	37

4	Proton Induced Background	39
4.1	Introduction	39
4.2	Data Samples used in Investigation of Proton Beam-Gas Scattering	40
4.3	Monte Carlo Simulation of Beam–Gas Scattering	43
4.3.1	Modelling of Proton–Proton and Proton–Nucleus Interactions	43
4.3.2	The Simulation of Dead Material, Magnetic Fields and the Vertex Distribution	43
4.3.3	Properties of the Primary Interactions	48
4.3.4	Properties of Events Observed in H1	48
4.3.5	Comparison with Earlier Studies	51
4.4	Calculation of the Track Trigger Rate	56
4.4.1	Normalization of the Monte Carlo Samples	56
4.4.2	The Track Trigger Rate	56
4.5	Comparison of Data with Monte Carlo Simulation	57
4.6	Effects of Possible Modifications of the Interaction Region	62
4.6.1	Reducing the Thickness of the C5B Collimator	62
4.6.2	Additional Lead Shielding around the C5B Collimator	62
4.7	An Additional Extended Collimator Inside GG	63
4.7.1	An Additional Collimator C6 at $z = -3.6$ m	64
4.8	Summary and Conclusions on Possible Modifications	64
5	Chemical Composition of the Residual Gas	67
5.1	Introduction	67
5.2	Mass Spectrum of the Residual Gas	67
5.3	Effective Z^2 from Beam-Gas Bremsstrahlung Rates	71
5.4	Summary	75
6	Conclusions	76

1 Introduction

Since the 2000/2001 shutdown, during which the HERA II luminosity upgrade was performed, the operation of HERA has been limited to moderate beam currents because of high backgrounds and difficult beam steering requirements. Severe synchrotron radiation backgrounds were observed in November and December 2001, limiting the positron current to less than 1 mA. Additional collimators upstream of the collider experiments were installed in February and early March 2002, and aperture limitations for the direct synchrotron radiation were removed on the downstream side. Over the following months a positron orbit was established which allowed beam currents of up to 30 mA to be stored with tolerable backgrounds. It then became evident that proton beam-gas background was limiting the tolerable beam currents to about $I_e \cdot I_p < 600 \text{ mA}^2$. This situation was exacerbated by the observed increase in the pressure of the residual gas in the beam pipe with increasing positron current.

Extensive measurements with a variety of beam conditions have been performed to understand the backgrounds arising from synchrotron radiation and from beam-gas interactions. In addition, detailed simulations have been performed, particularly of the proton background. The results of these studies are presented in this report as is an extrapolation to the high HERA II design beam currents of $I_e = 55 \text{ mA}$ and $I_p = 135 \text{ mA}$. A quantitative evaluation of possible remedies is given.

1.1 Changes with Respect to Previous Version of Report

This version of the report differs from that of 25/09/2002 in the following respects:

- Some artifacts introduced into figures 5 and 17 (now 18) by the graphical display program from which they were extracted have been removed.
- A new figure, number 53, has been added to section 4 which strengthens the conclusion that the residual gas in the beam pipe contains a large proportion of heavy elements, such as carbon and oxygen.
- Some re-writing has been done in an attempt to make more clear the conclusions that we draw from the studies presented. The re-writing includes a description of the structure of the report, see below, and the addition of a paragraph summarising each section and pointing out where some of the measurements should be repeated or further studies performed.
- Some typographical errors have been removed.
- Sections 5 and 6 have been amalgamated.
- A brief discussion of a possible proton beam-gas collimator has been added near the end of section 4 of the document, together with a new figure, number 57.

1.2 Structure of Report

The structure of the report is as follows:

- The remainder of this section presents the H1 apparatus and coordinate system and discusses the fundamental limitations on the tolerable background rates arising from the sensitive components of the H1 detector.
- Section 2 discusses the backgrounds observed with positron beams, proton beams and in colliding beam operation, as well as the effects of controlled pressure variations induced by firing titanium sublimation pumps in the region around the H1 apparatus. These observations are used to draw conclusions on the significance of the effects of synchrotron radiation, positron beam-gas interactions and proton induced background on the detector. The background induced by the proton beam is found to be the most significant and first conclusions are drawn on the positions along the proton beam line which, due to poor vacuum conditions, are causing the large backgrounds. An extrapolation to full HERA II currents is made and conclusions drawn on the magnitude of the improvements necessary to allow H1 operation at full HERA II luminosity.
- Section 3 investigates in more detail the backgrounds induced by the positron beam, namely those due to synchrotron radiation and positron beam-gas interactions. The primary sources of backscattered synchrotron radiation are identified and the relative contributions of synchrotron radiation and positron beam-gas interactions to the background extracted. The effects on the synchrotron radiation induced background of a reduction of the thickness of the H1 collimators are discussed, as are the effects of lead shielding designed to protect sensitive regions of the H1 detector. The contributions of synchrotron radiation and positron beam-gas interactions are evaluated at full HERA II beam currents.
- Section 4 contains a discussion of the proton beam induced backgrounds. Monte Carlo simulations are described which provide a good description of the observed backgrounds and which support the conclusions drawn in section 1 regarding the regions of the proton beam line in which poor vacuum is particularly damaging as regards H1 operation. Simulations are also used to investigate the effects on the proton induced background of the abovementioned modifications to the H1 collimation system and lead shielding. Studies are also made of collimation systems designed to protect the detector from proton induced background. Information on the composition of the residual gas in the beam pipe is extracted from comparisons of Monte Carlo with data.
- Section 5 presents two further studies of the composition of the residual gas in the beam pipe. The first uses measurements of the rate of beam-gas bremsstrahlung, the second relies on mass spectrometry.
- Section 6 contains a brief summary of the conclusions of the report.

1.3 The H1 Detector and Coordinate System

Figure 1 shows a schematic side view of the H1 experiment, located at the North IP of HERA, together with the final focus magnets of the electron machine which extend into the H1 Hall.

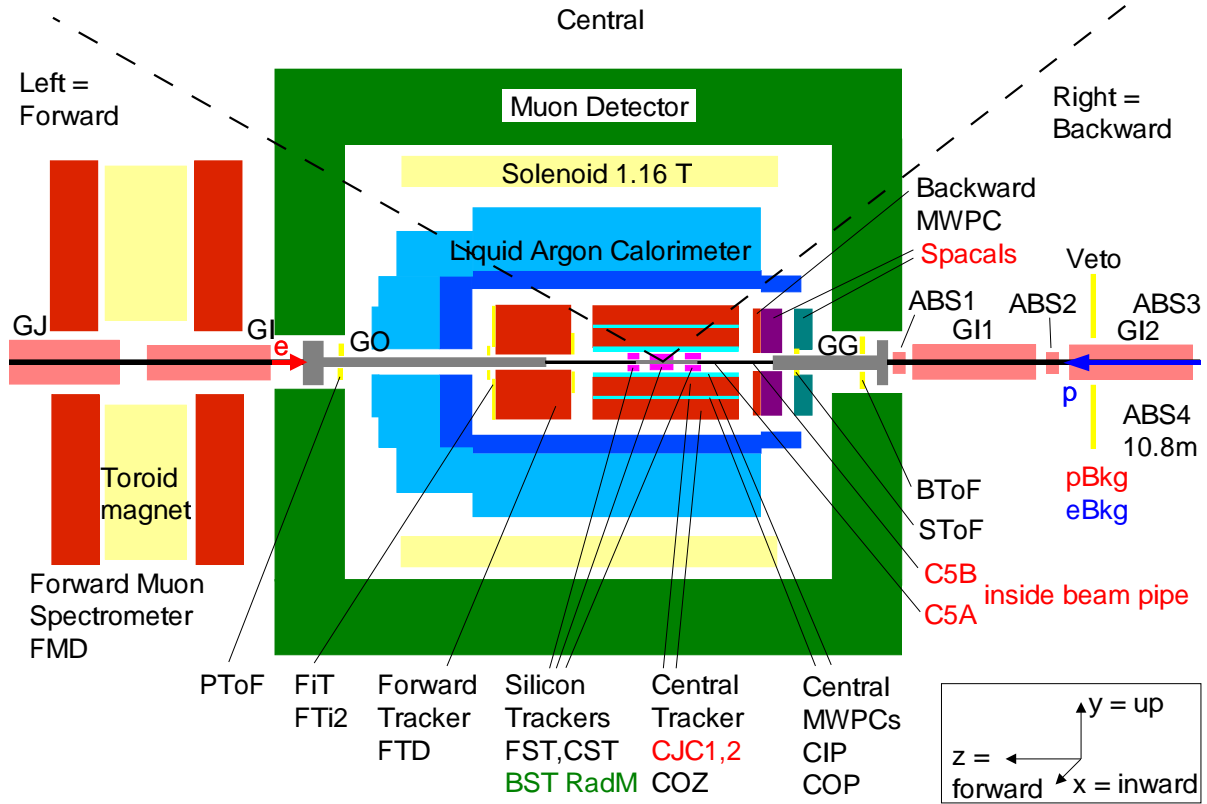


Figure 1: Schematic side view of the H1 detector, located at the North IP of HERA, to scale. The extension along the beam line is about ± 8 m.

In the following, a right-handed Cartesian coordinate system is used with origin at the nominal interaction point, z axis in the proton direction, y axis pointing vertically upwards and x axis towards the center of the HERA ring. Ring components are often referred to as seen by an observer at the ring center facing outwards. ‘North Left’ then refers to the ‘forward’ or proton direction and ‘North Right’ to the ‘backward’ or positron direction. These conventions are illustrated in Fig. 1.

1.4 Limits on Chamber Currents and Radiation Doses

The central drift chamber (CJC) is operated with a gas mixture of 49.6% argon, 49.6% ethane and 0.8% ethanol. The sense wires are made of gold-plated tungsten with a diameter of $20 \mu\text{m}$. Ageing with a significant efficiency reduction is believed to set in after an accumulated charge of 10 C/m [1]. The inner part of the drift chamber, CJC1, has 720 sense wires with a length of 2.2 m. Over 5 years of operation for 10^7 s per year the average CJC1 current should thus be less than $320 \mu\text{A}$. The corresponding limit for the outer chamber, CJC2, with 1920 wires is $850 \mu\text{A}$. However, we have already observed gain reductions of up to 30% in some regions of the CJC2 in 1997 and again of up to 5% in 2000. Extensive re-wirings were done in the long shutdowns of 1998 and 2000 [2]. In 2000 the CJC2 was operated with currents of up to $200 \mu\text{A}$ for $I_e = 46 \text{ mA}$ and $I_p = 105 \text{ mA}$ and this represents what we consider to be a safe limit.

The pattern recognition code can tolerate a few hundred random hits per event, where one event integrates over up to 11 bunch crossings for the widest cells.

The H1 silicon tracking detectors are within radii of 4 and 12 cm of the beam line, and within ± 70 cm of the nominal interaction point in z . The most stringent dose limits for these detectors are determined by the custom CMOS preamplifier ICs and the commercial line drivers and voltage regulators and are about 500 Gy. The central silicon vertex detector uses radiation hard DMILL CMOS ICs at the front end, the digital parts of which are certified for doses of at least 10 kGy. We use part of our backward silicon track trigger detectors as a radiation monitor in a counting mode with a threshold of about 1 MIP. Using the energy loss in silicon (1.7 MeV/g cm^2) and the area of the detector (40 cm^2) and including a safety factor for the unobserved low energy part of the spectrum (synchrotron radiation), we set a continuous rate limit of 50 kHz for safe operation. Excursions above 250 kHz are always due to bad beam steering and a beam dump is requested after a few minutes under such circumstances. The dynamic range of the device extends up to 10 MHz, when it sees every bunch on every turn.

2 Experimental Investigation of the Backgrounds in H1

2.1 Introduction

This section presents a study of the dependence of the background rates observed in the H1 detector on the HERA beam currents. A simple model which describes the observations is developed and used to identify the most significant source of background, namely proton beam-gas interactions. First investigations are made of the sensitivity of the observed background rates to the quality of the vacuum at various points along the beam line. The model is used to predict the background rates expected at full HERA II luminosity and hence to deduce the level of improvements necessary before H1 can operate at full luminosity.

2.2 Dependence of Chamber Currents on Beam Currents

Under normal conditions the CJC is operated at a sense wire voltage of 1485 V, corresponding to an anode surface field of 28.25 kV/mm. During luminosity running, the chamber currents are seen to depend on both beam currents, I_e and I_p , and four contributions can be distinguished (see Fig. 2):

1. A small pedestal current I_0 , determined in off-beam periods which is constant in time and independent of the beam conditions ($15 \mu\text{A}$ in CJC2, $8 \mu\text{A}$ in CJC1).
2. A contribution from synchrotron radiation, $\alpha_{\text{SR}} I_e$, proportional to the positron current I_e .
3. A contribution from positron beam-gas interactions, $\alpha_e I_e \langle P_L \rangle$, proportional to the positron beam current and the average pressure to the left of the IP.
4. A contribution from proton beam-gas interactions, $\alpha_p I_p \langle P_R \rangle$, proportional to the proton beam current and the average pressure to the right of the IP.

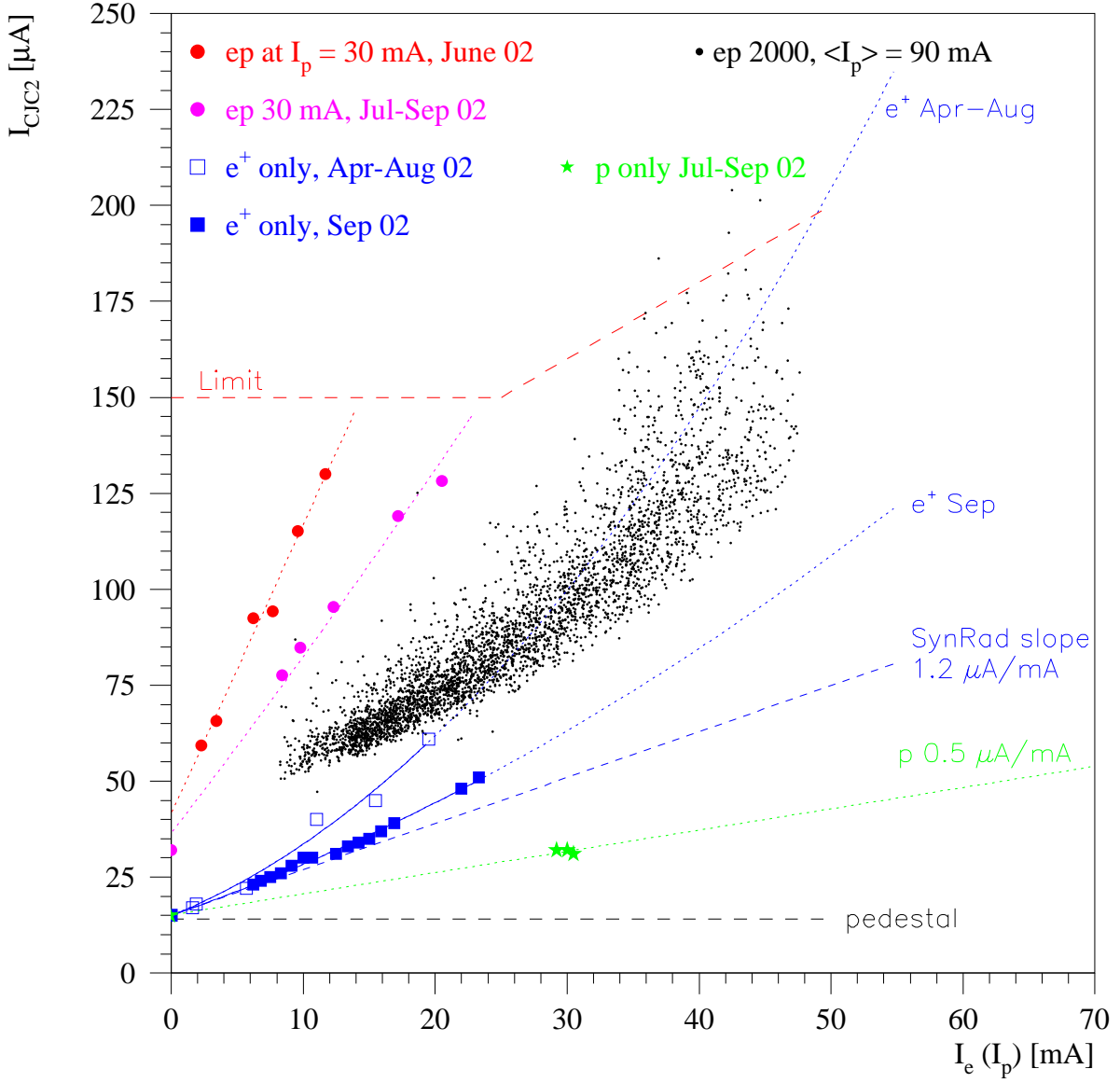


Figure 2: CJC2 current versus beam current. For protons-only (green stars) abscissa is I_p . For ep operation in 2002 (red and magenta circles) the chamber current is re-scaled to $I_p = 30$ mA and plotted versus I_e . The points from 2000 (black dots) are plotted as measured versus I_e and were all taken with $I_p > 70$ mA with a mean of 90 mA. The curves are explained in the text.

Assuming that the average pressure depends linearly on the positron beam current and is given by $\langle P_L \rangle = P_0^L + \gamma_L I_e$ and $\langle P_R \rangle = P_0^R + \gamma_R I_e$, with P_0 representing the base pressure, the total CJC current, I_{CJC} , can be parameterized as follows

$$I_{CJC} = I_0 + \tilde{\alpha} I_e + \alpha_e \gamma_L I_e^2 + \alpha_p I_p (P_0^R + \gamma_R I_e), \quad (1)$$

where $\tilde{\alpha} = \alpha_{SR} + \alpha_e P_0^L$ combines the contribution from synchrotron radiation and from positron beam-gas at the base pressure. The coefficients $\tilde{\alpha}$ and $\alpha_e \gamma_L$ are determined from positron-only fills, while $\alpha_p P_0^R$ and $\alpha_p \gamma_R$ are derived from fits to CJC current measurements during luminosity operation.

During HERA running, a clear correlation is observed between the silicon pad detector rates and the beam currents, and thus also with the currents drawn by the CJC. The rate counted in

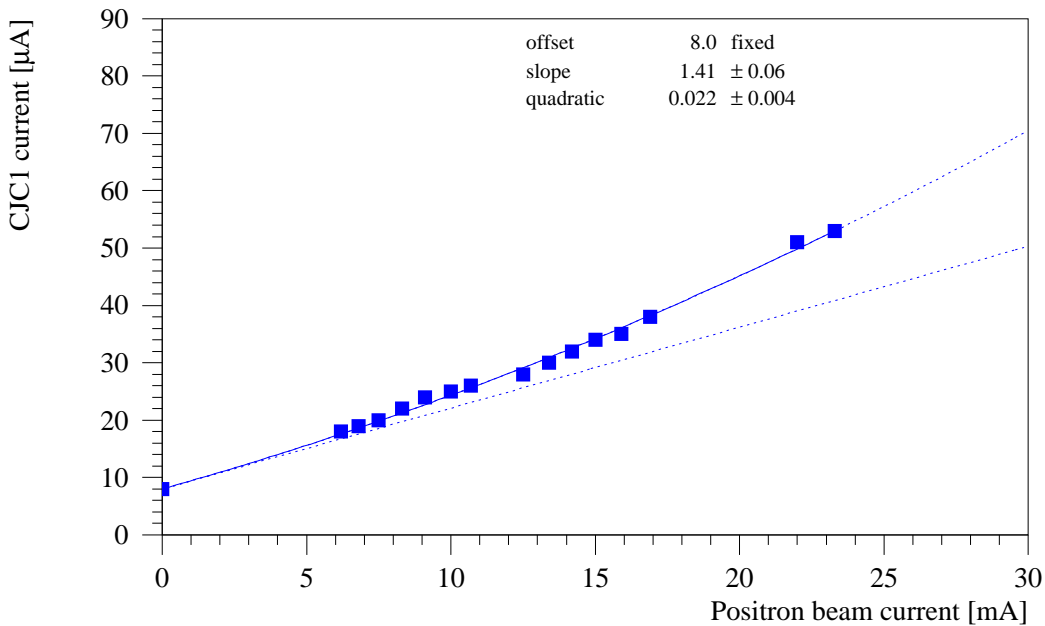


Figure 3: CJC1 current with stable positron beam on 11.9.2002. The solid line is a quadratic fit, the dashed line is the linear component. The accuracy of the measurement of the current is about $\pm 1 \mu\text{A}$.

the silicon radiation monitor can be described by a formula analogous to equation 1,

$$R_{\text{radmon}} = \tilde{\beta}I_e + \beta_e\gamma_L I_e^2 + \beta_p I_p (P_0^R + \beta_R I_e), \quad (2)$$

with a negligible offset rate.

2.3 Contribution of Synchrotron Radiation and Positron Beam-Gas Interactions to CJC Current

On September 11th 2002, a 15 h e^+ fill was taken in order to study the contributions to the CJC currents arising from synchrotron radiation and positron beam gas interactions. After background optimization, the CJC1 current stabilized at $I_e = 23.3 \text{ mA}$. Figure 3 shows the subsequent drop of the CJC1 currents with decreasing positron current. Fitting equation 1 (with $I_p = 0$, $I_0 = 8 \mu\text{A}$) to the data clearly reveals a quadratic beam-gas component which, when extrapolated to 55 mA of positron beam current, amounts to 86% of the linear synchrotron radiation component. A similar fit to the CJC2 current gives $\tilde{\alpha} = (1.20 \pm 0.07) \mu\text{A}/\text{mA}$ and $\alpha_e\gamma_L = (0.014 \pm 0.004) \mu\text{A}/\text{mA}^2$. The quadratic component therefore amounts to 64% of the linear component at 55 mA.

Similar observations are made for the radiation monitor rate which can be represented by $\tilde{\beta} = 0.126 \text{ kHz}/\text{mA}$ and $\beta_e\gamma_L = 0.014 \text{ kHz}/\text{mA}^2$. In this case the quadratic component is larger than the linear component at 55 mA. The difference in the relative importance of the quadratic beam-gas and the linear synchrotron radiation terms can be attributed to the higher sensitivity of the drift chamber to low energy synchrotron radiation than the silicon pad sensors.

A shorter positron-only run was taken on August 4th 2002, see figure 4. Independent quadratic fits give the same linear component due to synchrotron radiation, as expected for

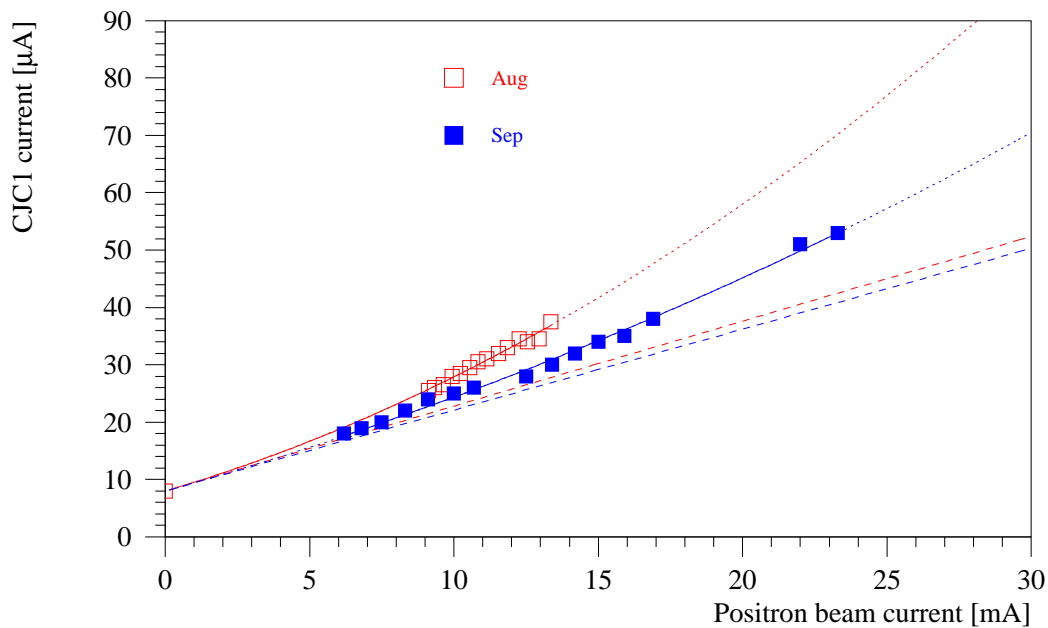


Figure 4: CJC1 current with stable positron beam on 4.8.2002 (open red squares) and on 11.9.2002 (solid blue squares). The dashed lines show the linear component of the independent fits to the two data sets, which are identical within errors. The quadratic component decreases by a factor of 2 from August to September.

optimal beam steering in both cases, but reveal an increase of the quadratic term by a factor of two. Investigation of the beam pipe pressure to the left of the IP (positron upstream) reveals that the highest reading comes from the getter pump at 25.9 m (figure 5) and that this was almost a factor of two higher at 13 mA positron current in August than in September (figure 6). This provides some indication that improved vacuum in the region around 25 m to the left of H1 would reduce the positron beam-gas background, which constitutes about 50% of the total positron induced background at full positron current.

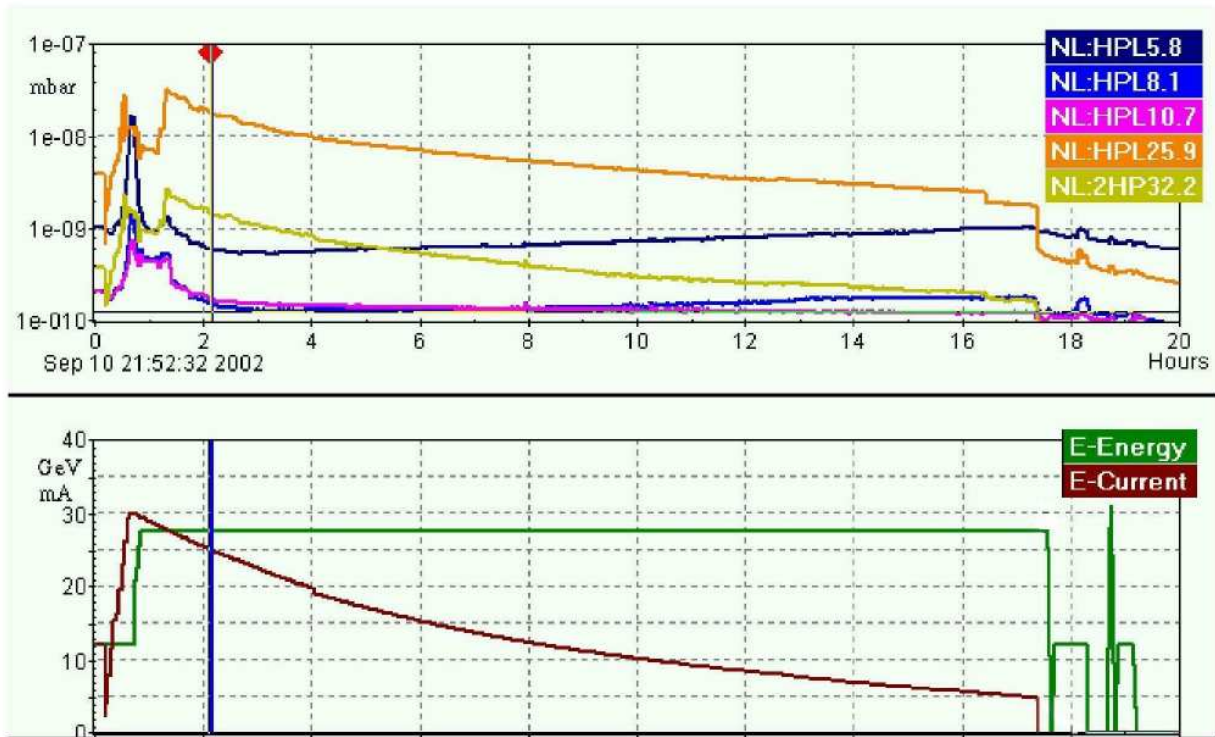


Figure 5: Pressure at five positions to the left of H1 during the long e^+ fill on the 10th and 11th September 2002. The names of the pumping stations indicate their position in meters. The highest pressure is measured at 25.9 m. The pressure increases during the background tuning period at 27.5 GeV, possibly when the vertical “BI bump” is introduced into the positron orbit to ensure direct synchrotron radiation is steered away from the H1 detector.

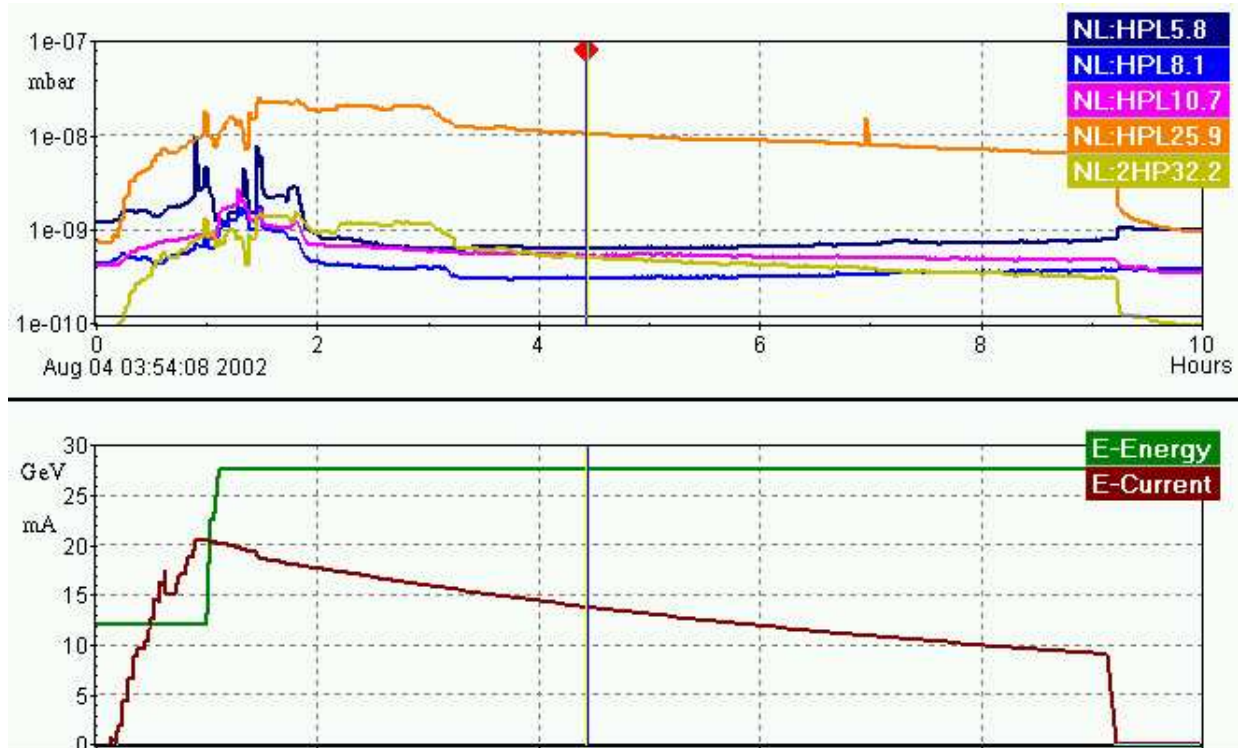


Figure 6: Pressure at five positions to the left of H1 during the e^+ fill on August 4th 2002. The pressure at 25.9 m was higher than a month later. The August CJC currents shown in figure 4 are taken from the stable period beginning at the vertical marker.

The sensitivity of the CJC currents to the local beam pipe pressure for positron operation was further studied on 13.8.2002 when a 4 mA beam was stored at 27.5 GeV and nine titanium sublimation pumps (TSPs) between 5.6 and 53.3 m upstream were fired in succession, see figures 7 and 8. The pressure increase measured in getter pumps next to the TSPs was between a factor of 50 and 500. However, the pressure increase in the beam pipe itself is best estimated by observing the “crosstalk” in adjacent pumps. Here we note a strong coupling between the pumps at 5.8, 8.1, and 10.7 m and between those at 25.9 and 32.2 m and estimate pressure increase factors of between 10 and 30, reaching values of 10^{-8} mbar.

The history of the CJC1 chamber current is shown in figure 9; no effects are observed. However, the sensitivity of the measurement is difficult to quantify. The positron current was rather low. The first firings were done with a rather high chamber current of around $40 \mu\text{A}$ and were repeated at $20 \mu\text{A}$ after beam steering which presumably reduced the synchrotron radiation contribution. Due to some “memory effect” in the pumps, the second set of pressure peaks is smaller. In conclusion, this study does not rule out a significant positron beam-gas contribution to the background at higher beam current and, to aid localisation of the regions in which the vacuum is particularly critical, should be repeated with larger positron currents.

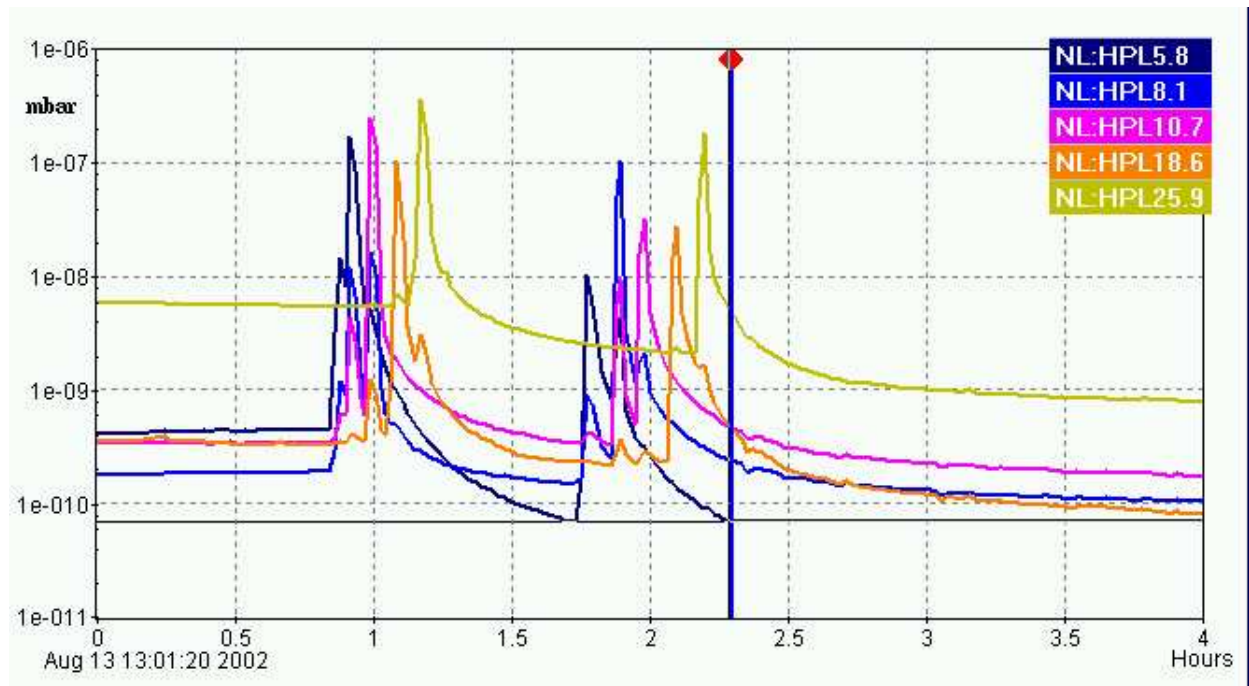


Figure 7: Pressure history for the firing of five upstream positron TSPs. The group of pumps was fired twice, one at a time, and shows some memory effect in that the second firing leads to a smaller pressure peak. The pressure increase in the beam pipe proper can be estimated from the cross-talk in neighbouring pumps. A positron beam of 4 mA was stored during this procedure.

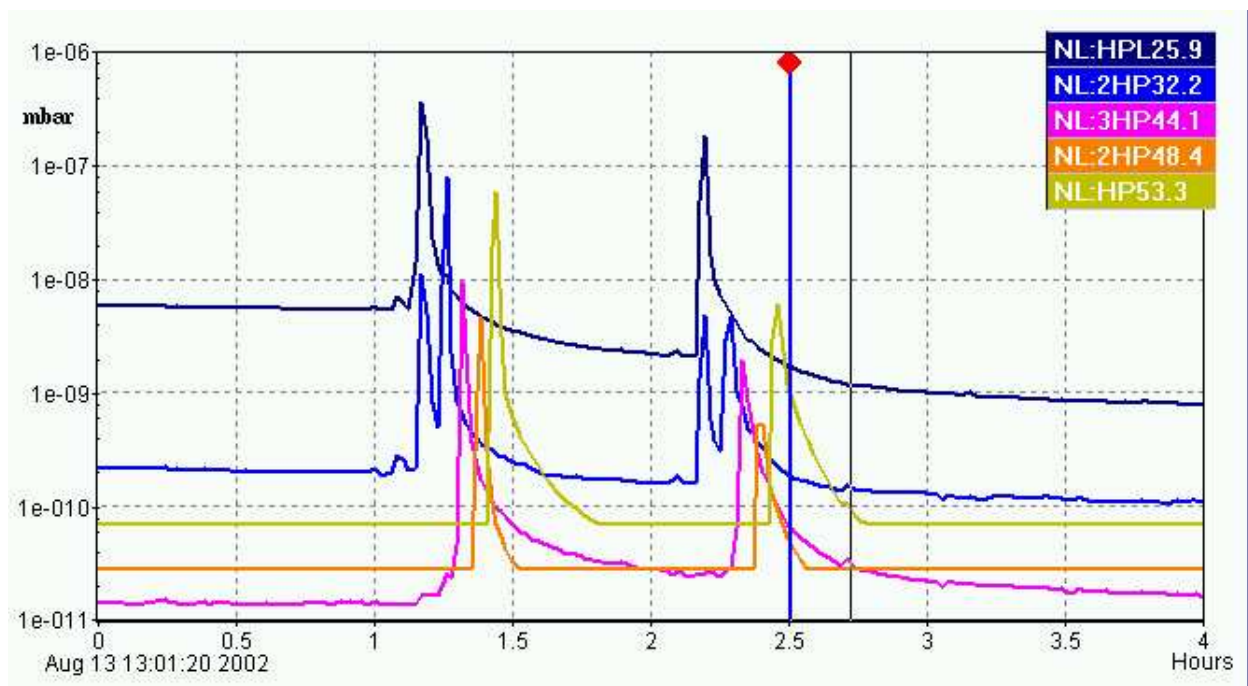


Figure 8: Pressure history for the firing of four more TSPs up to 53.3 m upstream of the IP. A positron beam of 4 mA was stored during this procedure.

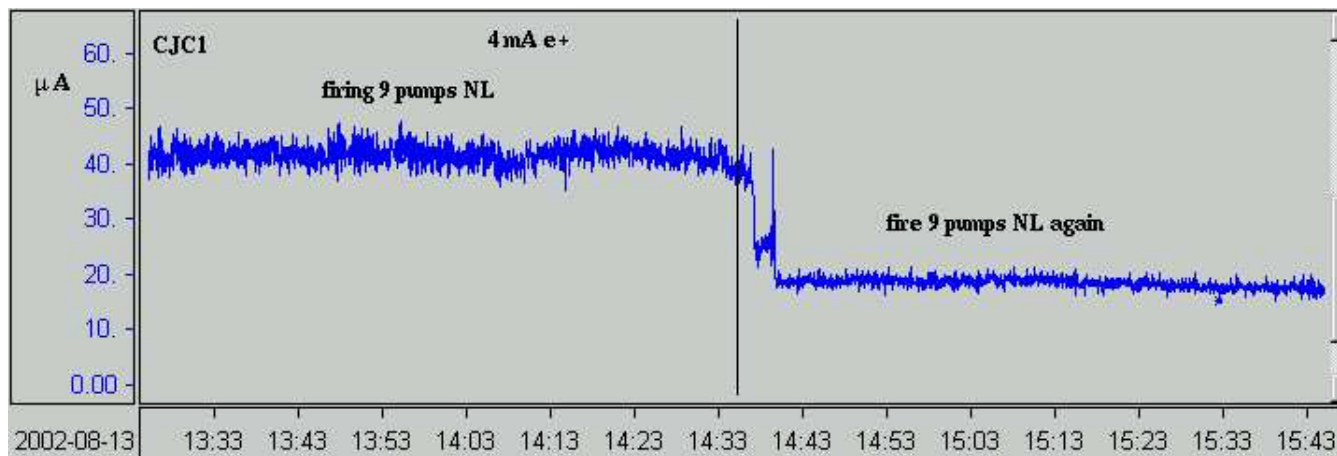


Figure 9: CJC1 current with a 4 mA e^+ current during the firing of 9 TSPs North Left. The step in the chamber current is due to HERA beam steering, after which the pumps were fired again. No pressure related effect is seen. However, the sensitivity of the measurement may be low given the low positron current, the initially high chamber currents and the reduced pressure peaks in the second firing of the pumps.

2.4 Effects of Positron Beam on Vacuum in North Right

The effects of the positron beam on the pressure to the right of H1 can also be studied directly in positron-only fills. As an example, Fig. 10 shows the pressure measured at the pump at 8.3 m North Right as a function of the beam current on September 11th 2002. A pressure of $6 \cdot 10^{-9}$ mbar is reached at $I_e = 15$ mA. A slope of $\gamma_{NR8.3} = 0.2 \cdot 10^{-9}$ mbar/mA may be extracted from the linear region after completion of beam steering. We note that the curve extrapolates to a large offset pressure of about $4 \cdot 10^{-9}$ mbar. This large offset later decreased, as is shown in figure 11, measured during a luminosity run on September 15th 2002, and was perhaps associated with a persistent discharge in the pump. In this later run, the base pressure is about $2 \dots 3 \cdot 10^{-9}$ mbar/mA and the measured slope is similar to that in the run on September 11th.

During the 2000 running period, the pump at this position showed a pressure of $6 \cdot 10^{-9}$ mbar at 50 mA and extrapolated to a base pressure of about 10^{-10} mbar. The slope was about $\gamma_{NR8.3}^{2000} = 0.12 \cdot 10^{-9}$ mbar/mA, somewhat smaller than observed in September 2002. From the experiences with CJC operation in 2002 we conclude that a pressure of $6 \cdot 10^{-9}$ mbar or better is desirable at design current in this region.

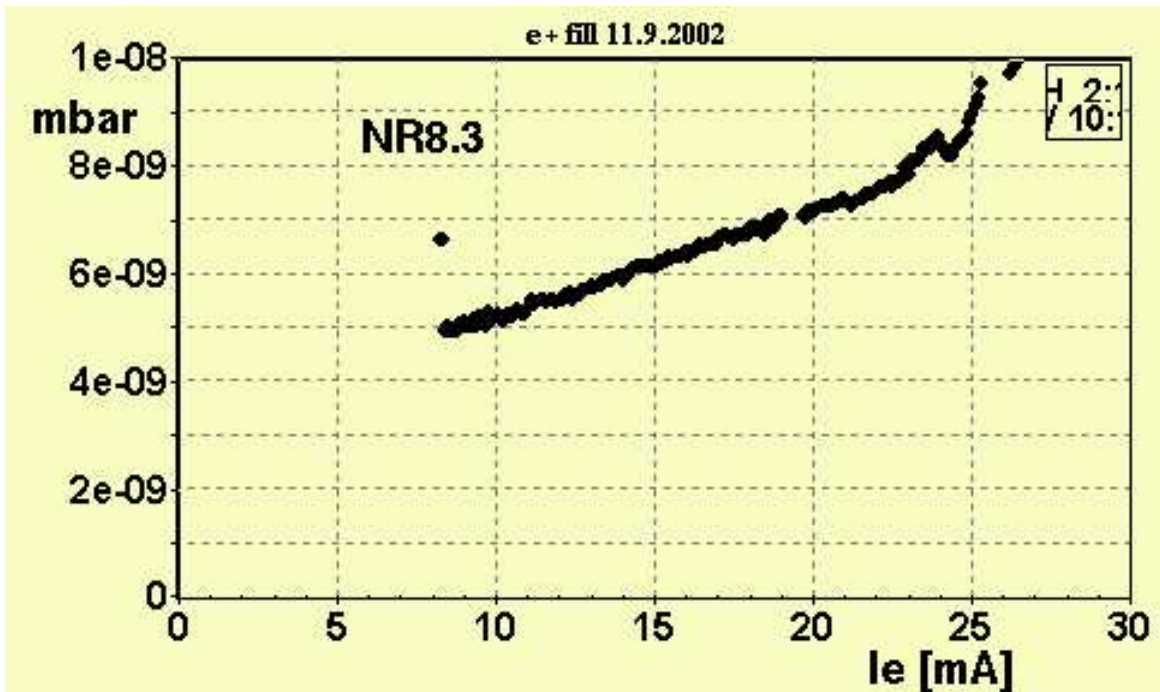


Figure 10: Pressure at North Right 8.3 m versus positron current during the long e^+ fill on September 11th 2002. The slope in the smooth region after steering is $\gamma_{NR8.3} = 0.2 \cdot 10^{-9}$ mbar/mA. A pressure of $6 \cdot 10^{-9}$ mbar is reached at 15 mA.

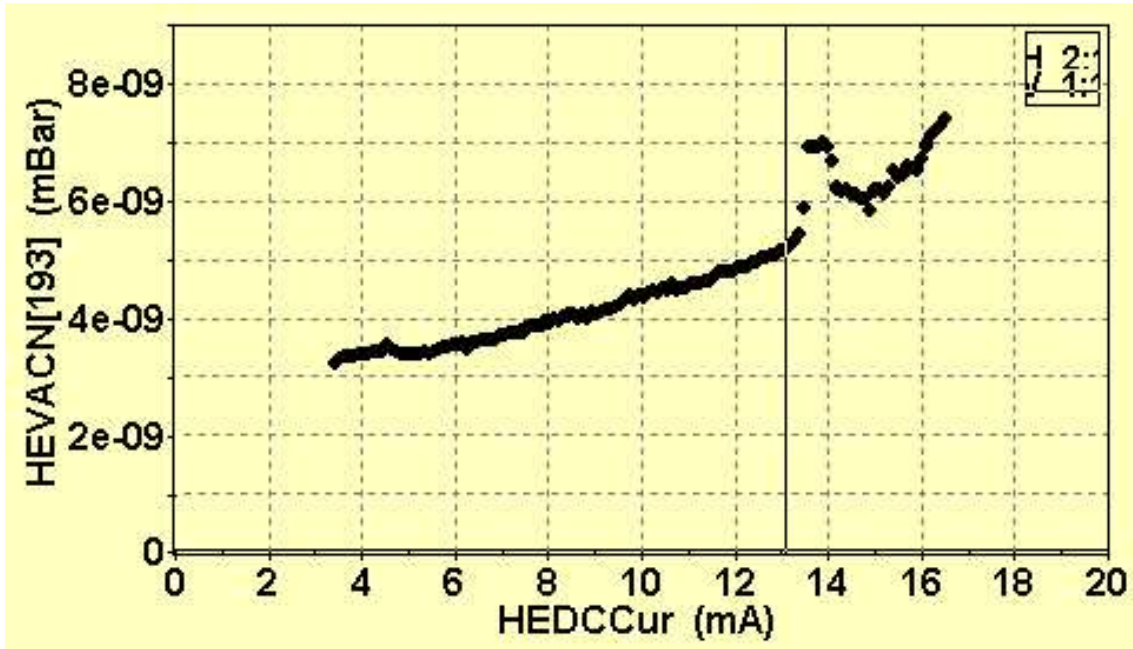


Figure 11: Pressure at North Right 8.3 m versus positron current during a luminosity run on September 15th 2002. The slope in the smooth region is roughly $\gamma_{NR8.3} = 0.2 \cdot 10^{-9}$ mbar/mA. Extrapolation to zero positron current gives a base pressure of about $2 \dots 3 \cdot 10^{-9}$ mbar.

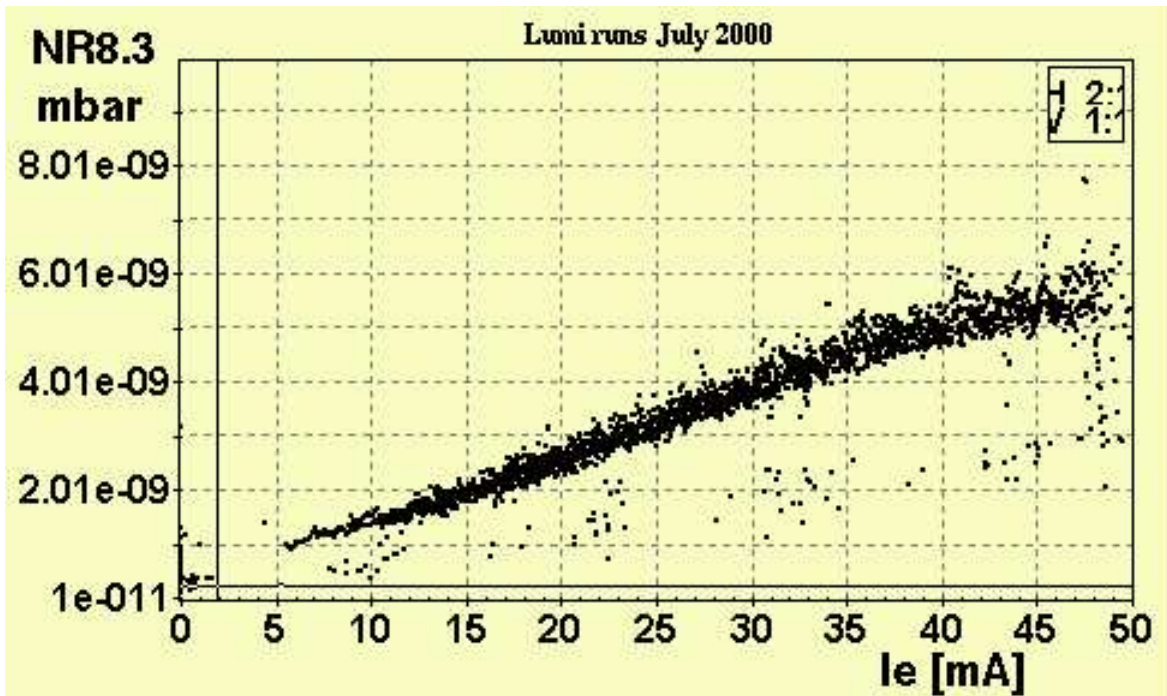


Figure 12: Pressure at North Right 8.3 m versus positron current from July 2000. The slope was $\gamma_{NR8.3} = 0.12 \cdot 10^{-9}$ mbar/mA. A pressure of $6 \cdot 10^{-9}$ mbar was reached at 50 mA. The base pressure was about 10^{-10} mbar.

2.5 Vacuum Quality and Proton Induced Background

Three points at proton currents of 30 mA are shown in figure 2, taken in July, August and early September 2002. We consistently measure currents of $32 \mu\text{A}$ in CJC2 and, using the pedestal of $15 \mu\text{A}$, derive a slope of $0.6 \mu\text{A}/\text{mA}$. Runs taken at higher I_p suffer from HERA-B operation with non-optimal collimator settings or, on one occasion, from a pressure increase in the proton ring observe as the current reached about 70 mA.

We have studied data from two proton-only fills from 1999, both with beam currents of 88 mA, in which chamber currents of approximately 5 and $15 \mu\text{A}$ above pedestal were measured, indicating that a much lower base pressure pertained at that time following more than a year of operation since mid-1998.

The sensitivity of the chamber currents to the beam pipe pressure with protons only has also been studied by firing four titanium sublimation pumps (TSPs) located from 3.6 m to 10.8 m upstream of the H1 interaction region. The results can be seen in Figs. 13 and 14 which show the pressure readings and the CJC1 currents during this period. Clear sensitivity to local pressure peaks is observed, even with reduced chamber HV.

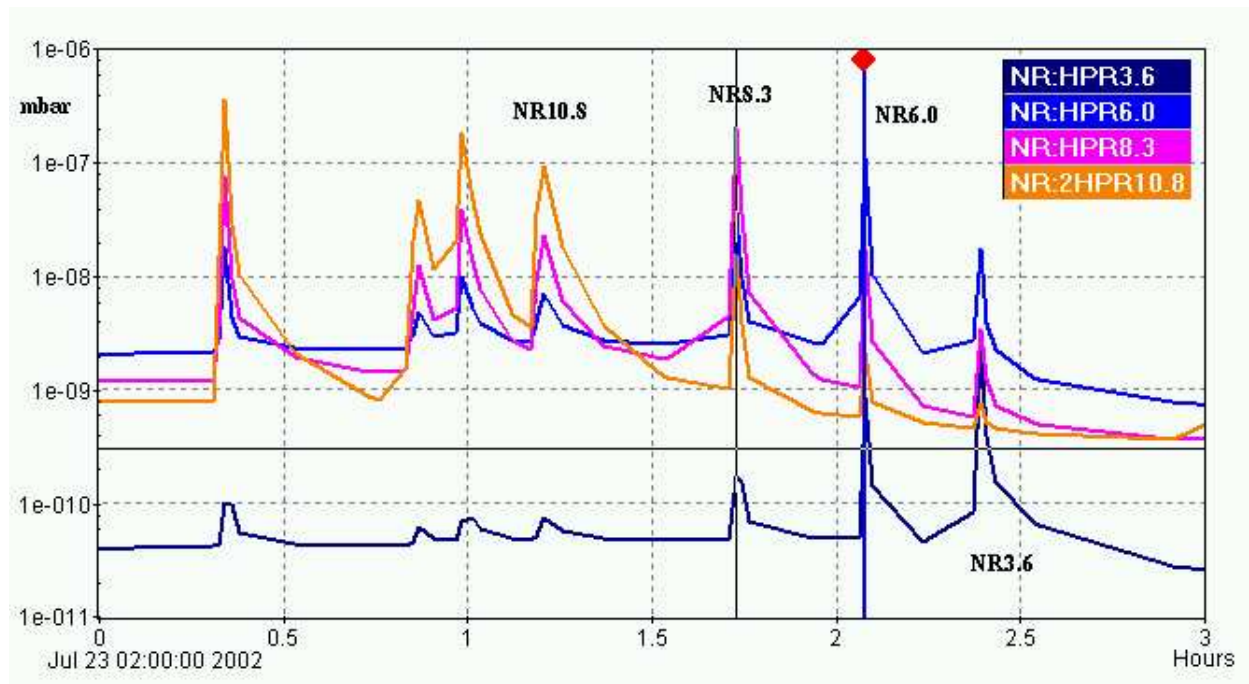


Figure 13: Firing North Right titanium sublimation pumps. A 39 mA proton beam was stored during this procedure.

Pressure studies were also performed with the TSPs in the warm proton beam pipe section at 32, 61, and 75 m upstream of the IP, see figure 15. At the time the GO and GG magnets were warm. A 29 mA proton beam was stored and the CJC2 was at full HV and drawing about $52 \mu\text{A}$, see figure 16. The pressure peaks reached 10^{-8} mbar as measured in adjacent getter pumps. No increase in chamber current was seen. Just after this exercise the cool-down of the GO and GG magnets started, which brought the CJC2 current down to the usual $32 \mu\text{A}$ within the first 90 minutes. We interpret this as being due to the cryogenic pumping effect of the cold beam pipes in GG and GO. Though this initially causes an improvement in the vacuum, the

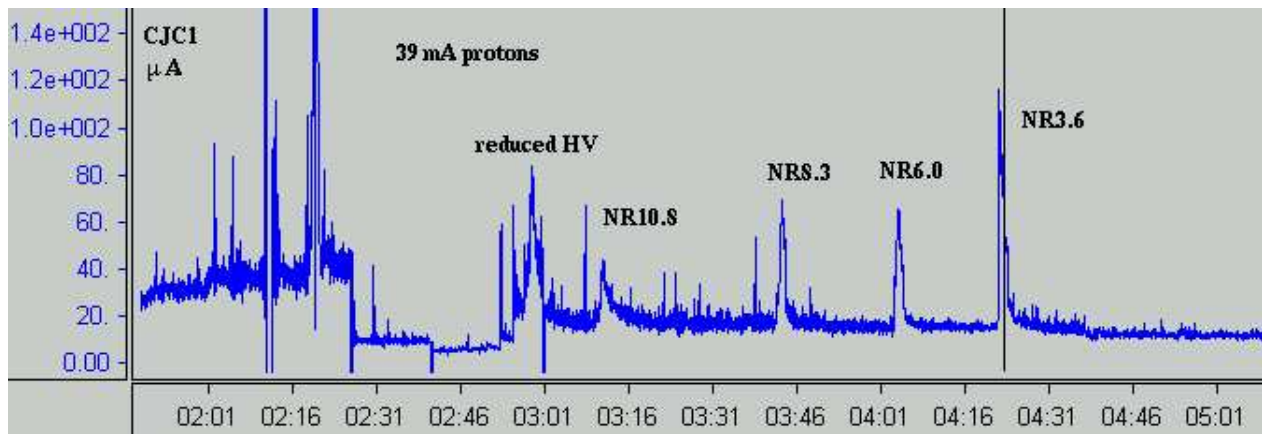


Figure 14: CJC1 current at reduced HV with a 39 mA proton beam on 23.7.2002. The North Right pumps were fired, showing clear sensitivity of the CJC1 current to local pressure peaks in the region between -3.6 m and -10.8 m.

molecules freezing out on these surfaces may later constitute a continuous source of gas as they are liberated from the beam pipe at the cold-warm transitions at the ends of the magnets.

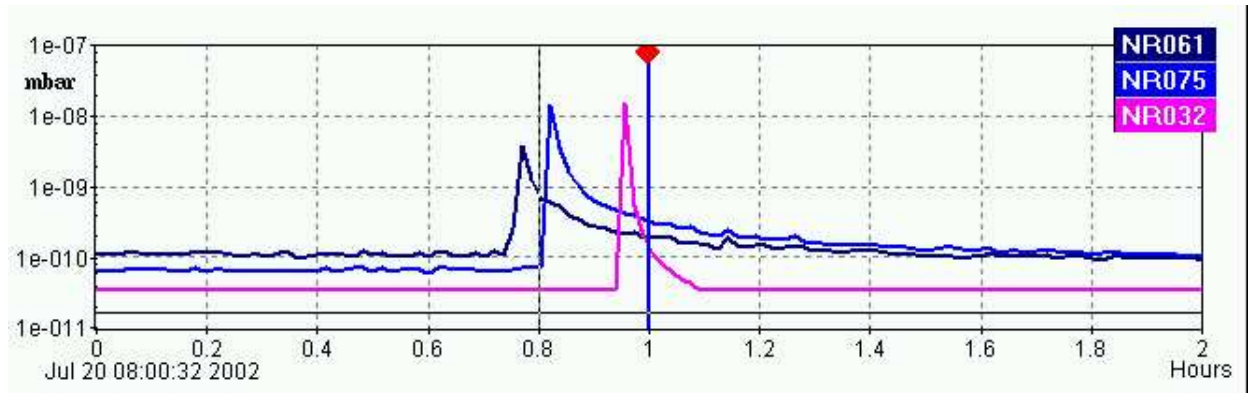


Figure 15: Firing titanium sublimation pumps in the North Right proton beam line. A 29 mA proton beam was stored during this procedure.

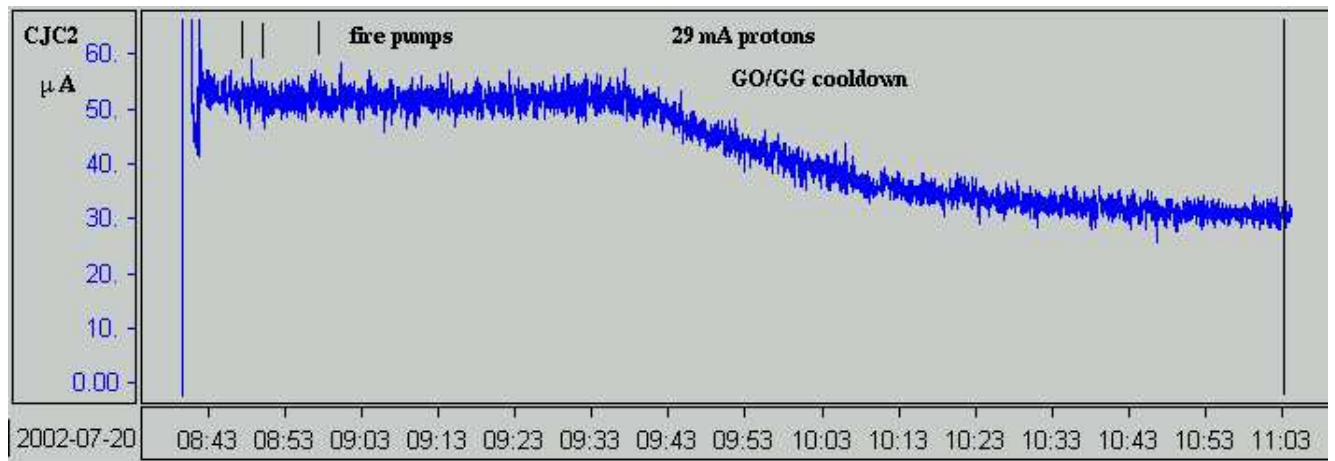


Figure 16: CJC2 current at full HV with a 29 mA proton beam on 20.7.2002. Proton pumps at 61, 75, and 32 m upstream were fired between 8:46 and 8:57. At 9:30 the cooldown of the GO and GG magnets started, showing a clear initial cryogenic pumping effect, possibly due to water freezing out on the cold beam pipe sections.

2.6 Positron-Proton Operation

The CJC2 current measured in ep operation after careful beam steering is shown in figure 2. The lines are fits according to equation 1. The fills in June 2002 have a significantly larger slope than those taken since mid-July. In the intervening period the GO and GG magnets in the North Hall were warmed up, for the first time since their installation in 2001, while the pumps were operated. The magnets were then again cooled. This procedure resulted in a somewhat improved vacuum. As can be seen from the figure, under the conditions pertaining in mid-September 2002, safe operation of the CJC requires that the HERA beam currents be limited to $I_e \cdot I_p < 600 \text{ mA}^2$.

The strong correlation of the CJC current with the pressure in the beam pipe during ep operation is shown in figure 17 for the pump at North Right 8.3 m. The pressure history for a long luminosity fill on 7.9.2002 is shown in figure 18. The silicon radiation monitor rate for the

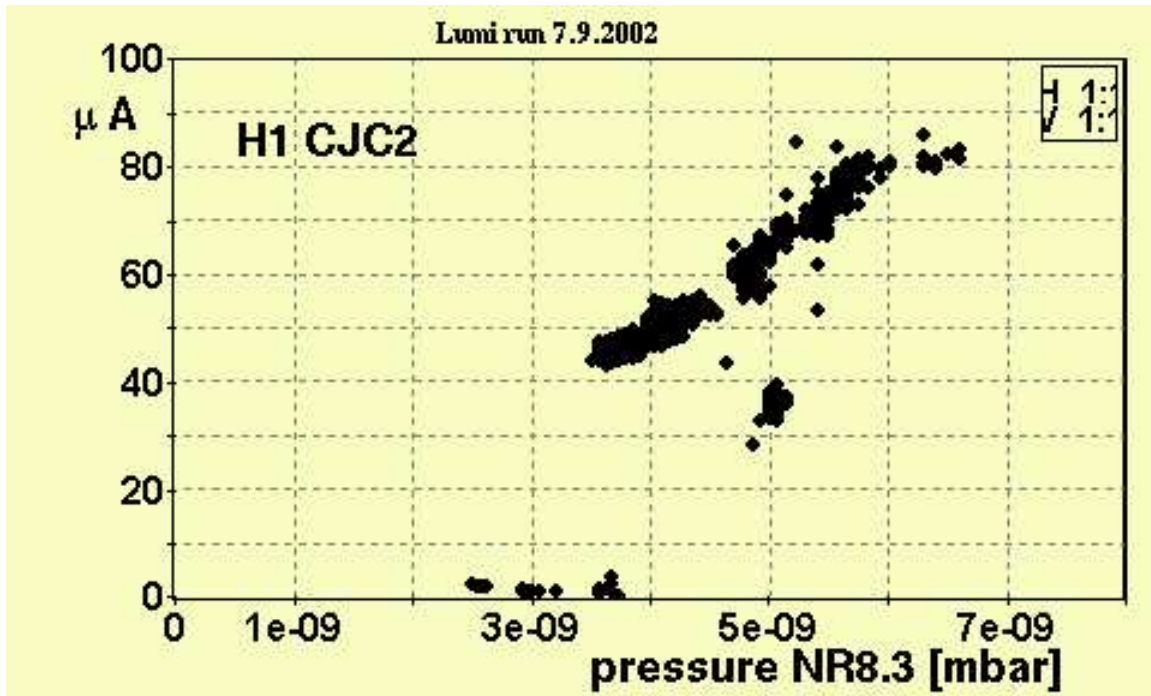


Figure 17: CJC2 current versus pressure at North Right 8.3 m during 11 h of a luminosity run on 7.9.2002. The proton current was 20 mA.

same luminosity fill is shown in figure 19 and shows a dependence in accordance with equation 2 after an initial steering period and while the HERA-B target rate was stable at 4 MHz.

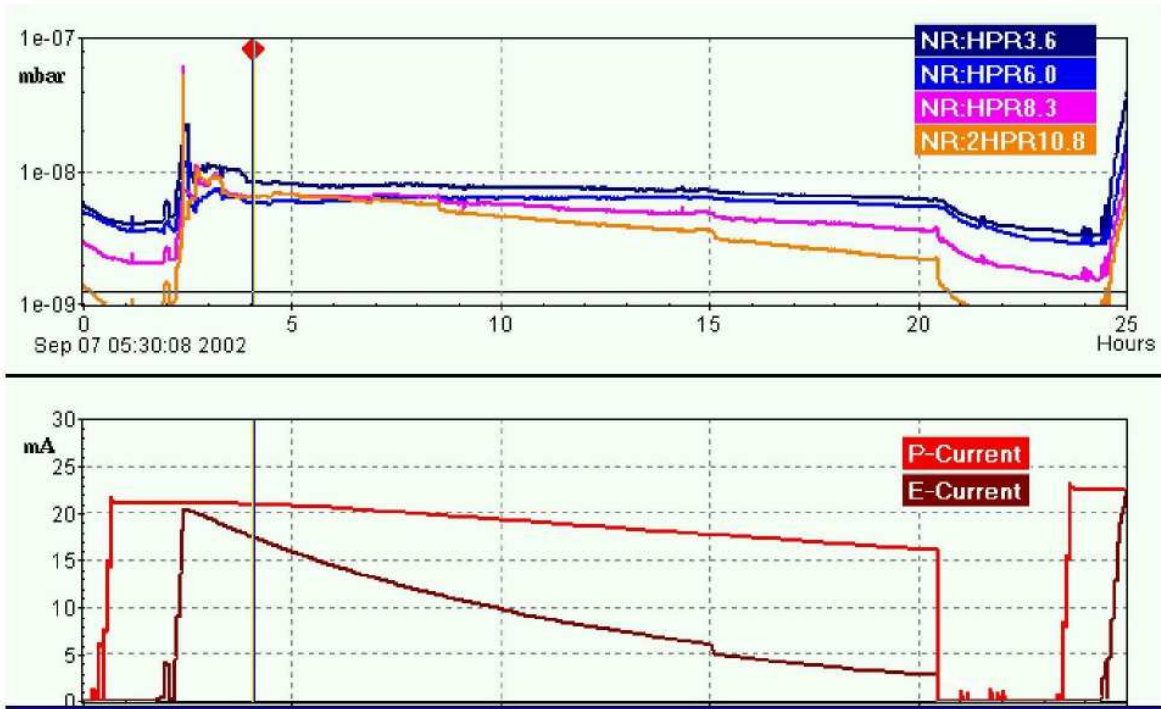


Figure 18: Pressure history at North Right during the luminosity run on 7.9.2002.

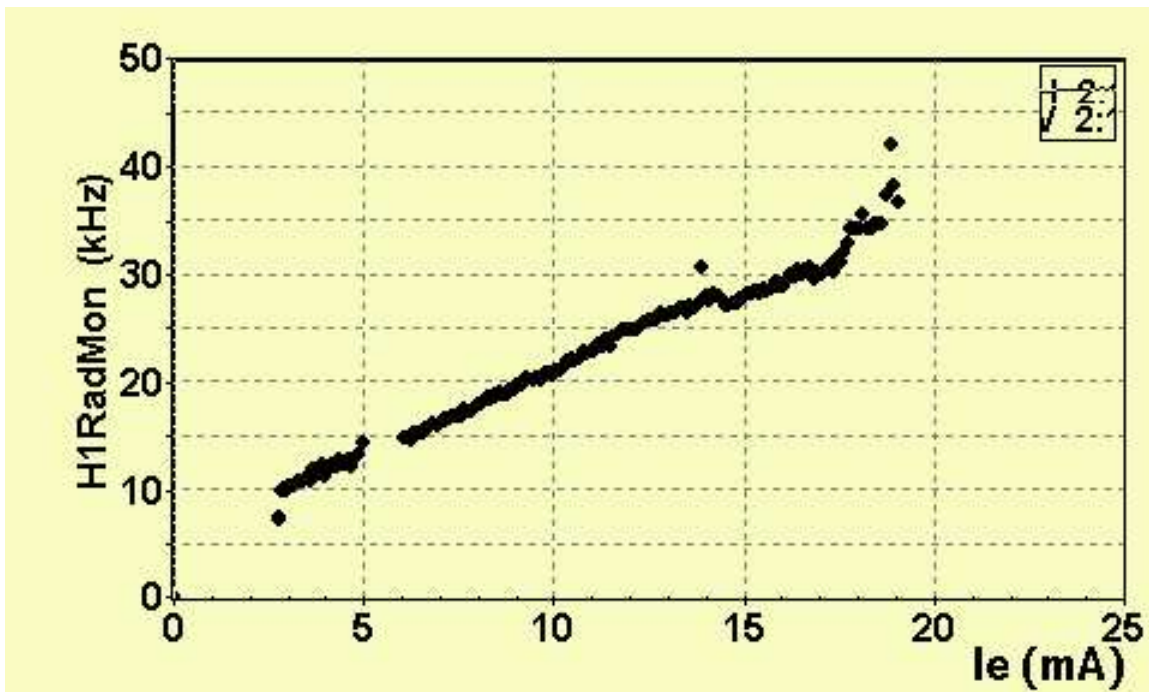


Figure 19: Silicon radiation monitor rate versus positron current during the luminosity run on 7.9.2002. The proton current was 20 mA. The rate limit of 50 kHz was not exceeded even during the ramping and luminosity tuning phases. The step at 14 mA is due to an increase of the HERA-B target rate from 2 to 4 MHz; the target rate was stable for the rest of the fill.

2.7 Extrapolation to Design Currents

The design HERA II currents are 135 mA for the proton beam and 55 mA for the positron beam, with 174 colliding plus a few pilot bunches. Extrapolating from the present significantly lower currents using equation 1 with the coefficients determined from the mid-September ep and e^+ fills suggests that the current in the CJC2 would be about 1 mA at HERA II design beam currents, a factor of 5 above the limit used in 2000, see figure 20. Improving the pressure by a factor of 3.3 to the 2000 level and reducing the synchrotron radiation contribution by a factor of 1.8 by coating absorber 4 (see next section) leads to a CJC2 current of $300 \mu\text{A}$ ('scenario A'). Improving the pressure by a factor of 5.3, with the same reduction in the synchrotron radiation contribution, leads to a chamber current of $200 \mu\text{A}$ ('scenario B'). The dependence of the radiation monitor rate on the proton beam current was also determined using the ep luminosity data taken in September, resulting in the parameters $\beta_p P_0^R = 0.416 \text{ kHz/mA}$ and $\beta_p \beta_R = 0.051 \text{ kHz/mA}^2$, see equation 2. Performing the large extrapolation to the HERA design currents results in an estimated rate of about 400 kHz, with an expected contribution of 50 kHz from positron beam only operation at 55 mA. The ep rate is expected to drop to 120 kHz in scenario A and to 80 kHz in scenario B. Given the uncertainty of these estimates, one arrives independently at a conclusion which is consistent with the CJC current based extrapolation, namely that pressure reductions of more than a factor of 5 with respect to those pertaining in mid-September 2002 are needed for safe operation of the CJC and the silicon detectors.

2.8 Summary

The CJC currents and radiation monitor rates in the H1 detector can be explained in terms of contributions induced by the positron and proton beams. The positron beam is observed to cause deterioration of the vacuum to the right of H1, resulting in an increased proton induced background rate. The background rates provide evidence that the vacuum in September 2002 is somewhat worse than that which pertained in 1999, following a running period of more than a year. Pressure measurements provide some support for this, though the calibration of the pumps is not well known. It also appears that the influence of the positron beam on the vacuum to the right of H1 is stronger now than it was in 1999.

Positron induced background is influenced by vacuum conditions up to and perhaps beyond 25 m to the left of H1. Further studies would be necessary to better quantify this component of the background. Proton induced background is most strongly affected by vacuum conditions up to around 10 m to the right of H1.

Performing the large extrapolation from the conditions pertaining in mid-September 2002 to full HERA II luminosity produces unacceptable currents in the CJC. About 10 to 15% of these arise from the direct effects of the positron beam; the remainder are proton induced. The proportion of the positron induced background attributable to the effects of synchrotron radiation is about half. Acceptable operating conditions can be achieved if the vacuum is improved by a factor of about 5 in the interaction region and to the right of H1 up to a distance of at least 10 m, in conjunction with a reduction of a factor of about 2 of the synchrotron radiation induced background. Decreasing the pressure in the beam pipe to the left of H1 out to a distance of at least 25 m would provide a further small improvement in operating conditions due to the reduction in the rate of positron beam-gas interactions.

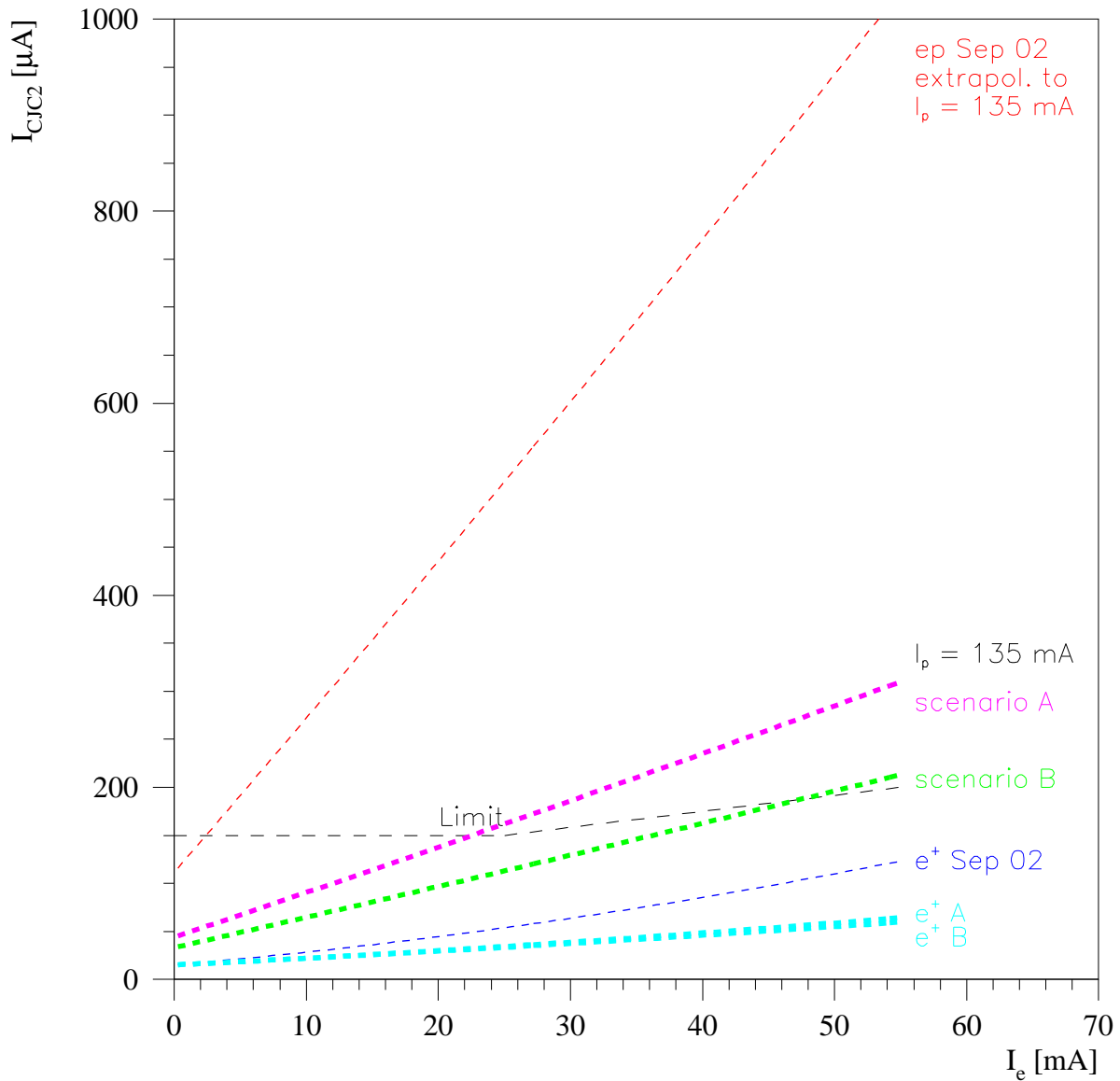


Figure 20: CJC2 current versus positron beam current. The 2002 conditions are extrapolated to $I_p = 135$ mA. For ‘scenario A’ a pressure reduction by a factor of 3.3 on both sides of the IP (reaching the 2000 level) and a reduction of the synchrotron radiation background by a factor 1.8 are assumed. For ‘scenario B’ a pressure reduction by a factor of 5.3 is assumed, together with the factor 1.8 reduction in the synchrotron radiation background.

There is some evidence that some components of the residual gas in the beam pipe condense on the cold surfaces within the super-conducting GO and GG magnets and that these gasses are liberated by warming up the magnets.

3 Positron Induced Background

3.1 Introduction

In this section the backgrounds induced by the positron beam are investigated, namely those arising from synchrotron radiation and from positron beam-gas interactions. In particular, the sources of the synchrotron radiation entering H1 are sought, the minimum thickness of the collimators necessary to shield H1 from this background and the relative importance of the backgrounds arising from synchrotron radiation and the interactions of off-momentum positrons are investigated. Minimising the thickness of the synchrotron radiation collimators is of interest as it reduces the amount of material these present to hadrons generated in proton beam-gas interactions and therefore reduces the amount of proton beam induced background in H1. Measures designed to reduce the amount of synchrotron radiation back-scattered towards H1 and to shield sensitive regions of H1 from this radiation are also discussed.

3.2 Synchrotron Radiation

Figure 21 shows a schematic overview of the direct synchrotron radiation in the horizontal plane around the H1 interaction region. The positron beam must be steered such that no collimator or beam pipe wall closer than 10.8 m from the IP is hit directly. At 10.8 m a dedicated copper absorber is placed in front of the GM magnet. Further targets are the front of the GN magnet at 19 m and a photon absorber at 26 m. Synchrotron radiation can be backscattered from these absorbers in the direction of H1.

3.3 Backscattering from Absorber 4

The copper absorber at 10.8 m (ABS4) has a V-shaped front face such that the photons enter it at a glancing angle of 40 mrad. This ensures that the heat load is spread over a sufficiently large area. The spectrum of backscattered photons for an incident synchrotron radiation spectrum with critical energy $E_c = 110$ keV is shown in figure 22. For backscattering into the central detector the relevant photons are those leaving the absorber at angles close to $\Theta = 180^\circ$ from their incident direction. Compton scattering dominates over photo-absorption for photon energies above 130 keV in copper, which leads to an energy cut-off for backscattering from single collisions at $m_e/2$, as can be seen in figure 22. The backscattered spectrum above 10 keV can be approximated very well by a Gaussian with mean 92 keV and width 34 keV. For $E_c = 140$ keV, corresponding to $E_e = 30$ GeV, the mean increases to 99 keV and the width to 38 keV. The cutoff at $m_e/2$ remains.

3.4 Thickness of Collimators C5B and C5A

The central beam pipe is shielded against backscattering from 10.8 m and beyond by two fixed tungsten collimators: C5B at -145 cm and C5A at -80 cm, shown in figure 23. The photon flux incident on C5B is $8 \cdot 10^{10}/s$ at 55 mA and 27.5 GeV, while the smaller C5A receives $6 \cdot 10^9$

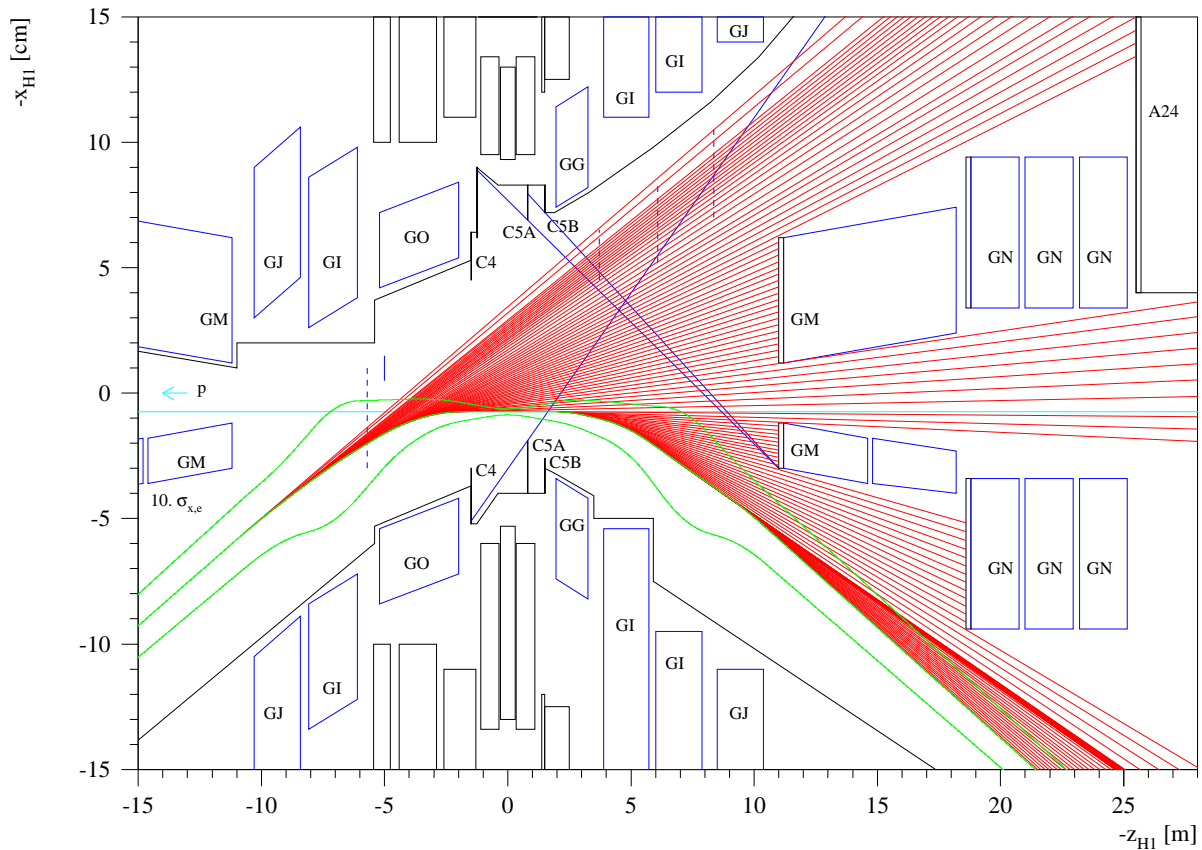


Figure 21: Synchrotron radiation in the horizontal plane. Angles with respect to the H1 z axis are exaggerated by almost a factor 100.

photons/s. C5B and C5A have a thickness of 2 cm, which ensures they completely absorb incident X-rays, but corresponds to 0.2 nuclear interaction lengths for hadrons. The minimum required thickness can be determined from the photon flux at various depths inside the absorber, as shown in figure 24. For a thickness of 5 mm of tungsten, the fraction of penetrating X-rays, with the above energy spectrum, is $8 \cdot 10^{-5}$, giving a flux of $6 \cdot 10^6$ photons/s. The absorptivity is critically dependent on the details of the high energy tail of the photon spectrum. However, these hard (200 keV) X-rays have a low interaction probability in both silicon and argon, of the order of a few percent, and therefore are unlikely to cause background problems. The results derived here are thus insensitive to the precise nature of this tail.

3.5 Backscattering from Collimator C5A

C5A has a coating of 0.4 mm of silver and 0.2 mm of copper, the purpose of which is to reduce the amount of backscattering. The spectrum of backscattered photons is shown in figure 25. The albedo is 1.4%, giving a photon flux of $8 \cdot 10^7$ photons/s at design beam currents.

These photons cause problems if they penetrate the 3 mm aluminium beam pipe in the backward part of H1 and then reach the BST repeater electronics, the CIP, and the CJC. In order to study the effects they have, their interactions in argon gas and a copper layer representing the field and cathode wires of the CJC were simulated. Recoil electrons from photo-absorption and

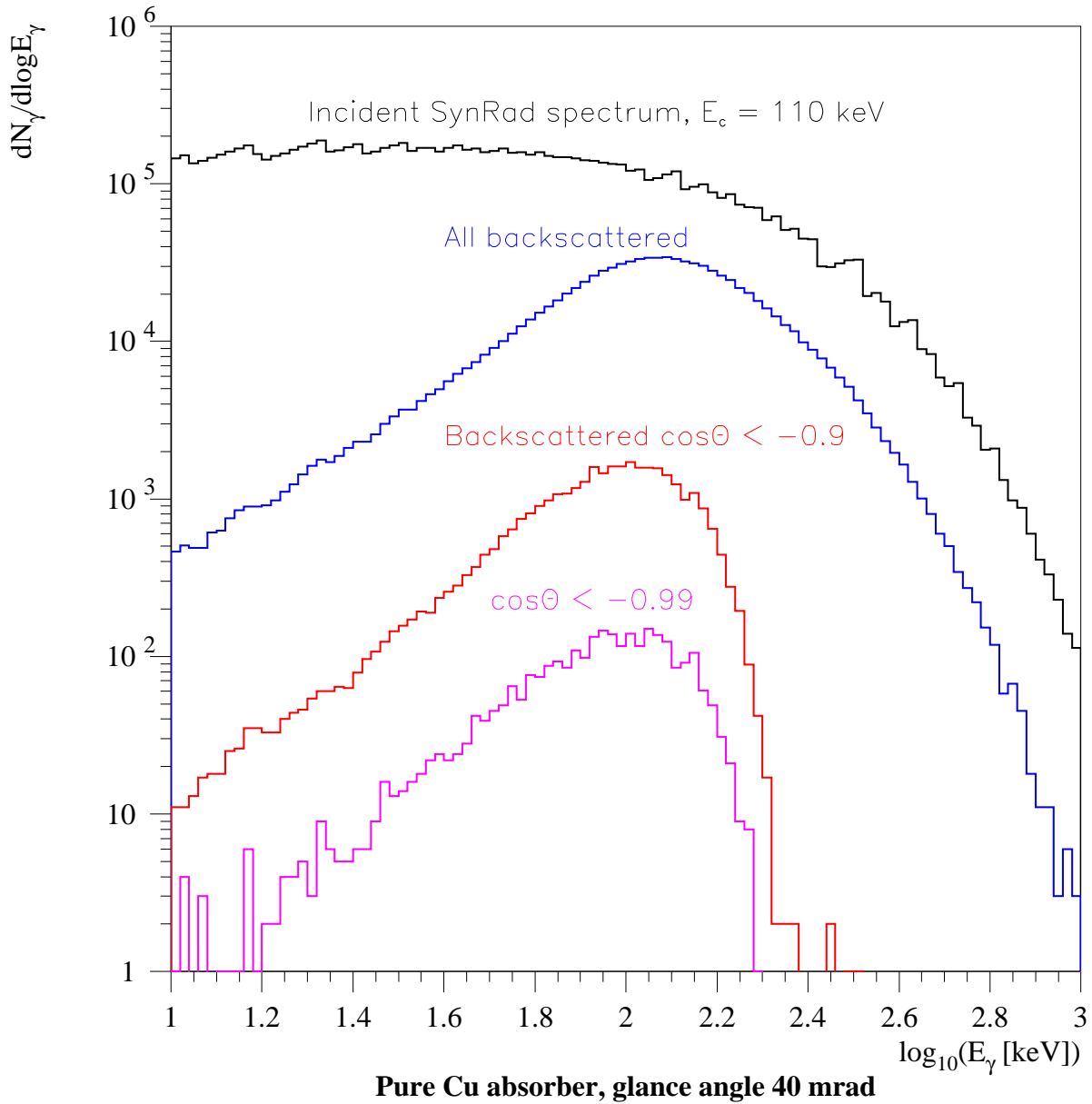


Figure 22: Energy spectrum of synchrotron radiation photons backscattered from a pure copper absorber with glancing incidence at 40 mrad. For a source at 10.8 m the backscattering close to $\Theta = 180^\circ$ is relevant. Here the spectrum shows a cut-off at $m_e/2$ from single Compton scattering.

Compton scattering of the direct radiation, as well as from re-absorption of Ar and Cu fluorescence lines, lead to charge deposits in the chamber. In the CJC, the 1.16 T solenoid field curls these electrons into helices of radii of less than 1 mm, such that the charge is collected on one wire. The simulation assumes 100% charge collection efficiency on the sense wires, omitting effects due to the small proportion of drift field lines that end on potential wires. The charge spectrum shown in figure 26 has a Compton continuum and peaks from Ar and Cu fluorescence at 3 keV and 8 keV, respectively, and a photoelectron peak resulting from the direct X-rays at 60 keV. The charge is scaled to ADC counts, using minimum ionizing particles as a reference, and roughly smeared to mimic the single-hit dE/dx resolution at large amplitudes.

H1 collimators

View along proton beam

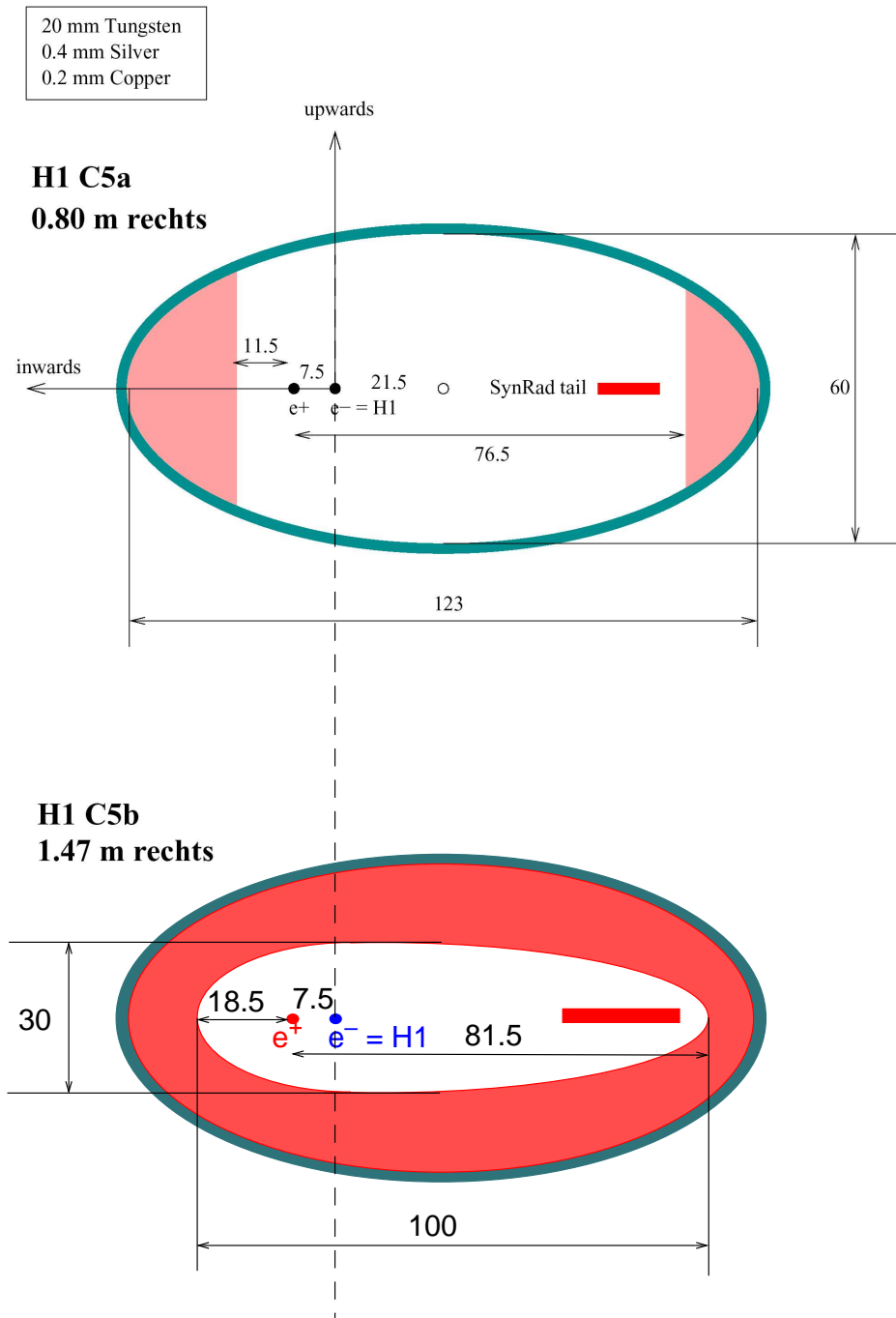


Figure 23: Synchrotron radiation collimators C5B and C5A. The labelled points indicate the nominal positions of the positron and electron beam orbits and the central axis of H1. Also shown is the position of the region in which the bulk of the primary synchrotron radiation is expected.

The measured charge distribution in the CJC with positron beams only and using randomly triggered events with low multiplicity, i.e. events that predominantly contain only synchrotron

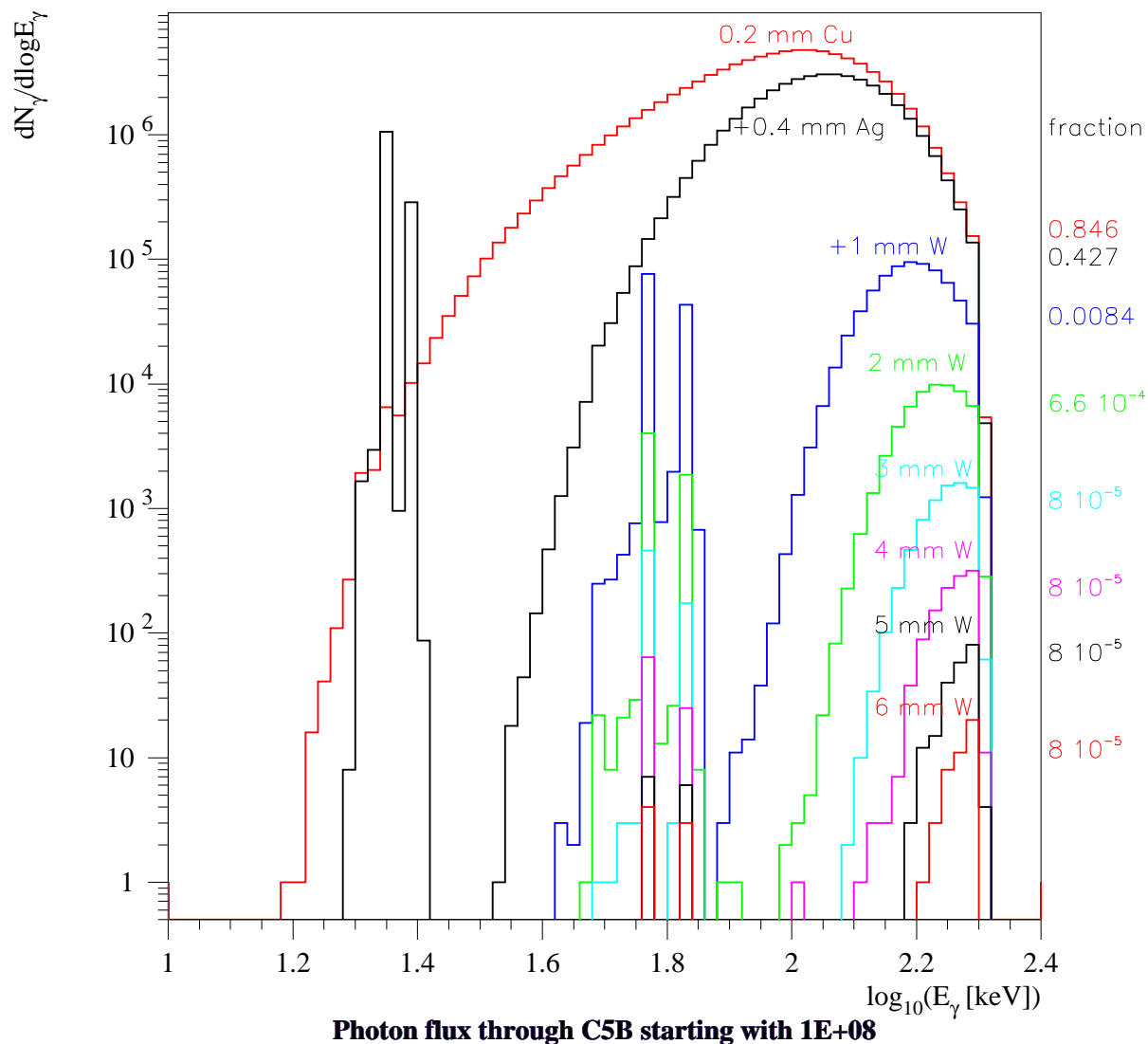


Figure 24: Photon flux at various depths in collimator C5 for the photon spectrum backscattered from the copper absorber ABS4, shown in figure 22. C5B and C5A are made of 2 cm tungsten coated with 0.4 mm silver and 0.2 mm copper to reduce the albedo. The silver fluorescence lines at 22 and 25 keV are absorbed within the first 1 mm of tungsten, while the tungsten K_α and K_β lines at 59 and 68 keV are reduced internally. For a tungsten thickness of 5 mm a fraction of $8 \cdot 10^{-5}$ photons penetrate the collimator.

radiation hits, is shown in figure 27. The Ar and Cu peaks are clearly recognizable. The CJC FADC system has a digital range of up to 16 384 counts, corresponding to about 80 keV. The preamplifier, however, saturates earlier, cutting off the peak of the pulse. This explains the shift and truncation of the “direct” photoelectron peak when compared to the results of the simulation.

3.6 Reducing the Amount and the Effects of Back-Scattered Synchrotron Radiation

The backscattering from C5A into the BST repeater, CIP and CJC can be reduced by a factor

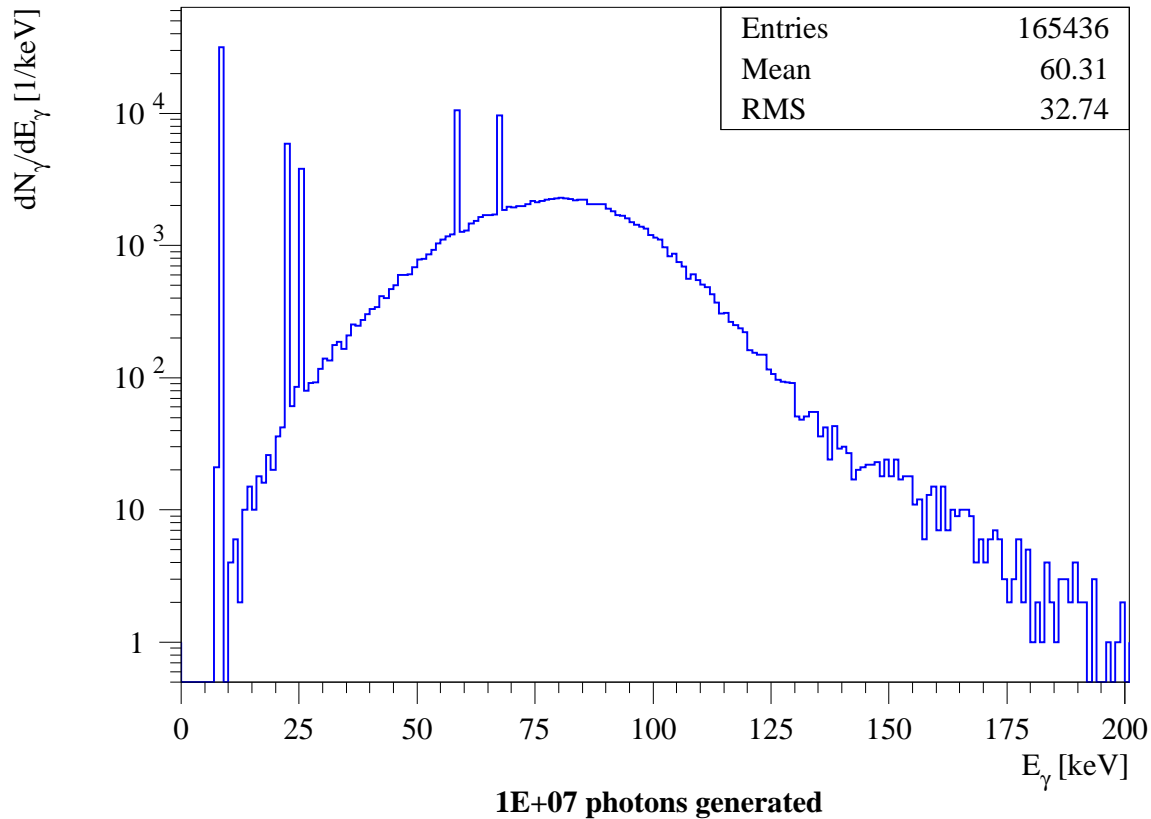


Figure 25: Energy spectrum of photons backscattered from C5A. The source is the photon spectrum from the copper absorber of figure 22. Fluorescence lines from the Cu and Ag coating as well as from the W core are seen, but the spectrum is dominated by the Compton continuum.

of 30 by introducing a 1 mm layer of lead around the backward part of the beam pipe between C5A and C5B. The red curve in figure 26 shows the remaining CJC charge spectrum predicted by the simulation, and figure 28 shows a CAD drawing of the backward part of H1 with the lead inserted.

The fraction of photons backscattered from the main copper absorber at 10.8 m can be reduced by coating its surface. The basic idea is to introduce a medium or high Z material, such as silver or gold, in which the incident photons tend to suffer photo-absorption rather than Compton scattering. The fluorescence photons in turn are absorbed in a thin surface layer of copper. The glancing incidence angle of 40 mrad on ABS4 and the emphasis on backscattering at 180° lead to rather thin coating layers. A 3-D parameter space with a Au-Ag-Cu coating on copper has been searched, and a maximum reduction factor of 1.85 for 15 μm Cu on 45 μm Ag over 20 μm Au on the copper block was found. Without the gold layer, but with a thicker silver layer of 120 μm, a reduction of 1.75 was achieved. The main problem is the mechanical stability of the surface coating under high power loads and large differential thermal expansion; ABS4 has to absorb up to 5 kW of synchrotron radiation power. Additional Ni layers may have to be introduced to improve adhesion. The albedo calculations done with the code of [3] were checked with a GEANT simulation that also includes 3 μm Ni layers and gives a reduction factor of 1.85 ± 0.06 for the Cu-Ag-Au sandwich. The backscattered energy spectrum from pure Cu agrees within 3% for all energies between the two codes.

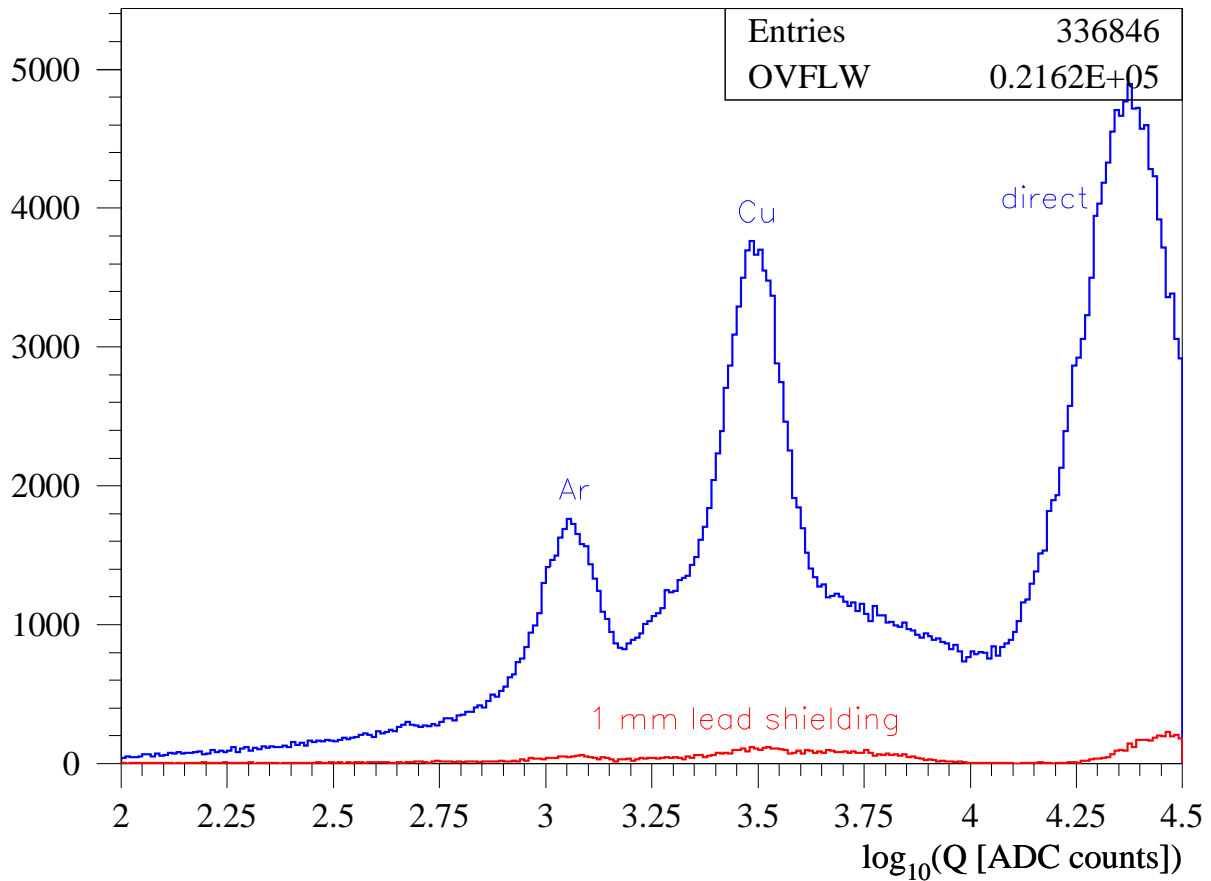


Figure 26: Simulated charge distribution from recoil electrons in argon gas and copper wires. Backscattering from C5A is the photon source. A single-hit dE/dx resolution of 15% was used in smearing the energy deposits. A conversion factor from energy to ADC counts of 375 counts/keV was used. The most probable charge from a minimum ionizing particle is around 450 ADC counts. Full charge collection in the CJC is assumed and the magnetic field is not simulated. The red spectrum shows the effects of 1 mm of lead shielding around the beam pipe in the backward region between C5A and C5B. It reduces the hit rate from this source by a factor of 30.

The flux of backscattered photons into the central detector may also be reduced by additional collimators, e.g. at -3.6 m, just behind the GG magnet. A vertical collimator at this position could be closed to ± 8.8 mm above and below the beams, corresponding to 12σ for the protons at 920 GeV and also leaving sufficient space for the direct synchrotron radiation to escape. However, such a collimator would throw a shadow on the upper and lower regions of C5B only, see figure 23, which are not a major source of radiation in the CJC. A collimator in the horizontal plane would be required to shadow C5A.

3.7 Study of Sources of Synchrotron Radiation Entering the CJC

The design of the HERA upgrade foresees that synchrotron radiation is absorbed at absorbers at 10.8, 19 and 24 m to the right of the experiment (see Fig. 21). A small fraction of the radiation is backscattered into the detector. The collimators C5B, C5A and C4 are designed to protect the beampipe and the innermost detector components against this backscattered radiation. If the e^+

Run 318307 e+ only at 27.5 GeV

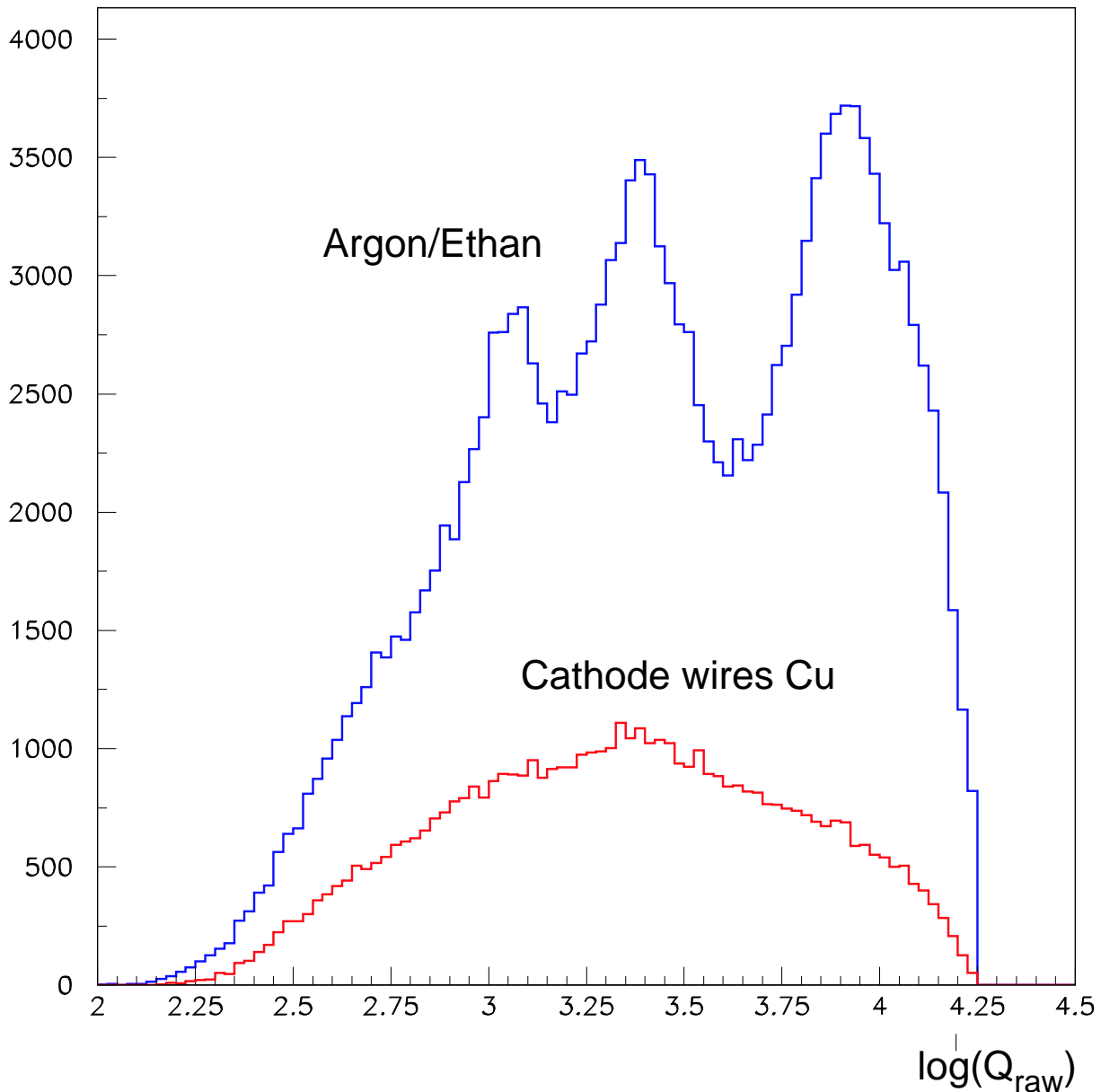


Figure 27: Observed charge distribution in the CJC from low multiplicity events taken with random triggers during running with only positron beams.

beam is not optimally steered, synchrotron radiation can hit other regions along the beampipe and the background increases dramatically. Analysis of the arrival time of this backscattered radiation can help to localize its source. The drift-time of an individual hit depends on the distance of the ionisation to the sense wire. A delayed component to the drift-time spectrum can be identified by the detection of a shifted contribution to the distribution, i.e. by detecting a step in its leading edge. The maximum drift-time in the CJC is about $1.3 \mu\text{s}$. Therefore, to avoid overlap of hits originating from different e^+ bunches, a special positron fill pattern has to be set up with at least one isolated bunch, before and after which there must be a gap of at least 16 empty bunches. For events triggered randomly on this isolated bunch, Fig. 29 shows

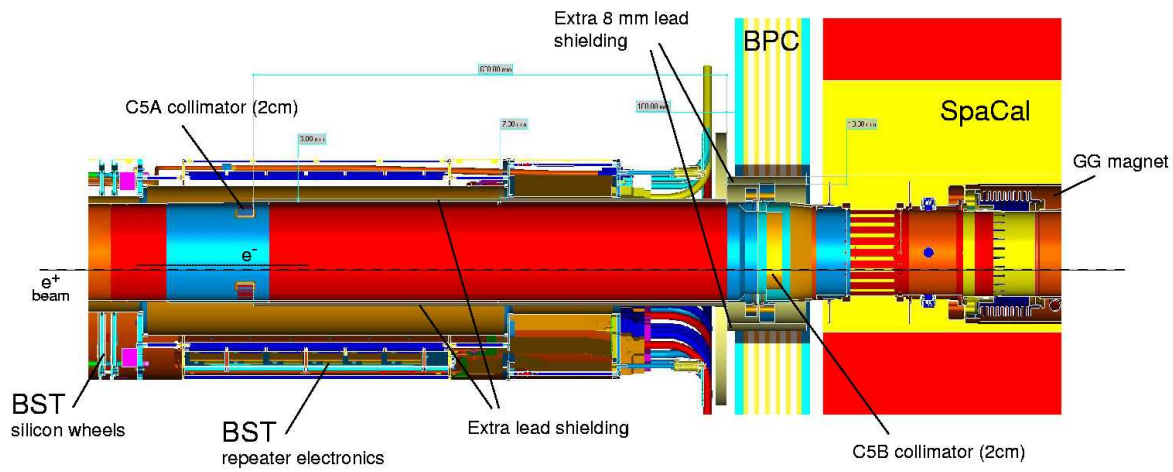


Figure 28: Horizontal section through the rear part of the H1 beam pipe with additional lead shielding.

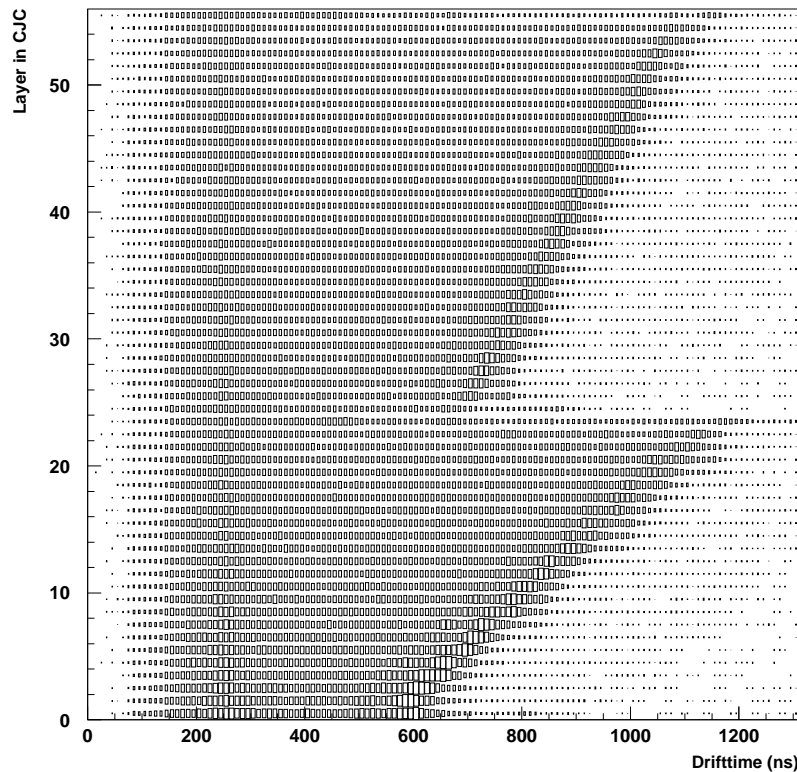


Figure 29: Drift-time versus layer number in the CJC for events triggered randomly on an isolated bunch in a positron-only fill. The twofold trapezoidal shape reflects the geometry of the cell structure of CJC1 (layers 0-23) and CJC2 (layers 24-55).

the expected correlation between drift-time and layer number given by the cell geometries of CJC 1 and CJC 2. The time distribution is flat with the exception of pronounced peaks at small and large drift-times. These peaks can be understood to result from the interactions of the X-ray photons with the field wires ($127\mu\text{m}$ diam. Cu) around the sense wires and the cathode wires ($180\mu\text{m}$ diam. Cu) which define the boundaries of each drift cell (see Fig. 30).

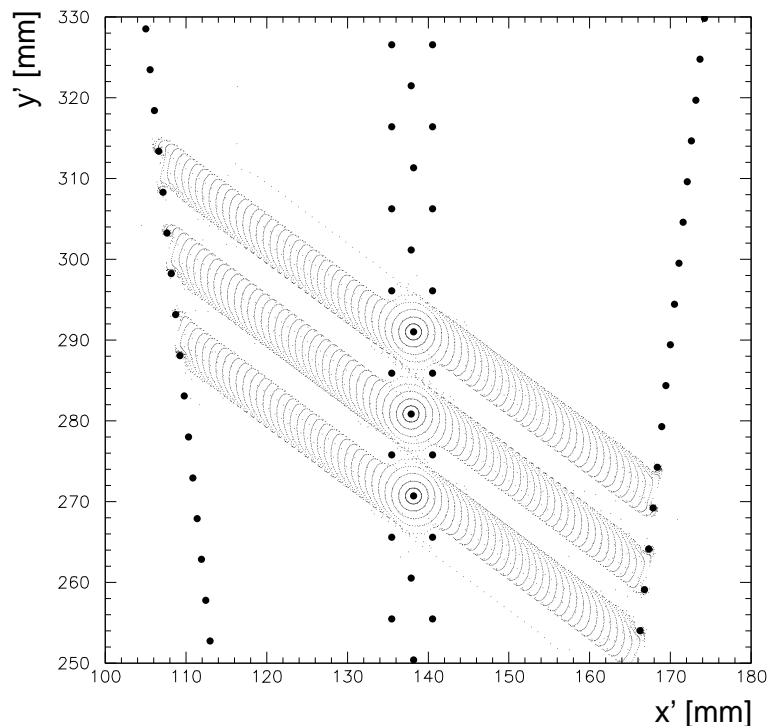


Figure 30: Wire positions and isochrones from a Garfield calculation for part of a CJC1 driftcell.

3.7.1 Comparison of Contributions of Lost Positrons and Synchrotron Radiation

In addition to synchrotron radiation background, off-momentum positrons which have lost some fraction of their energy due to beam gas interactions upstream ($+z$) of the detector can be bent by the dipole field of the GO magnet into the beam pipe, leading to another source of e^+ related background, “lost e^+ ”. This background contribution scales with the e^+ beam current and the upstream pressure in the ring. The upper part of Fig. 31 shows the number of CJC hits per event. The distribution extends to several hundred hits, but is dominated by a peak at small values. For small numbers of hits the distribution is consistent with a Poisson distribution with $\mu = 1.1$ at a positron current of $I_e = 24$ mA. Since these events were triggered on the isolated bunch, this number represents the contribution of one bunch only.

In the following, two event classes are defined by the requirements $N_{hit} < 5$ (synchrotron background) and $N_{hit} > 10$ (lost e^+). The lower part of Fig. 31 shows the hit charge distribution for these two event classes. Events with low hit multiplicity show the pattern expected from the interactions of ~ 80 keV photons with Ar and Cu (see section 2.3) while events with higher multiplicity do not show these characteristic peaks. For the latter events, the enhancement at the largest pulse heights is due to saturation of the FADCs. Hits with very large charge are expected from the interaction of high energy photons (Compton scattering or pair production) emerging from showers caused by the interactions of lost e^+ in the beampipe, the collimators C5A/C5B or the SpaCal calorimeter. Consequently, a large fraction of these events also has energy deposits in the innermost cells of SpaCal (see Fig. 32).

In addition, Fig. 31 shows the pulse height spectrum of hits associated with photon interactions in the Cu wires. Since electrons liberated in these interactions lose energy in the wire

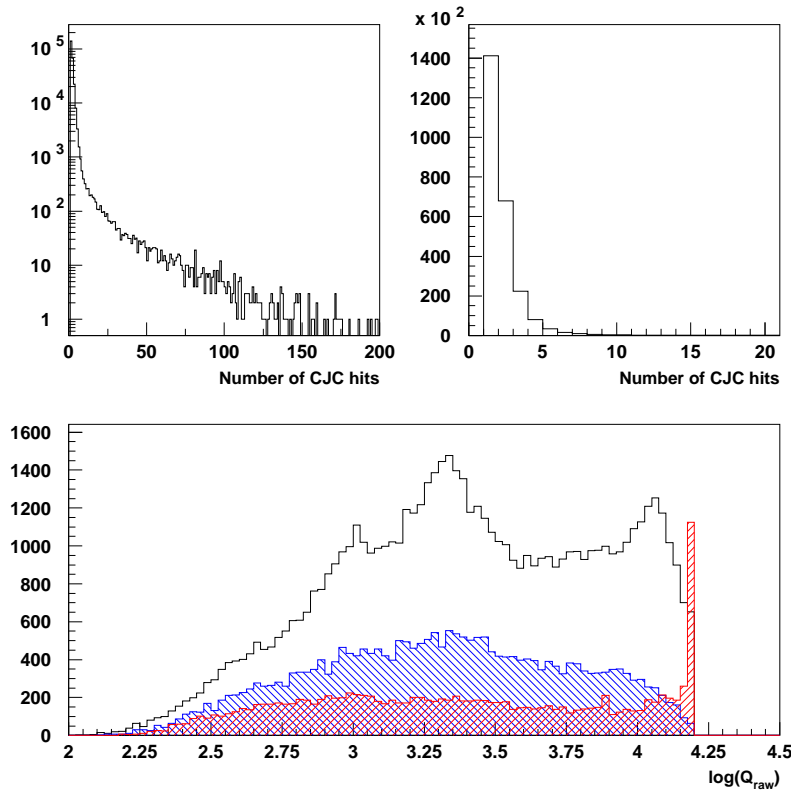


Figure 31: Top: number of hits in CJC on a logarithmic (left) and a linear (right) scale. Events with no hits are not shown in the distributions. Bottom: hit charge for synchrotron radiation hits from the gas (open), cathode wires (left hatched) and for hits from lost e^+ (right hatched).

before they reach the sensitive gas volume, the peak structure which is observed for direct interactions in Ar is completely smeared out.

For a long e^+ fill on September 11th 2002, which was very well steered in terms of background optimisation, the leading edge of the drift-time spectrum is shown in Fig. 33 for the two event classes. The reference T_0 is defined by in-time events which are caused by lost e^+ . These events lead to a rectangular time distribution. A clear shift of the distribution is seen for hits from synchrotron radiation which sit on a small remaining in-time contribution. The time delay of the first significant step at $\simeq 65$ ns agrees very well with the expectation for a source of backscattered radiation at 10.8 m (absorber 4 at GM magnet, see Fig. 21) which is indicated by an arrow. A second step occurs at $\simeq 110$ ns, consistent with a source at 18 m (GN magnet). A possible delayed contribution from the 24 m absorber at 144 ns cannot be detected because of the presence of a dominant peak at about 120 ns after the first step which matches well the expected drift-time for the 6 mm distance between the field wires and the sense wires (see Fig. 30) given the drift velocity of $50\mu\text{m}/\text{ns}$ in the CJC gas.

In this fill no significant contribution from backscattering from absorbers 1 to 3 at distances of 3.5 to 8.2 m is present. The relative amounts of backscattering from the 18 m and 10.8 m absorbers agree roughly with the expectation [4].

To investigate whether the level of this background is irreducible and therefore has to be tolerated or if it can be reduced by improved shielding, the location of hits in the CJC can be

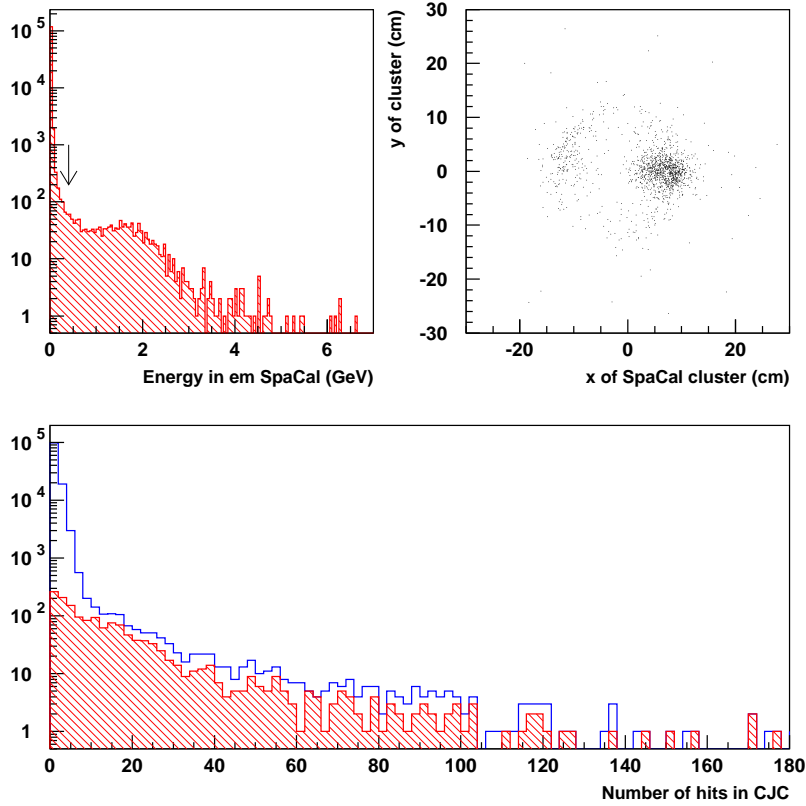


Figure 32: The upper plots show the energy deposited (left) and the reconstructed cluster position (right) in the electromagnetic SpaCal in randomly triggered events. The lower plot shows the hit multiplicity in the CJC without (open) and with (hatched) the requirement that there be energy deposition $E_{SpaCal}^{em} > 400$ MeV in the SpaCal.

measured and compared with simulations. Fig. 34 shows reconstructed hit positions in z and ϕ for hits in CJC 1 for the two event classes. While some features, like an enhancement at $-z$, can be qualitatively understood from backscattering from C5A or “sneak-through” underneath the backward proportional chamber (BPC) other features still have to be investigated in more detail in order to optimise the design of additional shielding in the backward direction.

3.7.2 Contributions of Synchrotron Radiation and Lost Positrons to Currents in the CJC

As described in section 2.3, the background from synchrotron radiation alone is proportional to the positron current I_e , while the contribution from lost e^+ depends in addition on the pressure to the left of the experiment which increases as the positron current rises, leading to a quadratic dependence on I_e . Therefore, the ratio of the contribution of the CJC current from particle losses, $I_{lost\ e^+}$, to that from synchrotron radiation I_{synrad} , is expected to rise linearly with the positron current in the machine.

The expected positron induced current in the CJC can be derived from the sum of all hit charges per event according to:

$$I_{CJC} = d \cdot N_T^{e^-} \cdot G \cdot e \cdot \frac{\langle Q_{hit} \rangle}{Q_{mip}} \cdot \frac{1}{T} \cdot \frac{N_b^{filled}}{220} \quad (3)$$

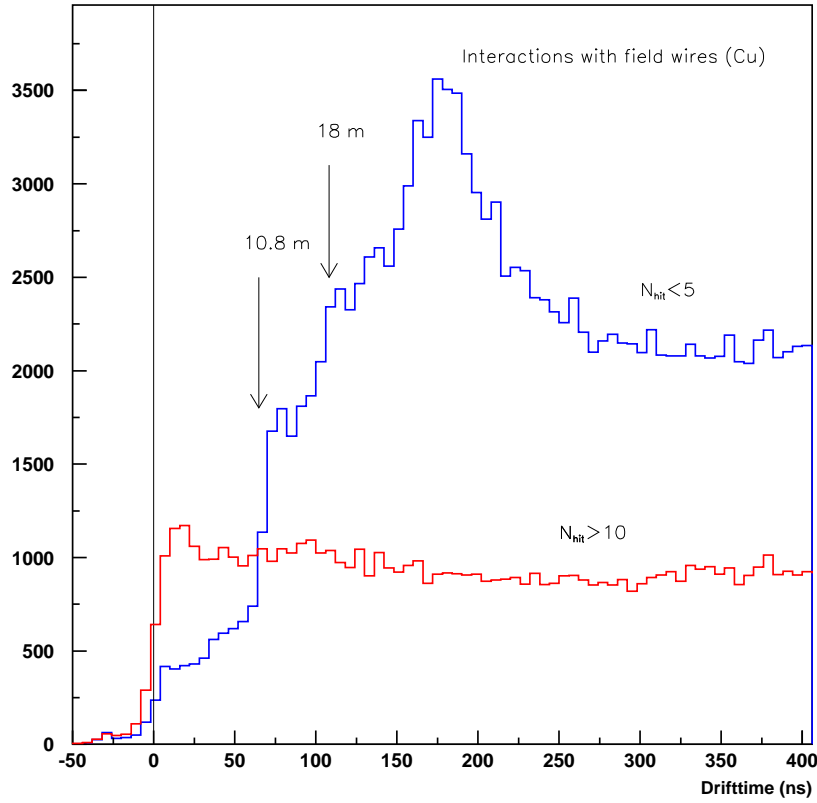


Figure 33: Drift-time distribution for events from lost e^+ ($N_{hit} < 5$) and synchrotron radiation ($N_{hit} > 10$). The arrows indicate the time delay expected for photons backscattered from the absorbers at 10.8 m and 18 m.

with:

$d = 0.7$ cm, active part of drift region per layer of CJC.

$N_T^{e^-} = 100/\text{cm}$, ionisation yield per cm in Ar/C₂H₆ for a m.i.p.

$G = 8 \cdot 10^4$, gas gain in CJC.

$e = 1.6 \cdot 10^{-19}$ C, elementary charge.

$\langle Q_{hit} \rangle = 3563$ total average charge per event from hits in CJC (run 322432).

$Q^{mip} = 410$, average charge per hit for m.i.p.

$T = 100\text{ns}$, active time per triggered event.

$N^{filled} = 181$, number of filled bunches (run 322432).

Note that the value of the gain in the CJC is not known very precisely. Using the numbers given above the calculated sum of currents in CJC 1 and CJC 2 for run 322432 is $\simeq 65\mu\text{A}$ which has to be compared with the pedestal corrected measured value of $\simeq 75\mu\text{A}$.

Using the above definition of lost e^+ and synchrotron radiation events, the contributions these event types make to the total current can be determined using equation 3 if the appropriate values are inserted for $\langle Q_{hit} \rangle$. Fig. 35 shows the ratio of the separate contributions as a function of the positron current. Within the experimental uncertainty a linear rise is indeed observed for both CJC1 and CJC2. The slope of this curve is a measure of the present positron current induced pressure increase on the left side of the experiment while the intercept with the y -axis is proportional to the base pressure in the machine, $\alpha_e P_0^L / \alpha_{SR} \simeq 0.05$. The extrapolation to the design current of 55 mA yields a ratio of roughly 1:1 which, within a factor of less than 2, agrees with the estimate derived from the parabolic fit to the total current versus I_e in section 2.3.

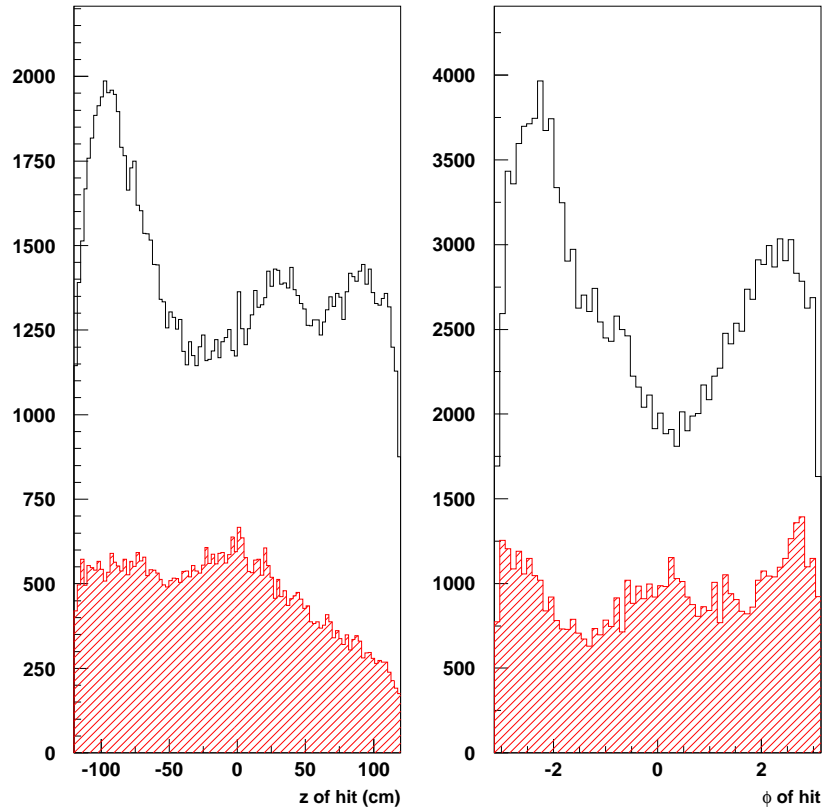


Figure 34: Reconstructed positions of hits in CJC 1 for synchrotron radiation (open histogram) and particle losses (hatched) along the wire and in azimuth. The center of the HERA ring is in the direction $\phi = 0$.

3.7.3 Particle and Synchrotron Radiation Induced Background During Electron-Proton Running.

The above method of separating synchrotron radiation from particle background can also be employed for luminosity conditions. For this purpose several random trigger runs were taken during a luminosity fill on September 8th 2002, starting with 20 mA of positrons on 20 mA of protons. Background conditions were initially good but degraded during the fill and then improved again towards the end of the fill. Fig. 36 shows the measured and calculated currents in CJC 1 and CJC 2 together with the decomposition into the contributions from particles and synchrotron radiation. The particle contribution is dominantly from p -gas interactions with a small component from lost e^+ . The time variation of the total current can be reasonably well described. The particle contribution falls monotonically with time whereas the mis-steering of the e^+ beam can clearly be seen in the increased fraction of synchrotron radiation background in the middle of the fill. The synchrotron radiation background conditions at the beginning of the fill correspond to the conditions of the e^+ -only fill discussed above and were taken for 20 mA positron current on 20 mA proton current. Under these conditions the synchrotron radiation contributes roughly 1/3 to the total chamber current, in agreement with the expectation from equation 1 using the parameters derived from the parabolic fit to the total chamber current.

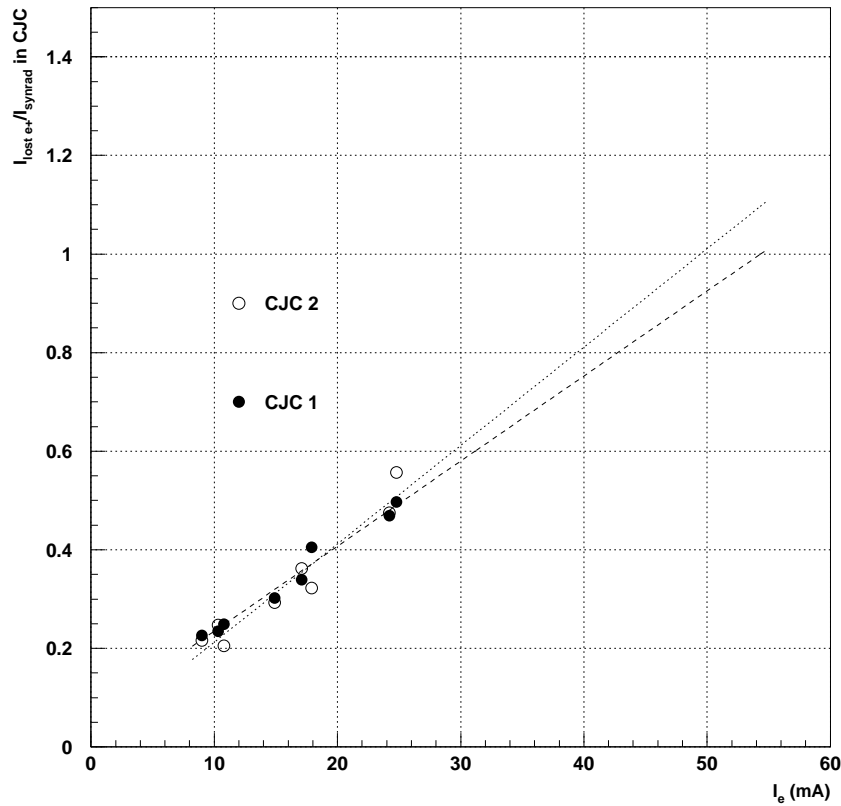


Figure 35: Ratio of the contributions to the total CJC current from lost e^+ and from synchrotron radiation as a function of the positron current.

3.8 Summary

The majority of the synchrotron radiation which enters the H1 detector, the properties of which are well understood, is backscattered from absorbers to the right of H1, in particular absorber 4 at 10.8 m from the interaction point. C5A and C5B, the 20 mm thick tungsten collimators designed to absorb this radiation could be reduced to a thickness of 5 mm without noticeable loss of performance, thereby reducing the amount of material presented to hadrons generated in proton beam-gas interactions and reducing the rate of re-scattering of these hadrons. Adding lead shielding allows adequate protection of the sensitive electronics of the BST and the rear of the CJC. This may be of particular importance during the injection and acceleration of the positron beams, during which period monitoring of the synchrotron radiation dose is not possible.

The positron beam can also induce background if positrons suffer collisions with the beam-gas and thus lose momentum. They can then be deflected into the beam pipe within the H1 detector. The CJC currents induced by this background source are found to be roughly the same as those caused by synchrotron radiation.

The studies reported here have all been performed using positron beams. It is important that simulations be performed of the situation with electron beams, to ensure that the results obtained here are apply also in this case.

Lumi Fill 100

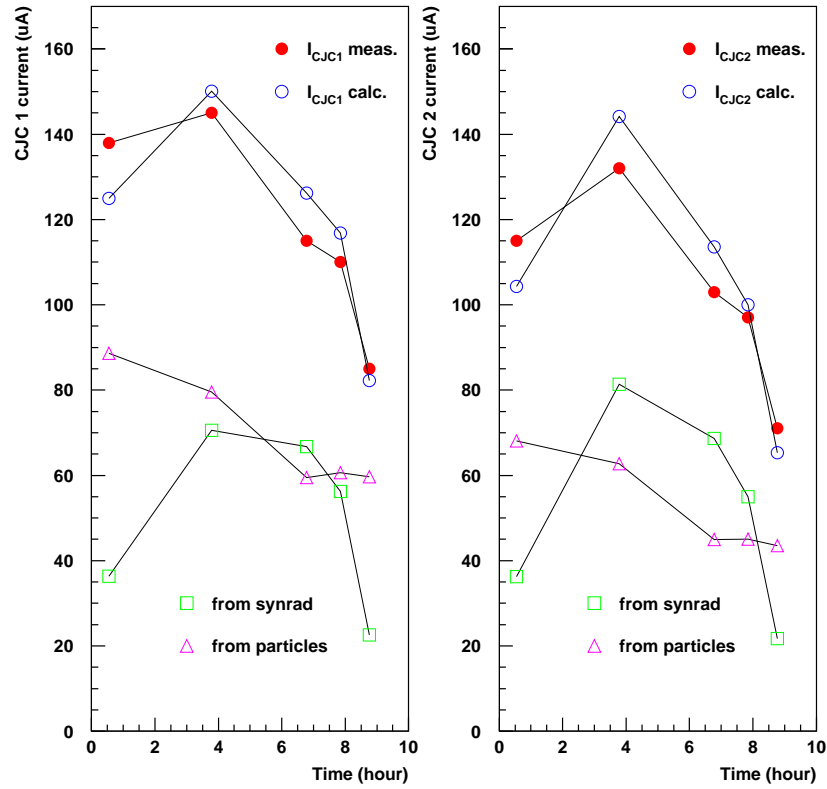


Figure 36: Measured and calculated CJC currents and their decomposition into synchrotron radiation and particle induced backgrounds versus time for a luminosity run taken on 8.9.02. At the start of the run, the positron and proton currents were both 20 mA.

4 Proton Induced Background

4.1 Introduction

As already demonstrated in this report, proton induced background is a major cause of the large currents drawn in the CJC under the present HERA operating conditions. Fig. 37 shows an example of a proton induced event. These typically contain lots of tracks at shallow angles.

As Figs. 38 and 39 show, the proton induced background has two distinct components:

- A component in which the particles originate from the beam pipe wall or the collimators C5A and C5B at $z = -80$ cm and -145 cm, respectively. This component is attributed to the re-scattering in the collimators and the beam pipe of particles produced in upstream beam-gas interactions.
- A component in which the interaction between the beam proton and the residual gas nucleus happens within the H1 interaction region. In this case, some of the reaction products are observed directly in the H1 detector.

Extensive Monte Carlo studies were conducted in order to quantitatively understand the origin and properties of these background sources. The Monte Carlo simulations were compared with data taken in a number of special runs with only proton beams in HERA, at various proton energies.

There is no evidence that so-called beam-wall events, in which beam protons interact directly with the material of the collimators or beam pipe in the H1 interaction region, contribute significantly to the backgrounds in H1.

A further potential source of background, namely upstream beam-wall interactions of protons, especially in the half quadrupoles at 11 m, has not yet been studied. (Here we refer to protons from the beam or the beam halo that hit aperture limitations in the machine.)

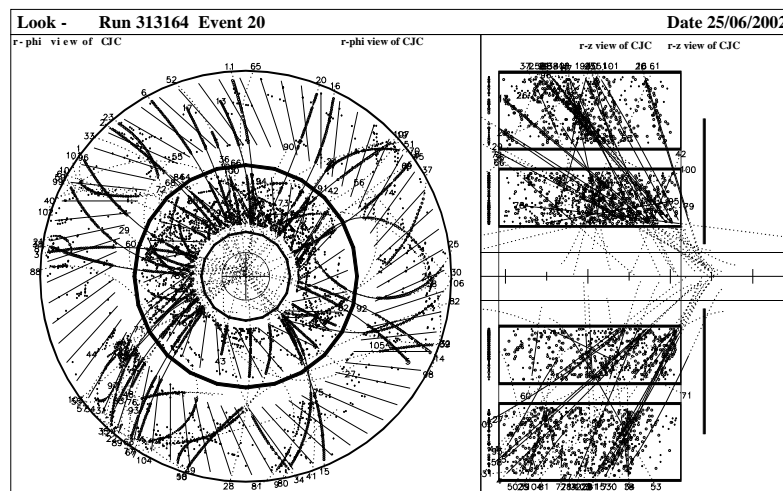


Figure 37: A typical proton background event with a vertex in the C5B collimator.

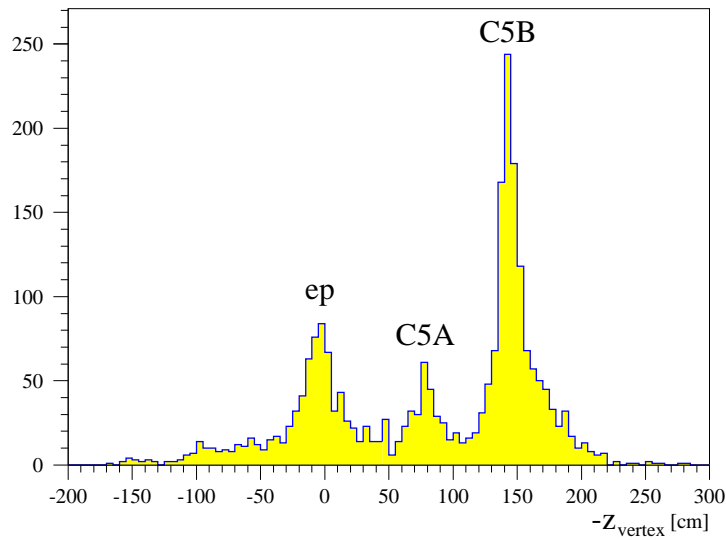


Figure 38: Distribution of the reconstructed z position of the interaction vertex for a luminosity run. Peaks at the positions of the collimators C5A (-80 cm) and C5B (-145 cm) are clearly visible. The precise height of the different peaks depends heavily on the beam conditions and the trigger mix.

Date	Energy [GeV]	Current [mA]	H1 Runs	Rate [kHz]	Currents CJC1/2 [μ A]
20.8.02	70	55	320476-78	3.0	15 / 21
20.8.02	150	50	320480-83	2.9	17 / 22
20.8.02	300	50	320488-93	3.4	20 / 25
20.8.02	455	49	320499-500	3.8	25 / 27
20.8.02	677	49	320507-510	4.4	30 / 30
29.8.02	677	42	320981-983	3.7	25 / 27
29.8.02	920	42	320985	4.1	31 / 31
30.8.02	920	48	321068	8.7	60 / 55
4.9.02	920	28	321605	4.0	30 / 30

Table 1: Characteristics of the various proton-only runs used for the studies presented in this chapter. The column “Rate” refers to the DCR_φ track trigger rate.

4.2 Data Samples used in Investigation of Proton Beam-Gas Scattering

In the period between 20.8.02 and 4.9.02 a number of special runs were taken with only protons in the HERA machine, as summarized in Tab. 1. In particular, on 20.8.02, data were taken at different proton beam energies. After each change of beam energy, background conditions were optimized by the HERA shift crew, as illustrated for one run in Fig. 40. During these runs, the central drift chamber (CJC) was at full high voltage.

Data was taken mainly with a track trigger, DCR_φ , which triggers events with at least one track of transverse momentum $p_t > 450$ MeV, a distance of closest approach to the beam line of $D_{CA} < 2$ cm and a sufficiently large radial length. The latter condition is fulfilled by particles originating at the interaction point if they have a polar angle in the range $20^\circ < \theta < 160^\circ$.

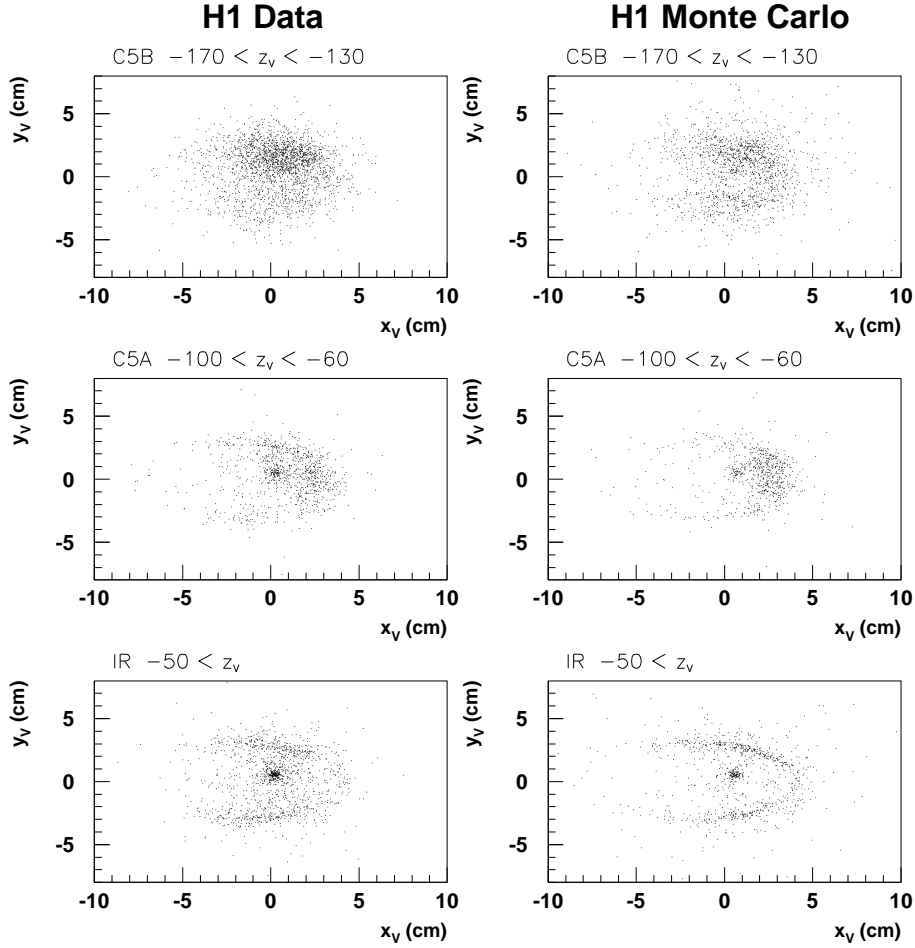


Figure 39: Distribution of the reconstructed vertex positions in the $r\phi$ plane for a proton-only run for different regions of the vertex in z (left data, right Monte Carlo): top, z values around C5B (-145 cm); middle, z values around C5A (-80 cm); bottom, z values around the interaction point. A marked up-down asymmetry is visible, especially in the vertex distribution around the C5B collimator. We attribute this to a misalignment between HERA and H1, which causes the beam to lie approximately 6 mm above the central axis of H1. The Monte Carlo simulation on the right side contains this y shift, and consequently shows a similar asymmetry. Studies have shown that the overall rate of proton induced background is rather independent of this shift, and subsequent simulations were done without it.

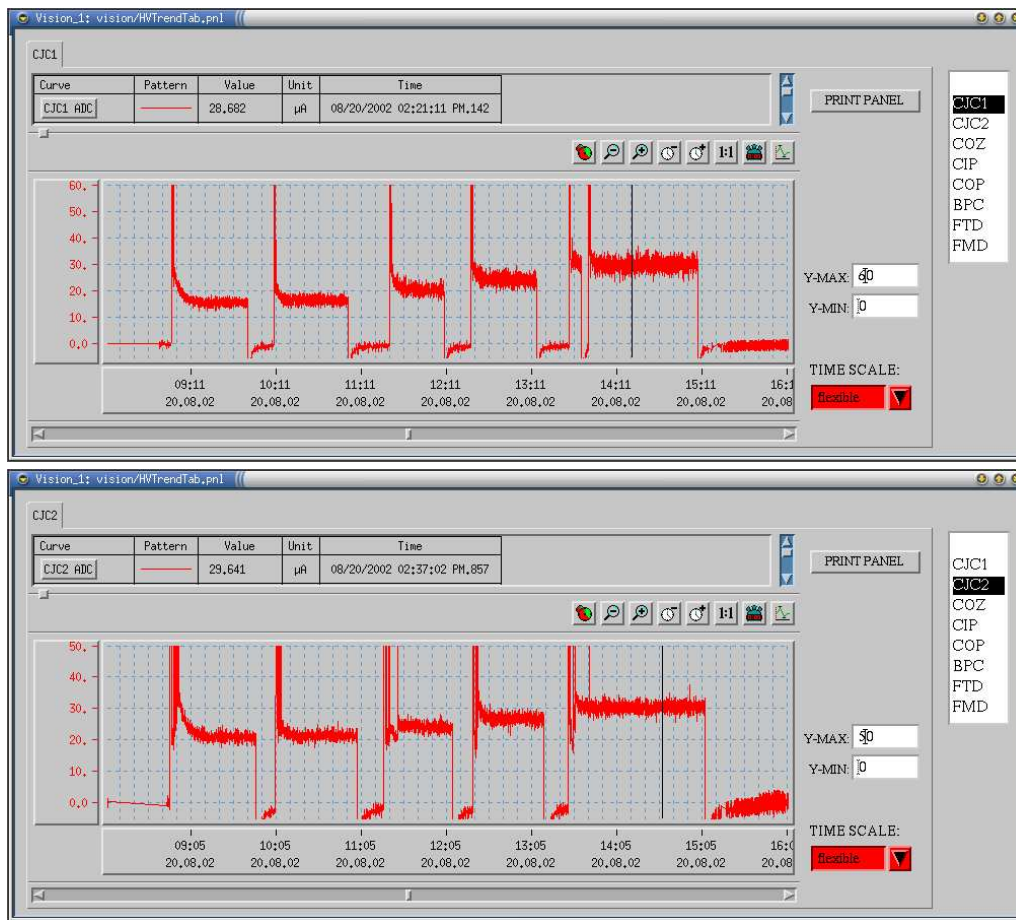


Figure 40: Variation of the current in the inner and outer central drift chambers, CJC1 (top) and CJC2 (bottom), respectively, as a function of time during a proton-only run on 20.8.02. It can be seen that the chamber current increased with each step in proton energy, and remained at an increased level even after optimization. The proton energies were 70, 150, 300, 455, and 677 GeV.

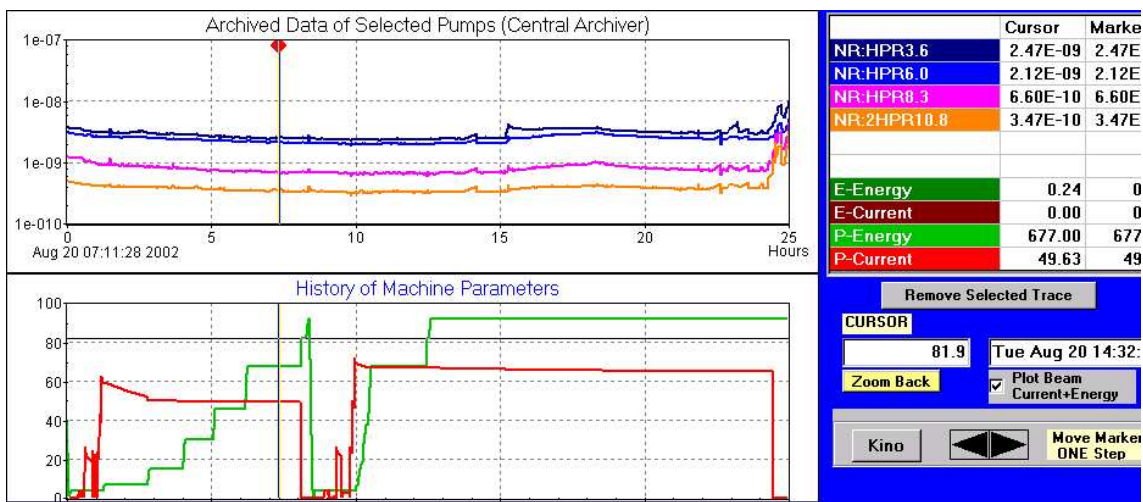


Figure 41: Variation of the pressure in the beam pipe and the proton beam current and energy during the energy scan performed on 20.8.02.

Beam Energy [GeV]	Total	Cross Sections [mbarn]					Nondiffractive	
		Elastic	Beam dissoci.	Target dissoci.	Double diffract.	Low- p_t	Inelastic (QCD)	
PYTHIA process:		91	92	93	94	95	11, 12, 13, 28, 53, 68	
148	38.59	6.73	3.27	3.27	1.11	20.61	3.62	
298	39.39	6.79	3.57	3.57	1.52	18.71	5.22	
450	40.07	6.90	3.74	3.74	1.76	17.60	5.69	
675	40.86	7.04	3.89	3.89	2.00	16.53	7.54	
920	41.55	7.17	4.00	4.00	2.18	15.74	8.47	

Table 2: The Pythia Monte Carlo samples used in the study of upstream beam gas interactions.

4.3 Monte Carlo Simulation of Beam–Gas Scattering

The Monte Carlo simulation of beam–gas interactions has four important ingredients:

- The simulation of proton–proton and proton–nucleus interactions using an appropriate event generator.
- Realistic modelling of the vertex distribution of the primary beam–gas interactions.
- The proper description of the material distribution in the accelerator.
- The implementation of the magnetic fields of the machine.

These topics will be briefly discussed in the following sections, before the results of the simulation are compared with measurements.

4.3.1 Modelling of Proton–Proton and Proton–Nucleus Interactions

The composition of the residual gas within the beam pipe is not well known. However, it is likely that in addition to hydrogen, the residual gas contains heavier components such as carbon, nitrogen or oxygen. The collisions of protons with energies ranging from 148 to 920 GeV with hydrogen nuclei (i.e. protons) were simulated using Pythia 6.157 [5]. Tab. 2 summarizes the resulting cross section predictions for various beam energies.

Collisions of 920 GeV protons with heavier nuclei, here represented by carbon, were modelled using the Fritiof event generator [6].

4.3.2 The Simulation of Dead Material, Magnetic Fields and the Vertex Distribution

For the purposes of this study, the GEANT description of H1 was extended to cover the region up to 110 m upstream of the detector. Part of the beam line had already been implemented for the study of the luminosity measurement, but large parts of the proton beam line had to be added. Figs. 42 and 43 show the backward region of H1, as incorporated in the GEANT

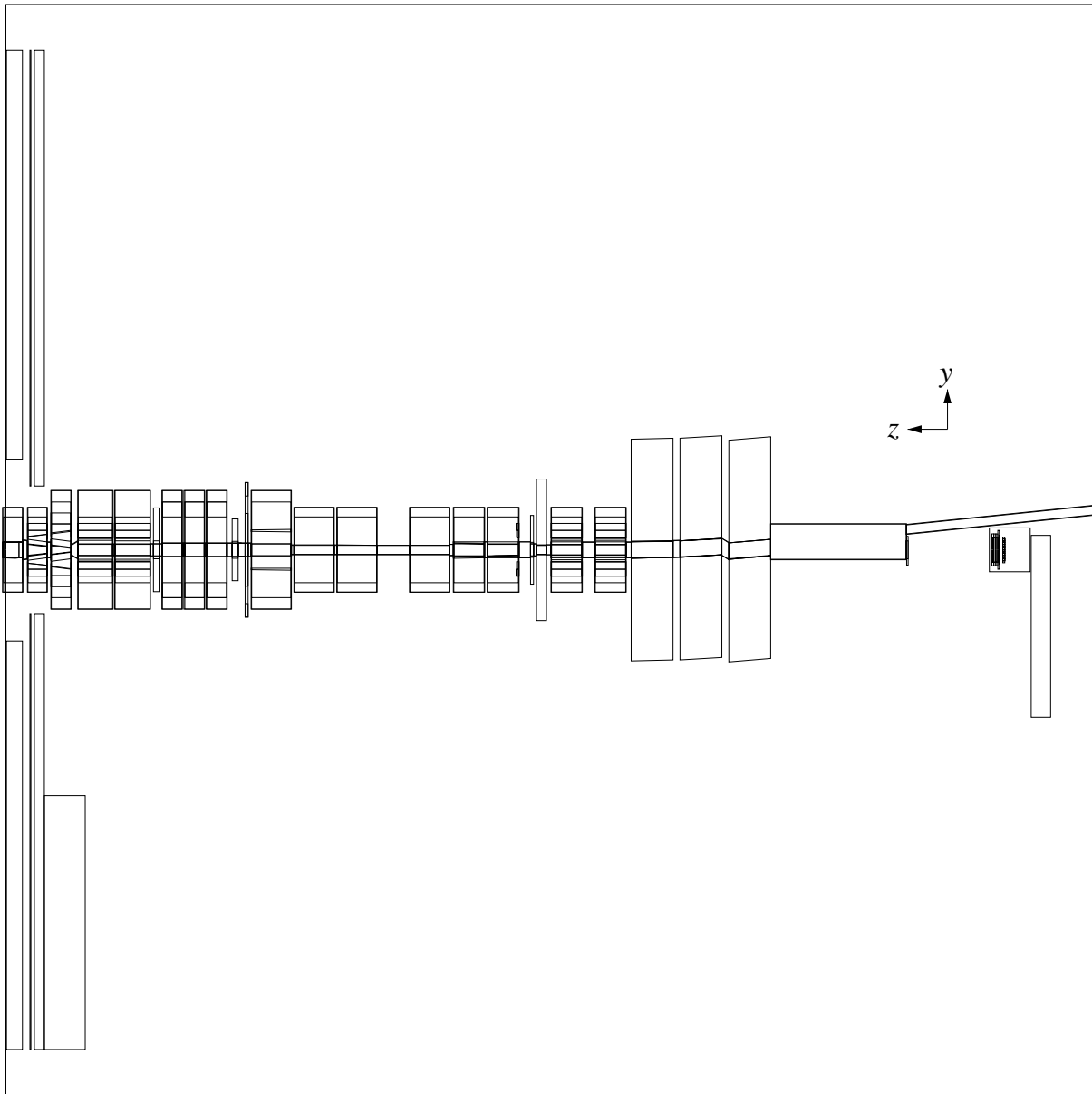


Figure 42: Horizontal section through the region $z = -3.6$ m to -110 m behind the H1 detector, showing the beam line components incorporated in the GEANT simulation.

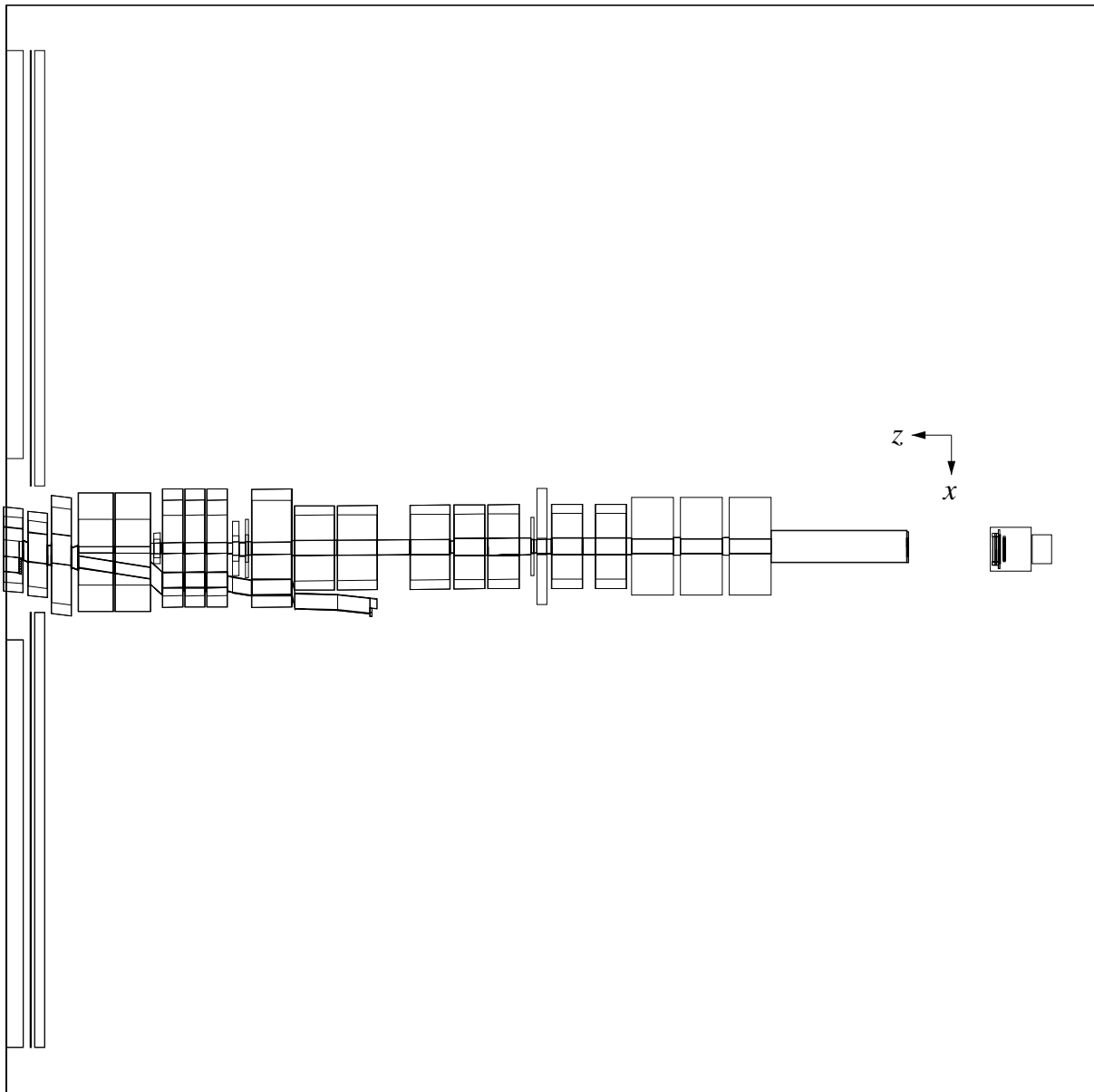


Figure 43: Vertical section through the region $z = -3.6$ m to -110 m behind the H1 detector, showing the beam line components incorporated in the GEANT simulation.

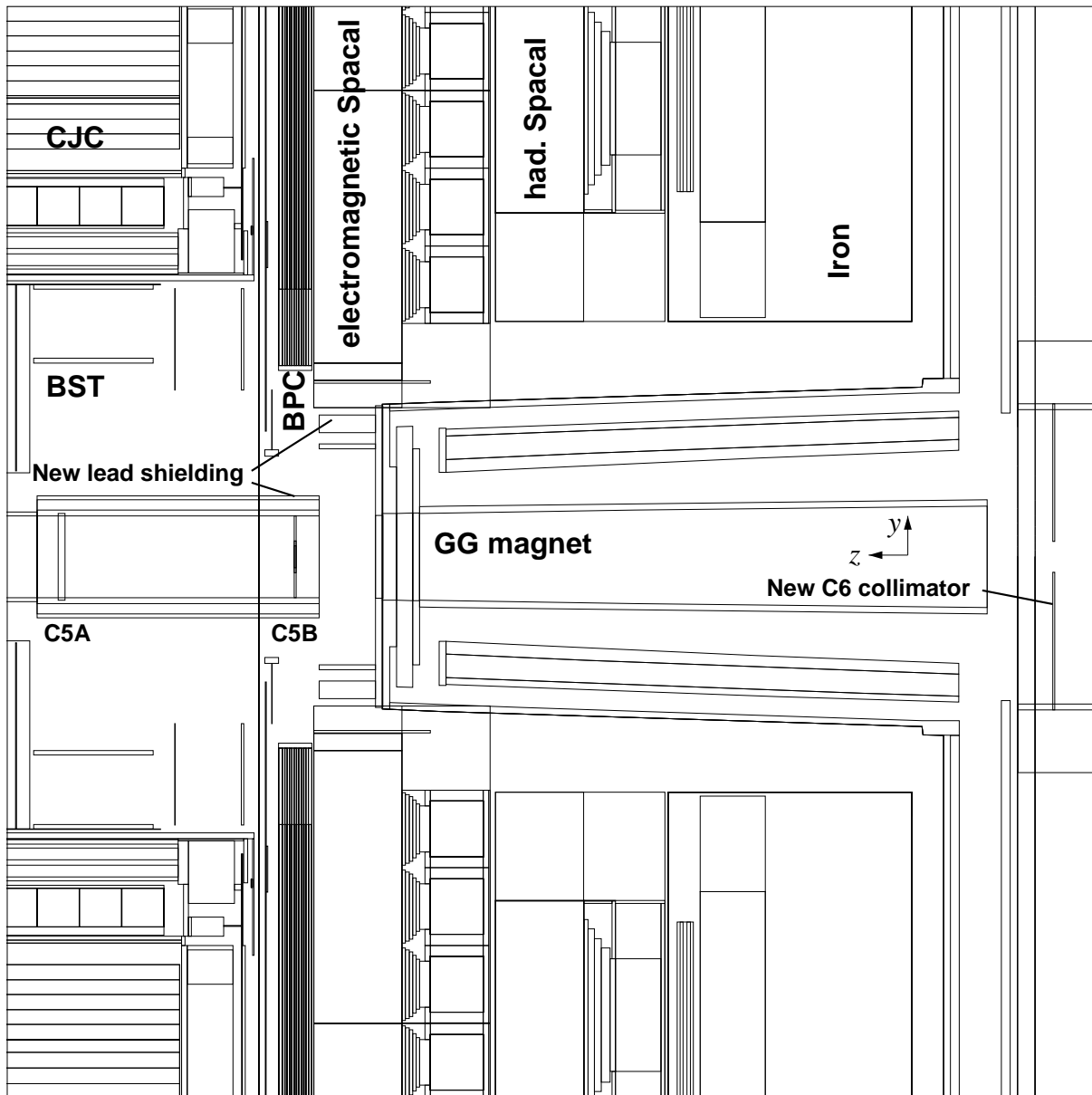


Figure 44: The position of the new C6 collimator and the additional lead shielding in the backward region of H1, as implemented in the GEANT simulation

Name	Generator	Target	E_p	z distrib.	C5B	Lead	C6
A	Pythia	p	920	-63... + 1 m flat	2 cm		
B	Pythia	p	298	-63... + 1 m flat	2 cm		
C	Pythia	p	920	-63... + 1 m flat	0.5 cm		
D	Pythia	p	920	-63... + 1 m flat	0.5 cm	yes	
E	Pythia	p	920	-63... + 1 m flat	0.5 cm	yes	yes
F	Fritiof	$^{12}_6\text{C}$	920	-63... + 1 m flat	2 cm		

Table 3: Monte Carlo samples used for the proton gas background simulation. The column labelled “C5B” shows the thickness of the C5B collimator; “Lead” indicates whether additional lead shielding, as depicted in Fig. 44, is present; “C6” shows the presence or otherwise of the proposed C6 collimator at $z = -3.6$ m. Sample A is the reference sample with the existing geometry. Sample B illustrates the effect of a lowered beam energy. Samples C to E show the effects of various possible changes to the detector geometry. Sample F is used to study the possible influence of the gas composition on the results.

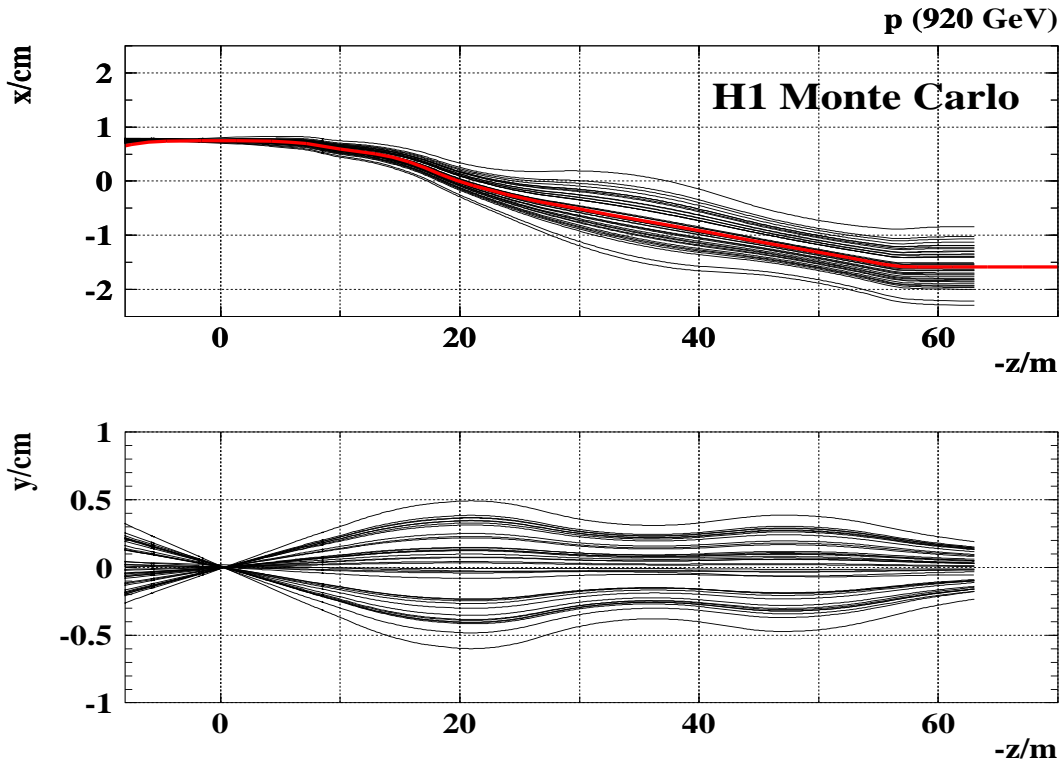


Figure 45: Trajectories of 920 GeV protons (upper plot xz plane, lower plot yz plane) starting at -63 m. The protons were initially generated with the nominal beam energy and no transverse momentum. The transverse momentum and starting point were then distributed according to the beam optics and the protons were tracked by GEANT through the magnetic fields of the HERA machine. The central thick line in the upper plot indicates the design orbit of the protons in the horizontal plane. In the vertical plane (lower plot) the design orbit in the region considered is at $y = 0$.

simulation. Fig. 44 shows a section through the backward region of the H1 detector in which some possible detector modifications have been implemented. Several configurations of the detector were simulated, as summarized in Tab. 3.

The magnetic fields of the proton magnets were also incorporated in the simulation. These were taken from the output of the PETROS program for the optics hp1920e+ that was kindly provided by the HERA machine group.

The primary event vertices were distributed in z along the nominal proton beam orbit and the vertex distribution in the xy plane was generated according to the known beam emittance, $\epsilon = 5.7 \cdot 10^{-9} \text{ m} \cdot \text{rad}$ (corresponding to a normalized 2σ emittance of $21\pi \text{ mm mrad GeV}$), and the β function calculated using the PETROS program. The events were also rotated such that the direction of the initial beam proton was tangential to the beam direction.

Fig. 45 demonstrates the accuracy of this procedure. Protons distributed as expected from the beam optics at $z = -63 \text{ m}$ were tracked to the interaction point. The simulated beam is seen to follow the design orbit and its envelope agrees well with the results of calculations based on the beam optics provided by the machine group.

Two different possibilities exist for the simulation of the z coordinate of the proton beam–gas vertex:

- A flat vertex distribution can be generated between two z values.
- The vertex distribution can be generated proportional to the measured pressure profile in the beam pipe.

In the second case, the pressure profile given in Tab. 5 was used. It was assumed that the pressure rises or falls exponentially (rather than linearly) between two measurements.

The simulated events were passed through the standard H1 event reconstruction program.

4.3.3 Properties of the Primary Interactions

Fig. 46 shows how the proton–proton (pp) and proton–nucleus (pC) interactions differ at the generator level, for a proton beam energy of 920 GeV. The multiplicity distribution of proton–nucleus interactions has a tail to much larger values than for the proton–proton case, as is to be expected¹.

4.3.4 Properties of Events Observed in H1

The above Monte Carlo was used to investigate the properties of the events which cause backgrounds in H1. Fig. 47 shows the energy spectrum of particles that suffered re-scattering in a collimator or the beam pipe and caused at least one track in the CJC. These particles are produced in primary pp collisions upstream of H1. It is interesting to note that very few 920 GeV particles cause activity in the detector, although in about 25% of all events (c.f. Tab. 2) the beam proton scatters elastically in the primary interaction. The mean energy of the particles

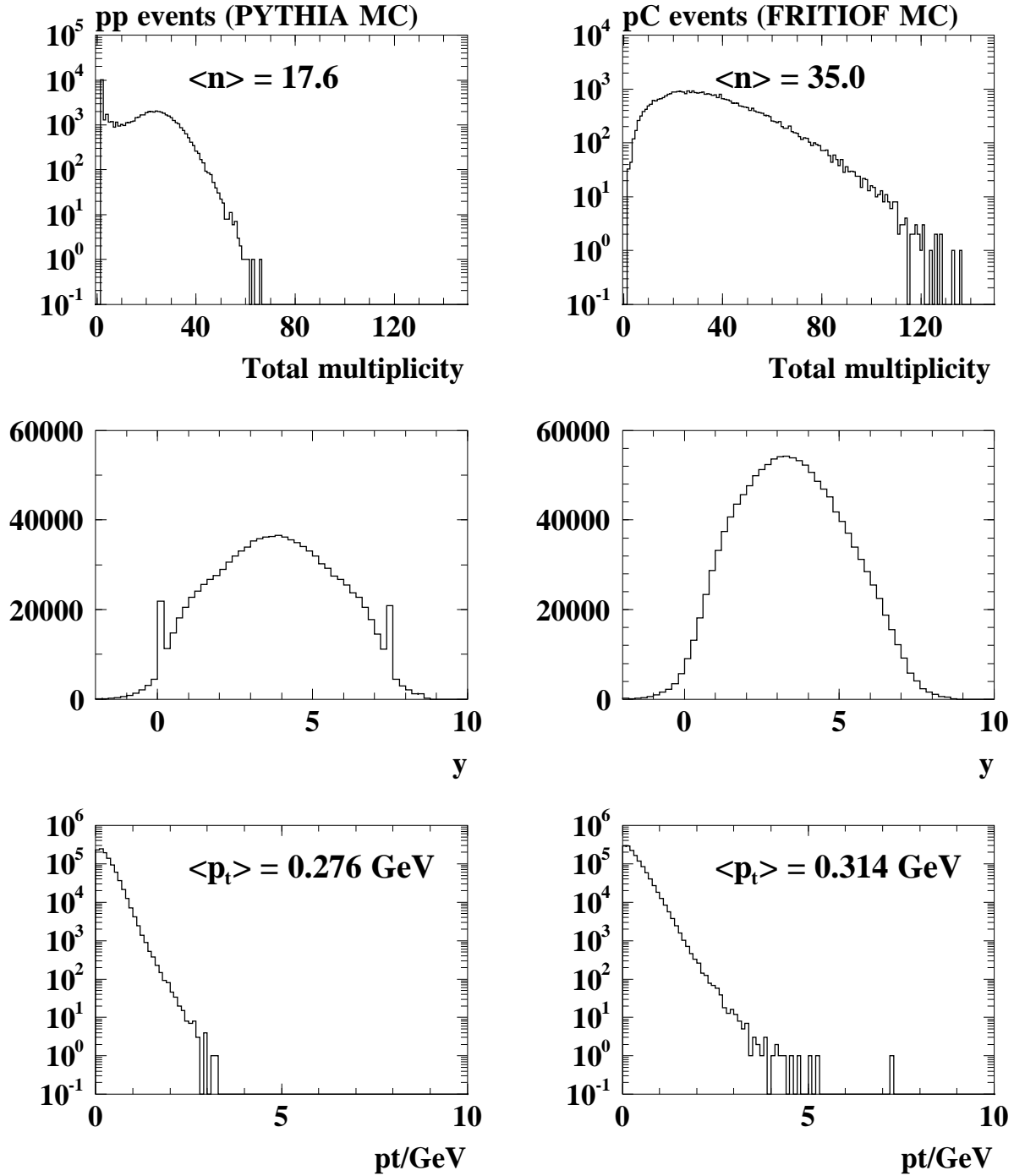


Figure 46: Comparison of proton–proton (left) and proton–carbon (right) scattering events: top, total number of generated stable particles; middle, rapidity distribution of generated particles (the peaks at $y = 0$ and $y = 7.5$ in the pp case are due to elastic scattering); bottom: transverse momentum.

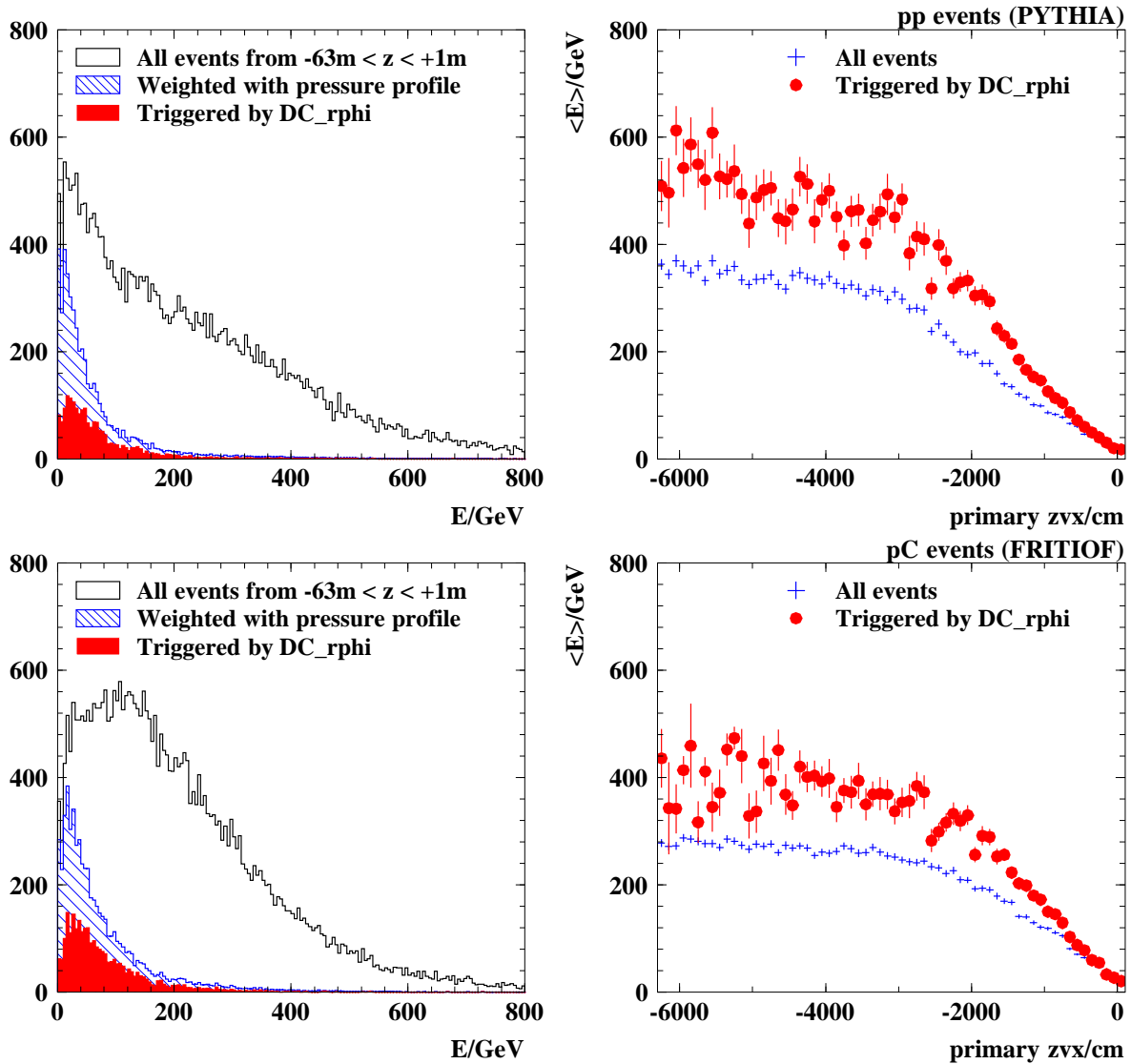


Figure 47: Comparison of proton–proton (top) and proton–carbon (bottom) events. Left, energy spectra of particles that suffer re-scattering in the beam pipe or one of the collimators which leads to some activity within the H1 detector; open histogram, all events, flat pressure profile; hatched histogram, realistic pressure profile (i.e. most events originate less than 20 m away from the interaction point); solid histogram, track triggered events. Right, mean energy of particles that cause a secondary interaction in the beam pipe or one of the collimators as a function of the z position of the primary interaction; crosses, all events; circles, track triggered events.

that undergo re-scattering is around 300 to 350 GeV for interactions that happen more than 20 m upstream.

Between $z = 0$ and $z = 20$ m, the proton beam deviates through about 1.1 mrad and suffers a total horizontal deflection of 7.5 mm (see also Fig. 45). These numbers scale as the inverse of the particle's energy, $1/E$. Therefore, a charged secondary produced in an interaction at $z = -20$ m with an energy of 300 GeV will deviate through 3.4 mrad and be deflected by 23 mm. We can compare this with the numbers for elastic diffractive scattering, where the momentum transfer t is distributed according to $d\sigma/dt \propto \exp(-b|t|)$, with $b \approx 10 \text{ GeV}^2$. The typical value of t is then $\langle |t| \rangle = 1/b \approx \langle p_t^2 \rangle$, so we have $\sqrt{\langle p_t^2 \rangle} \approx 0.32 \text{ GeV}$. Neglecting the focussing magnets for the moment, such a transverse momentum for a 920 GeV proton leads to a separation of 7 mm from the beam over a distance of 20 m. This, and the fact that further upstream the proton vacuum is very good, may explain why elastic scattering plays a relatively small rôle in the generation of the backgrounds in H1.

Proton-carbon events generally have a higher multiplicity than proton-proton interactions (see Figs. 46, 48 and 49) and a significantly higher fraction of the pC events generated in the region $z = -63$ m to $+1$ m leads to some activity within H1 than is the case for pp events (79 % vs. 56 %) or fire a track trigger (41 % vs. 23 %). This can also be seen from Fig. 50. This figure demonstrates that almost all proton-carbon interactions, up to a distance of more than 20 m, generate at least some hits in the H1 detector and also that a large fraction of these events fire the track trigger.

4.3.5 Comparison with Earlier Studies

An earlier study of beam gas interactions was performed in 1987 [7]. Fig. 51 shows two of the most important figures from that study. These show the origin of pion and proton tracks in beam gas events that pass through a disk of radius 1 m at $z = 0$. The primary proton beam-gas vertex distribution used in this study was flat in z up to -110 m. The figures suggest that, with the proper inclusion of magnetic fields, essentially no particles that originate more than 37 m from the IP contribute to beam gas events that are visible in the detector.

However, as Fig. 52 shows, a number of very energetic particles are seen at $z = 0$, and most of the particles at this z value are at very small radii, $r < 6$ cm. This is in agreement with the investigations reported here, which indicate that one important effect is indeed the re-scattering of high energy particles with energies around half the beam energy in the collimators and beam pipe close to H1.

We conclude that our studies are not inconsistent with earlier findings.

¹The absence of a small contribution of very low multiplicity states, i.e. elastic scattering, in the Fritiof pC Monte Carlo is under investigation.

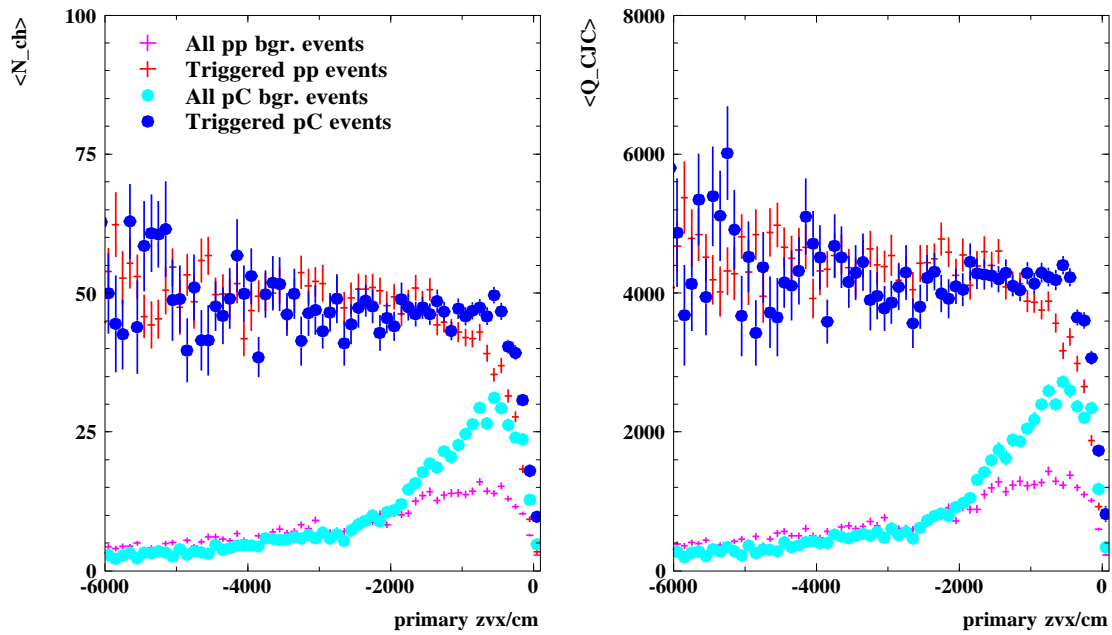


Figure 48: Mean number of tracks (left) and mean deposited charge in the CJC (right) for proton–proton (crosses) and proton–carbon (circles) events as a function of the z position of the primary interaction vertex. For both samples, the values are shown for all events and for track triggered events. The multiplicity from pC interactions is up to about twice that seen following pp interactions if the primary vertex is less than 20 m away from the interaction point, otherwise the event properties are very similar. This can be explained by the fact that for interactions far from H1 only the beam remnant causes the signal within H1, whereas for interactions closer to H1 the target remnant enters the detector.

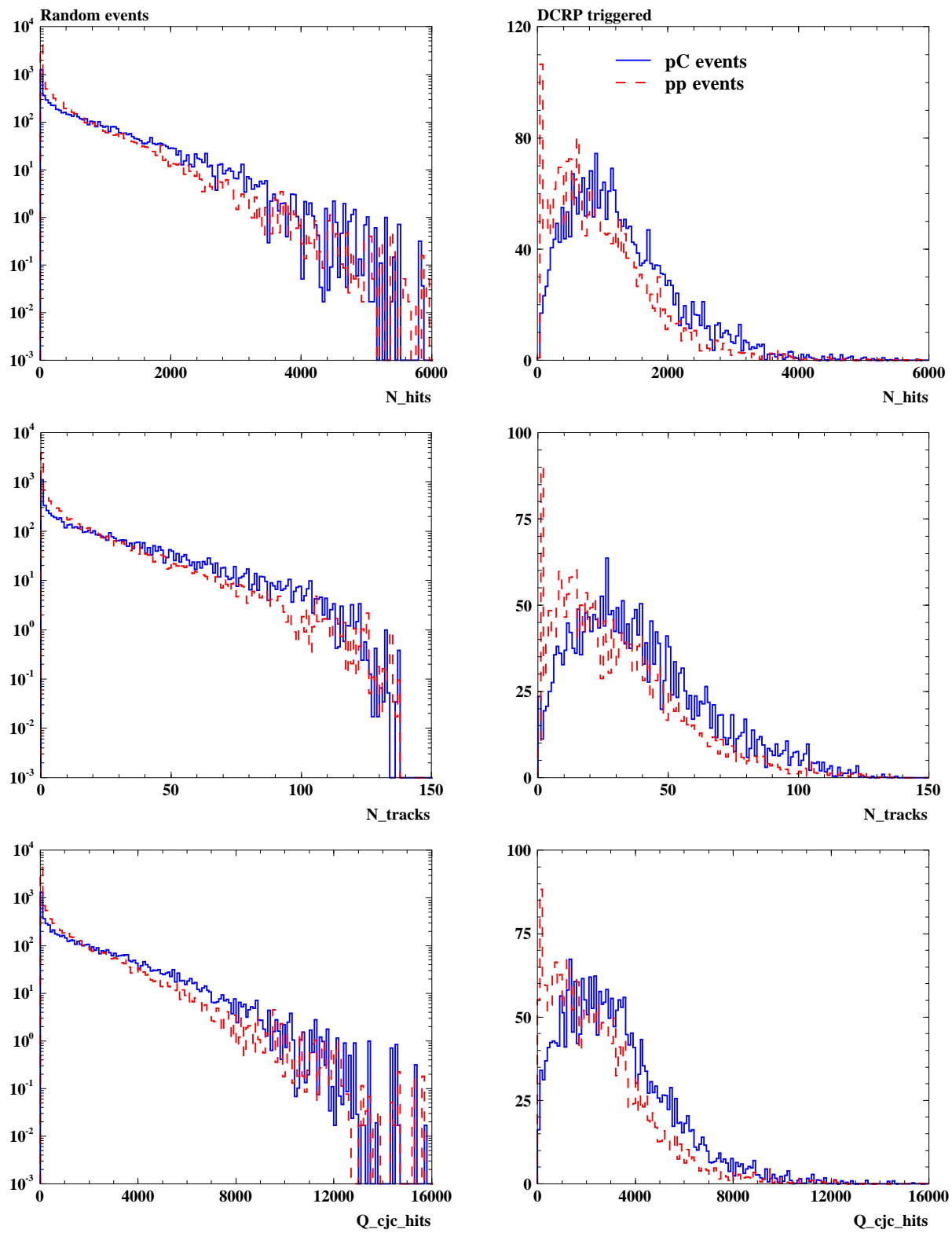


Figure 49: Comparison of proton–proton (dashed line) and proton–carbon (solid line) scattering events: left, all events; right, track triggered events; top, number of hits in the jet chamber; middle, number of tracks; bottom, deposited charge.

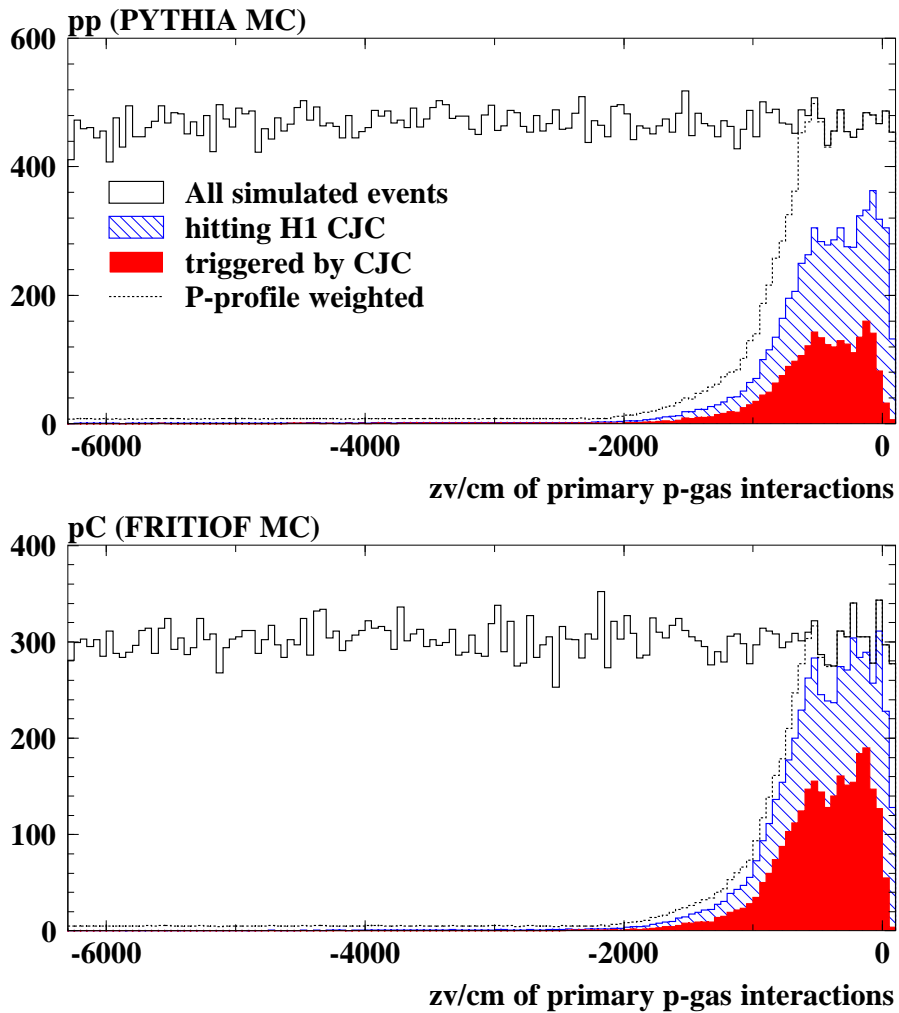


Figure 50: The z vertex of the original beam–gas interaction for events that cause some activity in the H1 detector. The events were generated with a flat z vertex distribution (solid histogram) and re-weighted according to a realistic pressure profile (dashed histogram). Hatched histogram, events with some activity in the CJC; solid histogram, events that fire the track trigger; top, proton–proton interactions; bottom, proton–carbon interactions.

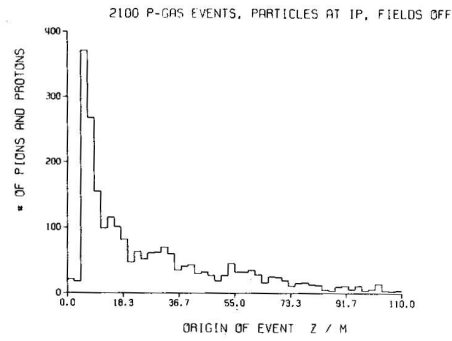


Fig. 3.9 Distribution of origin of tracks for pions and protons from beam gas events passing through a wall at $z = 0$, fields off.

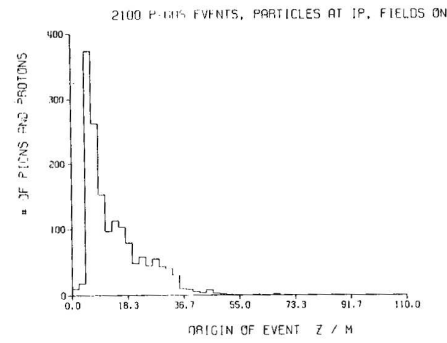


Fig. 3.10 Same as fig. 3.9, fields on.

Figure 51: Figures 3.9 and 3.10 from [7].

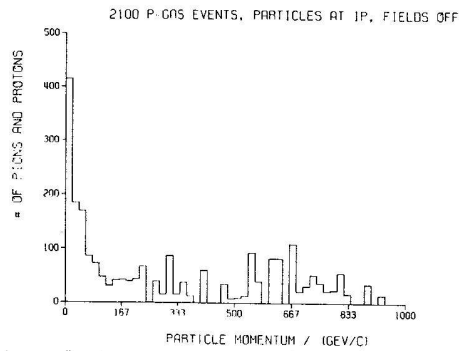


Fig. 3.5 Momentum distribution of pions and protons from beam gas events passing through a wall at $z = 0$, fields off.

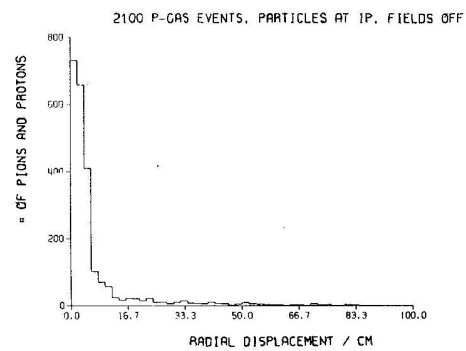


Fig. 3.7 Radial distribution of pions and protons from beam gas events passing through a wall at $z = 0$, fields off.

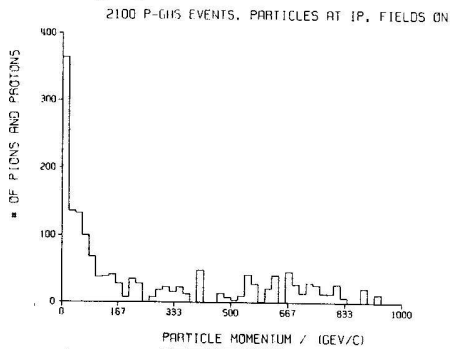


Fig. 3.6 Same as fig. 3.5, fields on.

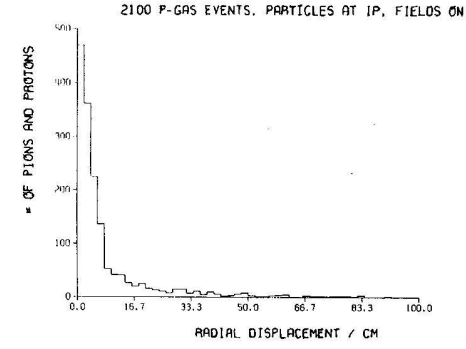


Fig. 3.8 Same as fig. 3.7, fields on.

Figure 52: Figures 3.5 to 3.8 from [7].

4.4 Calculation of the Track Trigger Rate

4.4.1 Normalization of the Monte Carlo Samples

Boyle–Mariott’s law of gases states

$$p \cdot V = NkT,$$

where p is the pressure, V is the volume, N is the number of molecules, T is the temperature and $k = 1.380 \cdot 10^{-23} \text{ J K}^{-1}$ is the Boltzmann constant. For the target density n we get

$$n = \frac{p}{kT} = 2.42 \cdot 10^7 \text{ cm}^{-3} \frac{p/10^{-9} \text{ mbar}}{T/300 \text{ K}} = 2.42 \cdot 10^{-18} \text{ mbarn}^{-1} \text{ m}^{-1} \frac{p/10^{-9} \text{ mbar}}{T/300 \text{ K}}.$$

If the proton–molecule cross section is given by σ_{pA} , then the probability, \mathcal{P} , that an interaction occurs in the residual gas over a given range in z is given by

$$\mathcal{P} = \sigma_{\text{pA}} \int n \, dz = 2.42 \cdot 10^{-18} \text{ mbarn}^{-1} \sigma_{\text{pA}} \frac{\int p \, dz / 10^{-9} \text{ mbar} \cdot \text{m}}{T/300 \text{ K}}.$$

The interaction rate R (in units of interactions per second) per unit z range with a beam of current I is then given by

$$R = \frac{\mathcal{P} \cdot I}{e} = 1.51 \text{ Hz mbarn}^{-1} \text{ m}^{-1} \sigma_{\text{pA}} \frac{(I/100 \text{ mA})(p/10^{-9} \text{ mbar})}{T/300 \text{ K}}.$$

Since it is essentially a black disk, a nucleus of atomic number A has a cross section $\sigma_{\text{pA}} = A^{2/3} \sigma_{\text{pp}}$, where σ_{pp} is the proton–proton cross section, which is about 41.5 mbarn at 920 GeV beam energy. For a molecule, the cross sections of the constituent nuclei have to be summed up: $\sigma_{\text{pA}} = \sum_i A_i^{2/3} \sigma_{\text{pp}}$. Tab. 4 lists the cross sections for a number of gases.

A Monte Carlo sample with N events thus corresponds to a certain time interval $t = N / \int R \, dz$, if the z distribution has been generated according to a given pressure profile with known $\int p \, dz$. Assuming a proton current of 100 mA and a beam pipe temperature of 300 K, we get

$$t = 0.66 \text{ s} \cdot \frac{N}{(\sigma_{\text{pA}}/1 \text{ mbarn}) \cdot (\int p \, dz / 10^{-9} \text{ mbar m})}.$$

For $N = 10^5$, $\int p \, dz = 68 \cdot 10^{-9} \text{ mbar m}$, and $\sigma_{\text{pA}} = 384 \text{ mbarn}$ (for CH_4 , see Tab. 4) one obtains $t = 2.54 \text{ s}$.

4.4.2 The Track Trigger Rate

Using the Monte Carlo simulation described above, one can calculate roughly the expected track trigger rate, here for H1 run 321068 (see Tab. 1). This was a proton only run taken on 30.8.2002 with luminosity optics, a proton current of 50 mA and a beam energy of 920 GeV. The track trigger rate for this particular run was 8.7 kHz and the relevant pressure profile is given in Tab. 5.

We assume that all hydrogen interactions are described by the Pythia pp events, and all interactions with heavier nuclei by the Fritiof model. For the pressure profile from the 30.8.02,

Molecule	$\sum_i A_i$	$\sum_i Z_i^2$	Z_{eff}^2	$\sum_i A_i^{2/3}$	σ_{pA} [mbarn]	R [Hz/m]
H ₂	2.0	2	2.2	2.0	83	125
He	4.0	4	3.0	2.5	104	157
CH ₄	16.0	40	22.6	9.2	384	580
H ₂ O	18.0	66	32.4	8.3	347	523
N ₂	28.0	98	47.7	11.6	482	728
CO	28.0	100	48.4	11.6	481	728
C ₂ H ₆	30.0	78	43.0	16.5	684	1033
O ₂	32.0	128	60.4	12.7	527	796
Ar	40.0	324	132.6	11.7	485	732
CO ₂	44.0	164	78.6	17.9	745	1125
C ₃ H ₈	44.0	116	63.4	23.7	985	1487

Table 4: The total cross section for the interaction of 920 GeV protons with some common gases. A proton–proton cross section of $\sigma_{\text{pp}} = 41.5$ mbarn is assumed. The interaction rate has been calculated for a temperature of $T = 300$ K, a pressure of $p = 10^{-9}$ mbar, a beam current of $I = 100$ mA, and a z range of 1 m. In addition, the summed Z^2 and the effective Z_{eff}^2 (see section on Z^2 determination) for screened molecules are given. These numbers can be compared with the value $Z_{\text{eff}}^2 \approx 23$ that was deduced from the Bethe–Heitler cross section measured with the luminosity system for positron only runs.

given in Tab 5, 23 % of the pp events and 41 % of the pC events lead to a track trigger. With a pressure integral of $\int p \, dz = 30 \cdot 10^{-9}$ mbar · m and a proton current of 50 mA, one arrives at trigger rates between 0.4 kHz for hydrogen and 7.7 kHz for propane, as summarized in Tab. 6. For methane, which could be the dominant component of the residual gas and is reasonably representative of most of the possible gases, the rate is 2.9 kHz. The predicted rate for methane lies a factor of 3.3 below the observed rate. In a later run taken with similar conditions (run 321605) this factor is 1.5 (4.0 kHz measured, 2.7 kHz calculated for methane). Given the uncertainties in the model, this represents very reasonable agreement.

Apart from the gas composition, which can change the predicted rates by up to an order of magnitude, the main uncertainties in the above are the true pressure and temperature of the gas. The pressure is only measured at a few points using the current drawn by getter pumps, which in some places are separated from the vacuum by titanium sublimation pumps. Moreover, the true temperature of the residual gas, which was here assumed to be 300 K, may be much lower. This is particularly true in the cold magnets, where the gas density could increase by a factor of up to 6.

Given these caveats, the most likely components of the residual gas, namely water, methane, nitrogen and hydrogen, can reasonably well explain the observed track trigger rate. The same assumptions allow the description of the bremsstrahlung rate observed in the luminosity system.

4.5 Comparison of Data with Monte Carlo Simulation

Tab. 7 gives an overview of the measured mean numbers of tracks and of hits as well as the measured total charge (in units of 1000 FADC counts, one MIP corresponds to approximately

Date	17.8.02	18.8.02	20.8.02	24.8.02	30.8.02	4.9.02
Time	9:30	3:00	14:30	16:30	3:20	23:50
p current [mA]	25	25	50	30	50	28
e current [mA]	5.5	6.6				
Conditions	Luminosity		Protons only			
Position			Pressure [10^{-9} mbar]			
NR 3.6	6.8	6.7	2.5	4.10	2.8	5.2
NR 6.0	4.5	4.8	2.1	4.00	2.3	4.4
NR 8.3	2.2	2.9	0.67	2.10	1.1	2.0
NR 10.8	1.0	1.4	0.34	0.88	0.49	0.82
NR 21.7	0.17	0.19	0.07	0.07	0.07	0.08
NR 23.6	0.12	0.07	0.07	0.07	0.07	0.12
NR 28	0.05	0.05	0.04	0.04	0.04	0.04
NR 32	0.04	0.04	0.04	0.04	0.04	0.04
NR 36	0.04	0.04	0.04	0.04	0.04	0.04
NR 41	0.09	0.14	0.04	0.04	0.04	0.04
NR 44	0.05	0.08	0.04	0.04	0.04	0.04
NR 46	0.74	0.99	0.04	0.04	0.04	0.04
NR 49	0.04	0.05	0.04	0.04	0.04	0.04
NR 54	0.38	2.43	0.04	0.04	0.04	0.04
NR 57	0.25	0.04	0.04	0.04	0.04	0.04
NR 61	1.8	2.3	0.04	0.65	0.04	0.04
NR 65	0.09	0.10	0.04	0.04	0.04	0.04
NR 70	0.04	0.04	0.04	0.04	0.04	0.04
$\int p dz$ [10^{-9} mbar · m]	66	68	26	45	30	51

Table 5: Pressure profiles as measured at various times and locations. The integrated pressure is calculated from $z = -63$ m to $+1$ m under the assumption that the pressure is constant between $z = -3.6$ m and $+1$ m and between $z = -63$ m and -23.6 m.

Gas	Rate [kHz]
H ₂	0.3
He	1.0
CH ₄	2.9
H ₂ O	2.8
N ₂	4.5
CO	4.5
C ₂ H ₆	5.3
O ₂	4.9
Ar	4.5
CO ₂	6.9
C ₃ H ₈	7.7

Table 6: DCR φ trigger rate predictions for H1 run 321068 (a proton only run with 50 mA of protons at 920 GeV) for various gases assuming that the respective gas is the dominant component. The measured trigger rate was 8.7 kHz.

Sample Triggered	$\langle N_{\text{trk}} \rangle$		$\langle N_{\text{hits}} \rangle$		$\langle Q_{\text{CJC}} \rangle$		$\langle Q_{\text{CJC}} \rangle / \langle N_{\text{hits}} \rangle$	
	all	DCR φ	all	DCR φ	all	DCR φ	all	DCR φ
Data		39.3		1295		2517		1.94
A: pp (Pythia)	10.7	30.6	347	1003	879	2497	2.53	2.49
B: pp, 300 GeV	8.0	25.4	255	822	648	2018	2.54	2.45
F: pC (Fritiof)	21.0	39.1	684	1285	1741	3232	2.55	2.52

Table 7: Raw track and hit multiplicities and total charge in the CJC per event for data and different Monte Carlo samples. The row labelled “triggered” indicates whether the average extends over all events in the sample, or only the track (DCR φ) triggered events.

500 FADC counts) in track triggered (DCR φ) events. The corresponding numbers for all Monte Carlo events (i.e. without trigger requirements) are also given².

The PYTHIA pp simulation predicts significantly fewer tracks and hits per event than are observed in the data, while the Fritiof pC simulation is in good agreement. For the total deposited charge, the PYTHIA simulation seems to describe the data better and the agreement of PYTHIA with the measured track multiplicity also improves as more stringent track selection criteria are applied. It is also observed that there is some interplay between the location of the primary scatter and the signals observed in the detector, making precise statements about the composition of the residual gas from these data difficult.

The confusion with regards to the composition of the residual gas above probably arises at least partly from the complexity of the simulation involved. In order to study this problem more directly, events in a luminosity run with vertex close to the beam line and in the range $|z| < 60$ cm were selected. Rate calculations and investigation of the z vertex distribution, which does not show a peak centred at the nominal interaction vertex, show that the vast majority of these events result from proton beam-gas interactions. The charged multiplicity of these events, as measured in the CJC, is shown in figure 53. This is clearly better described by the Fritiof pC Monte Carlo than by the Pythia or Fritiof pp results. Some indication of the systematic errors associated with this measurement is given by the comparison of the multiplicity predictions from the Fritiof and Pythia Monte Carlos. These are seen to be in reasonable agreement; the mean multiplicity predicted by Pythia for inelastic pp events is 10.8, that predicted by Fritiof is 11.4 and fixed target experiments measure a multiplicity of 10.7 ± 0.7 . The Fritiof prediction for proton-oxygen collisions is also shown in the figure and differs little from the pC results.

A comparison of the mean total charge between samples A and B shows that the Monte Carlo predicts an increase of chamber currents of about 35 % when the proton energy is raised from 300 to 920 GeV. For the proton-only runs summarized in Tab. 1, this would mean that the total chamber current is expected to rise from $45 \mu\text{A}$ at 300 GeV (the pedestal current is $23 \mu\text{A}$) to $53 \mu\text{A}$ at 920 GeV. Unfortunately, the beam was lost after reaching 677 GeV, where a chamber current of $60 \mu\text{A}$ was observed. If one compares to the runs taken on Aug. 29, and corrects for the lower overall current by comparing the 677 GeV runs on both occasions, the prediction for the chamber current at 920 GeV is only $46 \mu\text{A}$, to be compared to the measured current of $62 \mu\text{A}$. It appears that the pp model underestimates the increase of the chamber current with proton energy. It has yet to be verified how the proton-carbon model describes this aspect of the data.

²We have also collected random triggered samples, which can be used to extract numbers for all events, independent of trigger conditions, from data. The analysis of these is not yet complete.

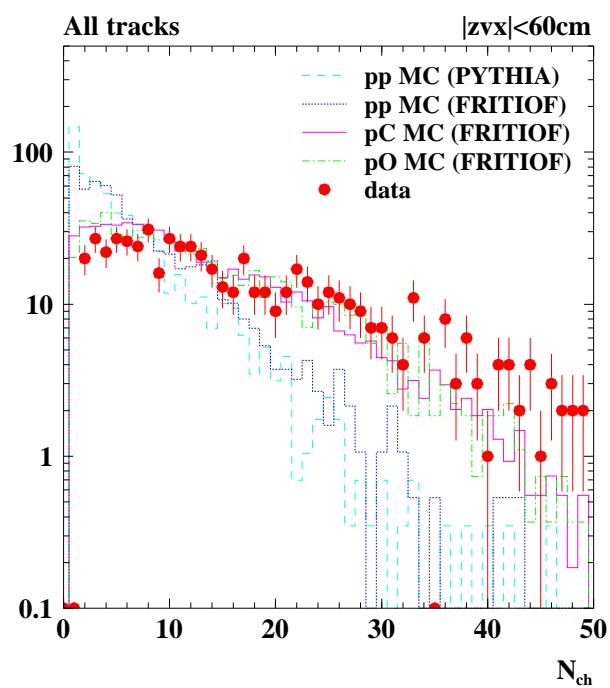


Figure 53: The charged multiplicity, measured in the CJC, of events with vertex close to the beam line and in the region $|z| < 60 \text{ cm}$ compared with the predictions of various Monte Carlo calculations.

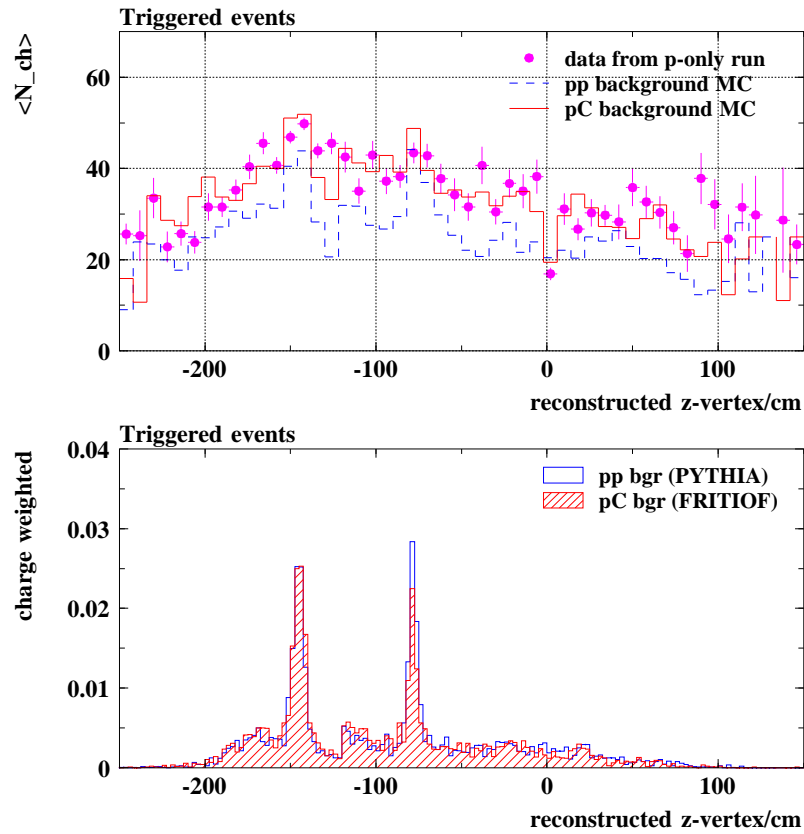


Figure 54: The mean track multiplicity per track triggered event as a function of the reconstructed vertex position and the distribution of the z vertex. The prominent peaks at -80 cm and -145 cm correspond to the synchrotron radiation masks C5A and C5B. The mean track multiplicity of events that originate in these collimators is significantly higher than for average events.

Sample	$\langle N_{\text{trk}} \rangle$	$\langle N_{\text{hits}} \rangle$	$\langle Q_{\text{CJC}} \rangle$
A: Reference	10.7	347	879
C: thinner C5	9.6	306	784
D: ... plus lead	11.4	368	912
E: ... plus C6	12.2	399	973

Table 8: Raw track and hit multiplicities and total charge in the CJC per event for Monte Carlo samples that implement different detector modifications. For sample C, the C5 collimator was reduced in thickness from 20 to 5 mm. For sample D, the lead shielding around C5A and C5B was also implemented, and sample D contains in addition the C6 collimator at $z = -3.6$ m. The reference sample is the same Pythia 920 GeV pp sample as in Tab. 7. These numbers are for all events, thus avoiding trigger bias.

Fig. 54 shows that the mean track multiplicity per event is significantly higher for events that originate in the synchrotron radiation masks C5A and C5B.

Overall, the agreement between data and Monte Carlo is quite good, and the comparisons provide a strong indication that medium-weight nuclei such as carbon, nitrogen and oxygen contribute significantly to the residual gas.

4.6 Effects of Possible Modifications of the Interaction Region

4.6.1 Reducing the Thickness of the C5B Collimator

A thinner C5B collimator slightly improves the background situation as far as the proton induced component is concerned. As Fig. 55 shows, about 40 % of the charge in track triggered events results from events in which particles are scattered from the C5B collimator. Depending on the exact horizontal beam position, the C5A collimator also produces many such events. As shown in Fig. 55, the rate of these in the data is lower than that in the Monte Carlo. This is at least partly due to the fact that the distance between the beam axis and the collimator edge implemented in the simulation is the design value of 11 mm, while the actual value is currently 14 mm.

Using the mean charge per event for all events from Tab. 8, one sees that the proton-induced part of the chamber current is expected to decrease by 11 % following the reduction in the thickness of C5B. This agrees well with the experimental estimate based on the z vertex distribution of the 2.1% of randomly triggered events in which a z vertex is found, shown in Fig. 56. Weighting this distribution according to the charge deposited in the CJC ensures that the area under the C5B peak is a measure of the contribution these events make to the current in the chamber. This is found to be 13% of the total, which is reduced by a factor of 4 if C5B is thinned, leading to a net reduction of about 10% in the proton-induced background.

4.6.2 Additional Lead Shielding around the C5B Collimator

The additional lead shielding that is depicted in Fig. 44 consists of two lead cylinders. One cylinder, with a thickness of 8 mm, is located within the SpaCal ($z = -168$ cm to -152 cm,

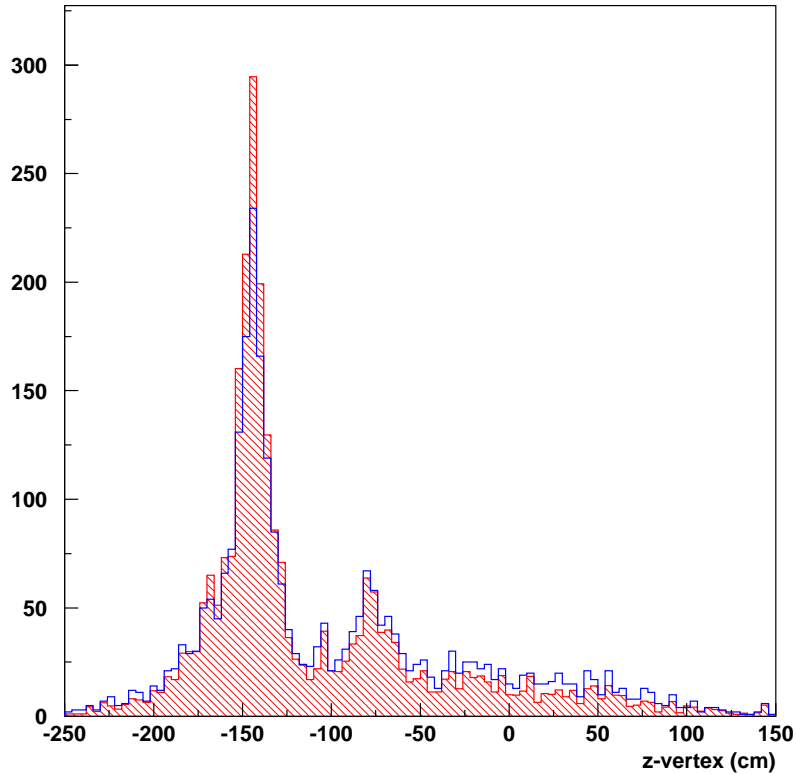


Figure 55: The z vertex distribution for track triggered events in a proton only run (open histogram) and the same distribution weighted according to the charge deposited in the CJC (hatched histogram).

inner radius 7.8 cm), the second, with a thickness of 1 mm, is wrapped around the beam pipe ($z = -152$ cm to -135 cm).

The purpose of this lead shielding is to prevent synchrotron radiation that scatters from the C5A and C5B collimators or “sneaks through” unshielded regions in the BPC area entering the detector. As regards the proton induced background, the lead shielding, in particular that immediately around the beam pipe, increases the chamber current by about 16 %. An optimized design with minimal additional material is needed from the proton background point of view. Shielding of thickness 1 mm is adequate to protect the BST electronics and the CJC, c.f. Fig. 26.

4.7 An Additional Extended Collimator Inside GG

Given the large background induced by proton beam-gas interactions we investigate the possibility of introducing a thick (i.e. long) collimator “C5C”, made of tungsten and extending in z from -3.4 m to -1.8 m. Since tungsten has an interaction length of 2 cm, it is hoped this collimator will completely absorb part of the proton background, thereby reducing the rates in the inner H1 detector. The effect of C5C has been simulated and is illustrated in Fig. 57. The two top figures show the charge induced in the CJC as a function of the vertex position of the proton interaction with beam elements or gas, for all events (crosses) and weighted with the pressure profile (closed circles), without and with C5C, respectively. The bottom figure is the ratio of the pressure weighted distributions. It demonstrates that part of the background can indeed be

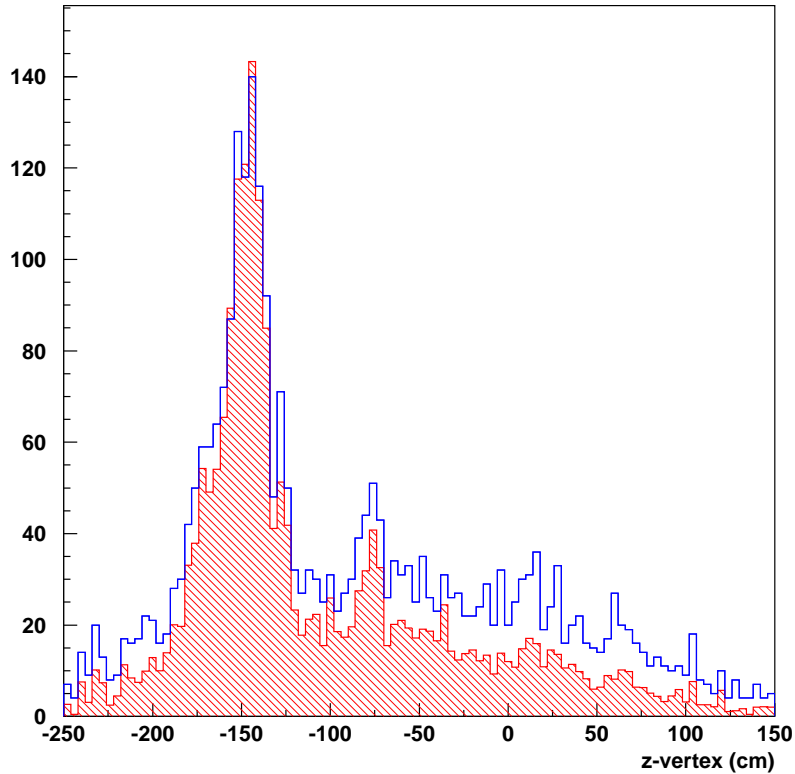


Figure 56: The z vertex distribution for the 2.1% of randomly triggered events in which a z vertex is found (open histogram) and the same distribution weighted according to the charge deposited in the CJC (hatched histogram).

suppressed. The integrated effect amounts to a 35% reduction for a rather tight transverse aperture of $20 \sigma_e$ from the e^+ orbit. The z position, length and aperture of such a collimator require further optimisation.

4.7.1 An Additional Collimator C6 at $z = -3.6$ m

An additional, moveable collimator at $z = -3.6$ m does not, according to the simulations, increase the proton induced background in H1 significantly (in fact, Tab. 8 shows a marginal decrease of 1%). However, the vertical 8.8 mm aperture of such a collimator is very small. Misalignments between the H1 detector and the HERA machine would lead to a drastic increase in the background rate. It is therefore mandatory that the jaws of such a collimator be moveable, by approximately 5 to 10 mm.

The effectiveness of a horizontal collimator is under investigation.

4.8 Summary and Conclusions on Possible Modifications

Proton gas background presently is the major cause of chamber currents in the H1 drift chamber. Extensive studies have been conducted to quantitatively understand this source of background. Although large uncertainties concerning the pressure and composition of the residual gas in the

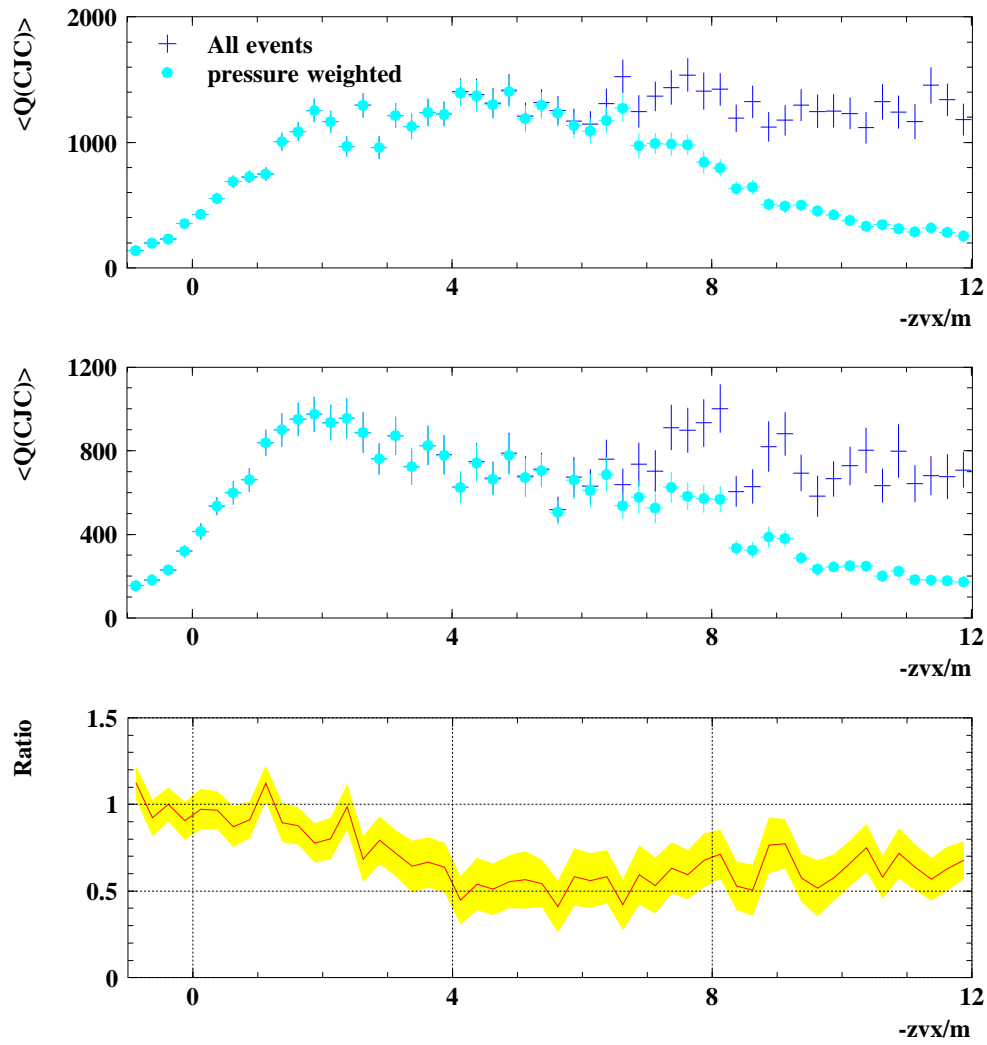


Figure 57: Simulation of the effect of a 1.6 m long tungsten collimator C5C placed at about $z = -3$ m on the charge $Q(\text{CJC})$ which is induced in the drift chamber.

beam pipe remain, Monte Carlo studies show we have a reasonable understanding of proton gas interactions and their effects on the operation of the H1 drift chamber. Monte Carlo and data track trigger rates are in reasonable and track multiplicities in good agreement.

Reducing the thickness of collimator C5B from 20 mm to 5 mm, has been proposed to reduce the proton induced background. This modification is technically feasible and is expected to reduce the proton induced chamber current by about 10 %.

The addition of a new tungsten collimator, C5C, extending from $z = -3.4$ m to $z = -1.8$ m may allow a reduction in the current in the CJC by up to about 35%, but further study of the feasibility of such a device is necessary, including its impact on the conductance of the beam pipe and hence its likely effect on the vacuum at the interaction region as well as the implications for the injection and acceleration procedure.

However, we conclude that the only way to reduce the proton induced background significantly is to improve the vacuum.

Two modifications, the introduction of a new collimator C6 at $z = -3.6$ m and additional lead shielding around the beam pipe in the backward region of the detector, have been proposed in order to reduce the vulnerability of H1 to backscattered synchrotron radiation.

The C6 collimator does not increase the proton induced background significantly, provided its position relative to the beam is correct. This requires that the collimator be moveable, which has the added benefit that it could be retracted in order to increase the aperture for injection.

The addition of 1 mm of lead shielding around the beam pipe increases the probability for the re-scattering of particles from upstream beam gas interactions. The layout studied leads to an increase in the proton induced part of the chamber current by 16 %, but the synchrotron radiation calculations presented above demonstrate that it efficiently shields the detector. We foresee that an optimised version of this shielding will be introduced.

The multiplicity distribution of proton beam-gas events originating close to the beam line in the H1 interaction region suggests strongly that atoms of intermediate weight, such as carbon and oxygen, form a significant proportion of the residual gas in the beam pipe.

5 Chemical Composition of the Residual Gas

5.1 Introduction

Further studies of the chemical composition of the residual gas have been made by measuring the rate of bremsstrahlung off the gas in the beam pipe and, as will be discussed first, using mass spectrometry.

5.2 Mass Spectrum of the Residual Gas

Analogue mass spectra were taken at the H1 pumping stations at 26m NL and 26m NR and used to investigate both the species of molecules and atoms found in the beam pipe and those released by the getter and titanium sublimation pumps, see Fig. 58.

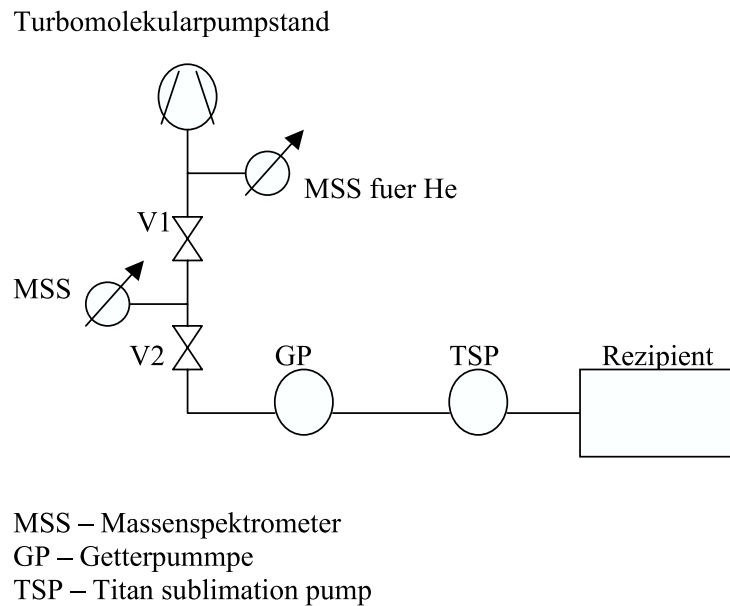


Figure 58: Layout of vacuum pumps.

Additional independent information is available from background rates and event properties in proton only runs (section 4.4) and from beam-gas bremsstrahlung rates as measured in the photon detector in the luminosity system (section 5.3). It should be emphasized that the latter two measurements are sensitive to the beam-gas background during HERA operation, whereas the mass spectra can only be taken while there are no beams in the machine.

The beam gas composition depends on many parameters, including the degree of contamination from internal and external sources. Hydrogen, in particular ionized hydrogen (protons), is highly penetrative and is also produced in dissociation processes, e.g. $\text{H}_2\text{O} \rightarrow \text{OH}^- \text{H}^+$. Nitrogen, oxygen, argon, CO_2 and water are typical “leak markers”, arising from contamination with atmospheric air through flanges, valves or gaskets which are not properly sealed. Large hydrocarbon molecules with atomic masses above 50 to 100 are typically indicative of contamination through lubricants, whereas shorter hydrocarbons with atomic masses below 50 (methane,

ethane, propane) are often indicators of out-gassing from materials such as elastomers. However, such interpretations are hampered by the cracking of large or unstable molecules in the high radiation environment inside the beam pipe and by catalytic chemical reactions. The latter can be important at the titanium sublimation (TSP) and NEG pumps where titanium and other getter materials can act as catalysts. This process is believed to be the main mechanism through which methane is produced in colliders, i.e. via the reaction $CO + 3H_2 \rightarrow CH_4 + H_2O$.

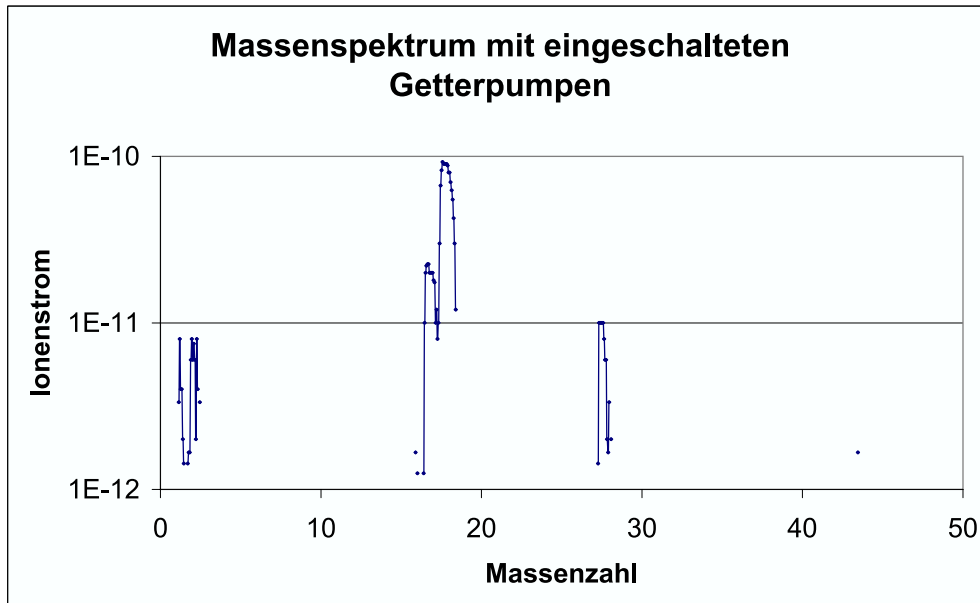


Figure 59: Mass spectrum recorded at 15:44 on 10.7.02 at pump station NL (code NR17). The getter, titanium sublimation and NEG pumps were on at the time the spectrum was recorded. Clearly visible are lines from water (18,17), hydrogen (1,2) and nitrogen (28). The point at 44 amu is probably due to CO_2 .

Mass spectra were taken at both stations (NL and NR) on July 10th and again on September 17th. After starting the turbo molecular and the ion getter pumps, a water line (18 amu) and prominent lines at $A = 16$ (methane), $A = 28$ (N_2 , CO ? ethene?), $A = 44$ (CO_2 , propane? N_2O ?) as well as hydrogen were identified. The initial pressure was measured to be typically 10^{-7} mbar. The mass spectrum measured in July is shown in Fig. 59.

In a second step, after pumping to reduce the residual gas pressure, the cold GO and GG magnets (close to the IA region) within which the beam pipe temperature is typically 50K, were warmed up. As the beam pipe reached a temperature of about 110K (the boiling point of methane) a pressure increase by almost 2 orders of magnitude was registered 26m away from the detector [8]. The molecular masses observed during this procedure are shown as a function of time in Fig. 60. About 1000 seconds after startup, clear evidence is seen for the presence of CH_4 , CH_3 and CH_2 . Another 1000 seconds later C_2H_4 and C_2H_3 (boiling point about 170K) are observed. A little later a peak in the C_3H_8 and C_3H_7 lines shows up. During further warming, more structures are seen which are mainly due to the differing rates at which various regions of the beam pipe warm up, ensuring that the boiling points of the various gases are not reached simultaneously. Out-gassing of water and other materials was found to be at least 2 orders of magnitude below that of the above hydrocarbons. The mass spectra recorded during the warming up of the magnets in September are consistent with those obtained in July,

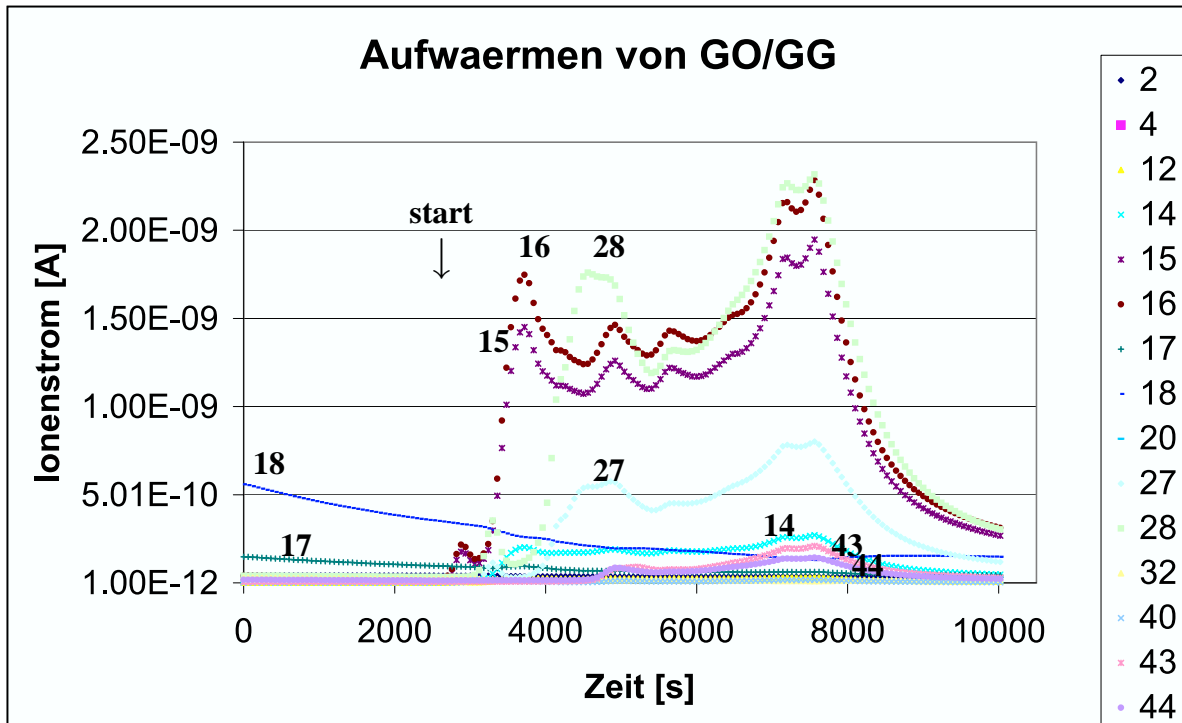


Figure 60: Observed molecular masses as a function of time during the warming up of the GO and GG magnets on September 17th. During the warm up procedure the turbo and ion getter pumps were active.

see Fig. 61. The observed spectra are compatible with the expectations for methane, ethane and propane [9].

During the whole pumping process no indication of contamination with other elements or large molecules was found. The hydrocarbons are believed to be produced catalytically and may freeze out in the cold section of the beam pipe within the GO and GG magnets. Not understood is the source of the carbon, as no convincing evidence for the presence of large amounts of CO or CO₂ was found. The hypothesis that proton-carbon and proton-oxygen scattering are a significant source of background is supported by this analysis, in which the contamination with intermediate mass molecules such as oxygen and carbon was found to be more significant than the contamination with hydrogen. However, the current understanding of the beam-gas composition is not complete. The beam-gas composition is not known during beam operation and the mass spectra were taken far from the interaction point in a low pressure region, whereas the main background comes from the “high pressure” region in the vicinity of the detector.

Measures should be taken to improve the vacuum in the interaction region by installing additional pumps at e.g. 3 m or 10 m. It is likely that hydrocarbons are produced during the pumping process (TSPs) or when firing the NEG pumps. In order to reduce the methane content significantly, frequent pumping with the turbo-molecular and ion getter pumps with warm GO and GG magnets and the installation of more powerful pumps may be necessary.

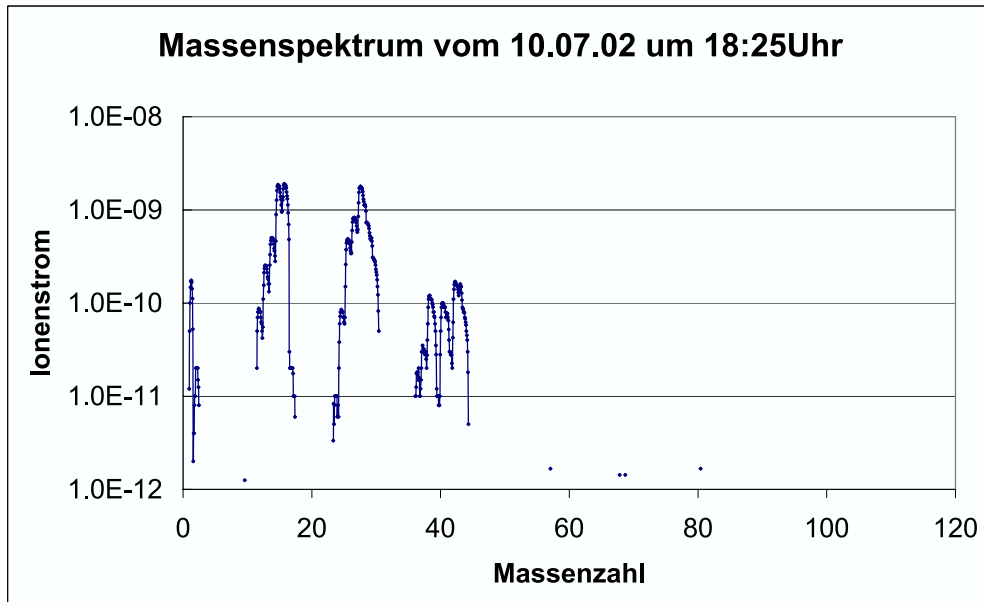


Figure 61: Mass spectrum recorded at 18:25 on 10.7.02 at pump station NL (code NR17). The magnets GO and GG were warmed up prior to the measurement. Hydrocarbons CH_x (masses 12 to 16), C_2H_x (masses 24 to 30) and C_3H_x (masses 36 to 44) are clearly visible. Additional peaks corresponding to hydrogen (masses 1, 2), nitrogen (masses 14, 28), CO_2 (mass 44) and argon (mass 40) are not particularly prominent.

5.3 Effective Z^2 from Beam-Gas Bremsstrahlung Rates

The bremsstrahlung process offers a possible handle on the chemical composition of the residual gas in the beam pipe since the cross-section for this process is roughly proportional to the square of the atomic number, Z^2 .

The detection rate $R^{(i)}$ of photons with energy above E_{\min} in the luminosity detector for the electron pilot bunch i is given by

$$R^{(i)} = \frac{1}{e} I_e^{(i)} \int \sum_j n_j(z) \sum_m s_m(j) \sigma(E_{\min}, Z_m) \mathcal{A}(z) dz,$$

where

$I_e^{(i)}$:	bunch current
e :	elementary charge.
z :	longitudinal orbit coordinate.
$n_j(z)$:	number density of the j -th component of the residual gas.
$s_m(j)$:	number of atoms of nuclear charge Z_m in a molecule of component j .
$\sigma(E_{\min}, Z_m)$:	integrated cross-section for emission of bremsstrahlung photons. with $E > E_{\min}$ from electrons of energy E_0 on nuclei of charge Z_m .
$\mathcal{A}(z)$:	geometrical acceptance of the luminosity detector.

Assuming that the chemical composition of the residual gas does not depend on z , the volume density is given by:

$$n_j(z) = \frac{p_j(z)}{kT(z)} \approx \frac{p_j(z)}{p(z)} \frac{p(z)}{kT(z)} = f_j \frac{p(z)}{kT(z)},$$

where

p_j :	partial pressure of the residual gas component j .
f_j :	molar proportion of the residual gas component j .
$p(z)$:	residual gas pressure profile.
$T(z)$:	residual gas temperature profile.
k :	Boltzmann constant.

The Z dependence of the cross-section for the bremsstrahlung process varies as a function of the degree of ionisation of the residual gas molecules or atoms, because the nuclear electrostatic potential is screened by the shell electrons. Scattering on the shell electrons themselves is also taken into account [10–14].

We consider the two extreme cases of no screening (full ionisation) and complete screening (no ionisation). In the first case, the cross-section is strictly proportional to Z^2 , whereas for the second it is, to very good approximation, proportional to $Z^2 \cdot \log(184.15Z^{-1/3}) + Z \cdot \log(1194Z^{-2/3})$.

Therefore, we factorise the cross-section as follows:

$$\sigma(E_{\min}, Z) = \varphi(Z) \cdot \bar{\sigma}(E_{\min}),$$

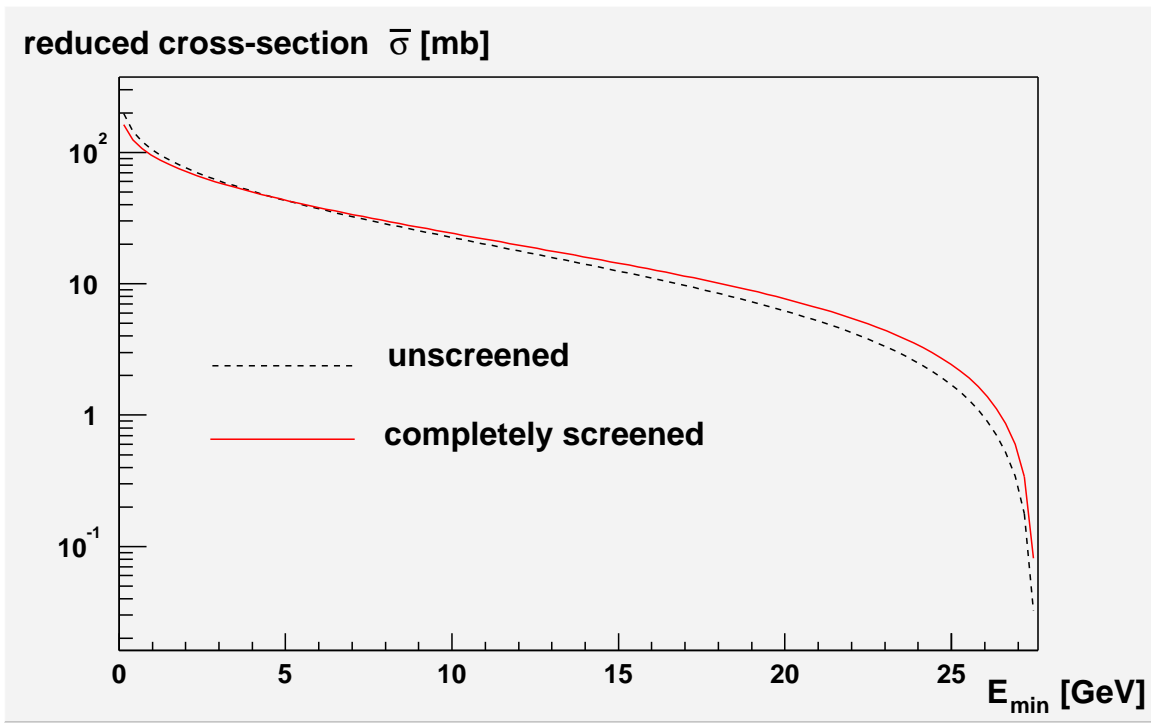


Figure 62: The reduced Bethe-Heitler cross-section as a function of E_{\min} .

where the charge coefficient is defined as $\varphi(Z) = Z^2$ for unscreened ions, and for neutral atoms as:

$$\varphi(Z) = (Z^2 \cdot \log(184.15Z^{-1/3}) + Z \cdot \log(1194Z^{-2/3})) / (\log(2E_0/m_e) - 1/2).$$

The extra factor $(\log(2E_0/m_e) - 1/2)^{-1}$ has been introduced so that the reduced cross-sections $\bar{\sigma}$ have almost the same value for the unscreened and the completely screened nuclei. Figure 62 shows the reduced cross-sections for both cases as a function of E_{\min} .

For molecules the atomic charge coefficients have to be weighted according to the composition of the molecule:

$$\tilde{\varphi}_j = \sum_m s_m(j) \varphi(Z_m).$$

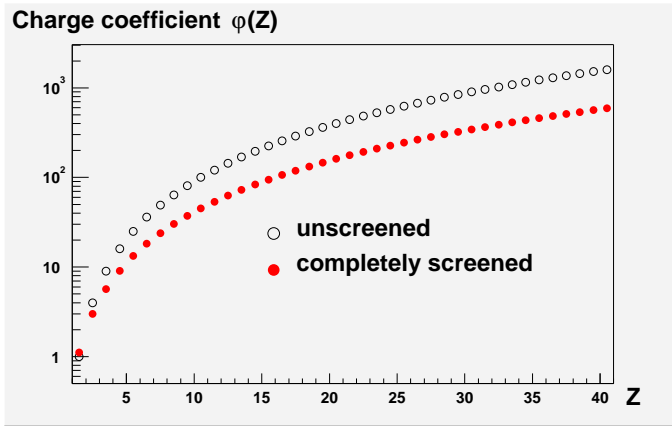
Figure 63 shows the charge coefficients for the elements and for several gases in the screened and unscreened cases.

With these approximations, the bunch rate can be expressed as follows:

$$R^{(i)} = \frac{1}{e} I_e^{(i)} \bar{\sigma}(E_{\min}) Z_{\text{eff}}^2 \int \frac{p(z)}{kT(z)} \mathcal{A}(z) dz,$$

where the effective charge squared Z_{eff}^2 is defined as:

$$Z_{\text{eff}}^2 = \sum_j f_j \tilde{\varphi}_j.$$



	unscr'd	screened
H ₂	2.00	2.22
He	4.00	2.99
CH ₄	40.00	22.62
H ₂ O	66.00	32.43
C ₂ H ₄	76.00	40.80
C ₂ H ₆	78.00	43.02
N ₂	98.00	47.67
CO	100.00	48.40
O ₂	128.00	60.43
CO ₂	164.00	78.61
Ar	324.00	132.63

Figure 63: Charge coefficients for the elements and various gases.

date	time	run	I_e^{TOT} [mA]	$I_e^{\text{e-pilot}}$ [mA]	R^{TOT} [kHz]	$R_e^{\text{e-pilot}}$ [kHz]	$[10^{-10} \text{ mbar}]$				$ekR/I_e\bar{p}$ [mb m / K]	Z_{eff}^2
							$PL_{5.1}$	$PL_{5.8}$	$PR_{3.6}$	$PR_{6.0}$		
11/09/02	01h43	e ⁺	20.25	20.25	11.6	11.6	1.3	5.5	87	62	14.5	26.9
11/09/02	12h43	e ⁺	6.38	6.38	2.3	2.3	1.8	8.8	74	63	10.8	20.0
12/09/02	04h00	e ⁺	9.48	9.48	3.9	3.9	1.7	7.8	68	53	13.4	24.8
12/09/02	15h30	e ⁺ p	8.17	0.56	320	0.35	1.3	5.8	95	59	14.6	27.0
12/09/02	16h22	e ⁺ p	7.62	0.53	297	0.33	1.3	5.9	86	60	16.1	29.8
13/09/02	07h32	e ⁺ p	14.1	10.4	99.7	5.59	0.69	2.8	72	49	16.5	30.5
13/09/02	12h55	e ⁺ p	8.44	6.19	49.9	2.67	1.05	4.4	72	51	13.3	24.6

Table 9: Beam parameters, beam-gas rates, vacuum conditions and calculated effective Z^2 for selected runs in September 2002.

In the absence of precise knowledge about the pressure and temperature profiles $p(z)$ and $T(z)$, it is reasonable to assume uniform distributions with average pressure and temperature values of \bar{p} and \bar{T} . The remaining integral over the geometrical detector acceptance can be considered as an effective length L_{eff} of the section of the orbit that is visible in the luminosity detector. With these approximations the effective charge can be calculated from the measured bremsstrahlung rate, residual gas pressure and electron beam current:

$$\begin{aligned}
 Z_{\text{eff}}^2 &= \frac{ekR^{(i)}\bar{T}}{I_e^{(i)}\bar{p}L_{\text{eff}}\bar{\sigma}(E_{\text{min}})} \\
 &\approx 2212 \cdot \frac{ekR^{(i)}[\text{kHz}]\bar{T}[\text{K}]}{I_e^{(i)}[\text{mA}]\bar{p}[10^{-10}\text{mbar}]L_{\text{eff}}[\text{m}]\bar{\sigma}(E_{\text{min}})[\text{mb}]}.
 \end{aligned}$$

Note that the effective Z^2 is the same for the unscreened and the screened cases since this difference has been carried over entirely to the charge coefficients.

Assuming the nominal positron beam divergence, the geometrical acceptance \mathcal{A} of the luminosity detector is limited by the beam pipe and the exit flange and has its maximal value of 97.5% for a positron orbit tilted by 0.15 mrad towards the outside of the ring. At present, the nominal beam orbit realizes this tilt.

For bremsstrahlung photons emitted in the straight section between $z = -2\text{m}$ and $z = +1.95\text{m}$ this maximal acceptance is assumed. For the curved parts of the orbit, only photons emitted not further than $\approx 24\text{cm}$ inside the cold magnets can be detected in the luminosity detector. The acceptance for the curved part is calculated as an average over the acceptance and contributes only 2% to the total effective length, $L_{\text{eff}} = 3.93\text{m}$.

gas composition	unscr'd	screened
Ar/CH ₄	–	3/97
Ar/H ₂	7/93	18/82
CO ₂ /CH ₄	–	6/94
CO ₂ /H ₂	15/85	31/69
CO/CH ₄	–	13/87
CO/H ₂	24/76	51/49
N ₂ /CH ₄	–	13/87
N ₂ /H ₂	25/75	52/48
C ₂ H ₄ /CH ₄	–	19/81
C ₂ H ₄ /H ₂	32/68	62/38
H ₂ O/CH ₄	–	34/66
H ₂ O/H ₂	38/62	79/21

Table 10: Chemical composition (volume percentages) of the residual gas for $Z_{\text{eff}}^2 = 26$ in a two-component model derived using unscreened and completely screened charge coefficients.

Table 9 shows a selection of measured values of the bremsstrahlung rate, residual gas pressures and electron beam current for several runs (e⁺ only and e⁺p). The pressures measured in the four pumps closest to the interaction point (IP) are listed. The ratios $ekR/I_e\bar{p}$ for these runs all lie in the range (11-15 mb m/K). This indicates that the different measurements are consistent and that typical variations of the beam conditions have little influence on the effective Z^2 .

The determination of Z_{eff}^2 depends on the assumptions made regarding the p and T profiles. Throughout, we assume a uniform temperature profile at 313 K which corresponds to the typical temperature of the beam pipe in the warm section of the IR, as well as a uniform pressure profile at the value measured at $z = -3.6\text{m}$ (to the right of the H1 IP). In fact, in the straight section around the IP one expects a worse vacuum than at $z = -3.6\text{m}$.

The reduced integrated cross-section is calculated for $E_{\text{min}} = 5\text{GeV}$, which corresponds to the energy threshold above which photons are counted. Its numerical value is 42.9 mb (43.1 mb) for full (no) screening of the nucleus.

If one wants to interpret a particular value of Z_{eff}^2 in terms of the chemical composition of the residual gas, one has to take into account the particular values of the molecular charge coefficients.

Assuming a two-gas mixture, one component has to have $\varphi_j > Z_{\text{eff}}^2$ and the other $\varphi_j < Z_{\text{eff}}^2$, where the proportion of the components is uniquely determined.

The most likely component of the residual gas in the range of observed values of Z_{eff}^2 is methane. The average Z_{eff}^2 of 26 can be reproduced by a two-gas mixture with a dominant methane component, assuming full screening. Alternatively, gas mixtures with a large hydrogen component and a smaller heavier component (CO, N₂, CO₂ . . .), at the level of several tens of percent, are also allowed (c.f. table 10).

An argon component can be accommodated by the model, as can heavier noble gases, however only as a minor component at a level of 20% (3%) in hydrogen (methane).

In the case of full ionisation, which is generally considered less likely, one would tend to model the residual gas as a mixture of hydrogen and heavier components at the level of 10% to 40%. An argon contribution would then be even more disfavoured.

Conversely, if one assumes that the residual gas is composed entirely of methane, one can derive an average pressure around the IP which is typically about 10% to 40% higher than at $z = -3.6\text{m}$.

5.4 Summary

The previous evidence that atoms of intermediate weight such as carbon and oxygen form a significant proportion of the residual gas in the beam pipe is supported by both the mass spectra of the gas measured at some distance from H1 and the rate of bremsstrahlung off that gas measured within the H1 interaction region.

6 Conclusions

Following the HERA luminosity upgrade, high beam-related backgrounds in the collider experiments ZEUS and H1 have restricted HERA operation to low positron and proton currents (I_e and I_p , respectively). The limit for safe operation of the H1 detector with the conditions pertaining in mid-September 2002 is given approximately by $I_e \cdot I_p \leq 600 \text{ mA}^2$. Larger beam currents cause the currents drawn in the central outer drift chamber (CJC2) to rise beyond the tolerable limit of $150 \dots 200 \mu\text{A}$ and the rate in the silicon pad detector (radiation monitor) to exceed its safe limit of about 50 kHz. Presently, the maximum integrated luminosity that may be taken in a month with the H1 detector is of the order of a few pb^{-1} .

The behaviour of the CJC currents was studied in great detail in HERA runs with single positron and proton beams and during ep collisions. These currents were found to be primarily due to the effects of synchrotron radiation, positron beam-gas and proton beam-gas interactions. Extrapolation to the anticipated HERA-II beam currents of $I_{e,max} = 55 \text{ mA}$ and $I_{p,max} = 135 \text{ mA}$ leads to an estimated current of about 1 mA in the CJC2, nearly 90% of which is due to proton initiated background. Similarly, the radiation monitor rate, when extrapolated to the design beam currents, is about 400 kHz whereas a rate of 50 kHz is expected from the positron beam alone.

Various measures have been investigated to reduce the backgrounds. Backscattered synchrotron radiation is estimated to cause a current of about $60 \mu\text{A}$ in the CJC2 at $I_{e,max}$. As discussed in this report, coating of the absorber at 10.8m is expected to reduce the effects of this background by a factor of 1.8. As a further measure to protect the silicon detector and CJC, H1 is considering installing 1 mm of lead shielding around the beam pipe in the region $-150 < z < -70 \text{ cm}$.

During luminosity running, the dominant backgrounds are induced by proton beam-gas interactions. The rate of these depends on the pressure in the beam pipe, which is observed to increase with the positron current. Detailed Monte Carlo studies have led to a quantitative understanding of the background production mechanism, namely the re-scattering of particles produced in proton beam-gas interactions in the material of the beam line. The charged multiplicities measured in the CJC and the bremsstrahlung rate, measured in the H1 luminosity detector, suggest that atoms heavier than hydrogen ($Z \simeq 6$) form a significant proportion of the beam gas. This conclusion is supported by the mass spectra of the beam gas measured at some distance from H1. Reduction of the proton initiated background rate to tolerable levels requires an improvement of the vacuum at full beam currents by a factor of about 5 with respect to the conditions pertaining in mid-September 2002. This improvement is required both around the interaction region and extending upstream to z of at least -12 m. A further relatively small improvement may be possible through the introduction of a proton beam-gas collimator.

A fraction of up to about 10% of the current drawn by the CJC can be attributed to re-scattering in the C5B collimator at $z = -145 \text{ cm}$ (measured in random trigger runs and calculated in the proton background simulation). Adequate shielding of the backscattered synchrotron radiation is achieved if C5B has a thickness of 5 mm, reduced from its present value of 2 cm. The collimator C5A is not observed to contribute significantly to the background rate in the data.

A substantial improvement of the vacuum in the region of the H1 detector and a reduction in the rate of the backscattered synchrotron radiation are required before the H1 detector can be operated at the maximum currents envisaged for HERA II.

References

- [1] W. Blum, L. Rolandi, “Particle detection with drift chambers”, Berlin, Germany, Springer (1993) 348 pages.
- [2] C. Niebuhr, “Ageing effects in the Central Jet Chamber of the H1 Experiment”, Proc. of the International Workshop on Ageing Phenomena in Gaseous Detectors, DESY, Hamburg, Germany, Oct. 2001, to be published in NIM A.
- [3] D. Pitzl “Abschirmung der HERA Detektoren gegen Synchrotronstrahlung”, Diploma thesis, University of Hamburg, 1987.
- [4] A. Meseck, “The electron distribution in HERA and consequences for the H1 detector after the luminosity upgrade”, p.50, Ph.D. thesis, Hamburg, 2000.
- [5] T. Sjöstrand *et. al.*, Comput. Phys. Commun. **135** (2001) 238.
<http://www.thep.lu.se/~torbjorn/Pythia.html>
- [6] H. Pi, Comput. Phys. Commun. **71** (1992) 173.
<http://wwwinfo.cern.ch/asd/cernlib/mc/fritiof.html>,
<http://www-pat.fnal.gov/mcgen/fritiof/fritiof.html>
- [7] R. Brinkmann, “Simulation of Background from Proton Losses in the Hera Straight Sections”, DESY-HERA-87-19.
- [8] J. Schaffran, “Strahlvakuum Betrachtung der Region HERA (Nord)”, unpublished internal report 15.7.02.
- [9] Ch. Falland, “Mass table for rest-gas analysis”, DESY-H-4 unpublished internal report 22.1.70.
- [10] H.A. Bethe and W. Heitler, Proc. Roy. Soc. **A146** (1934) 83.
- [11] Landau, Lifshitz and Pitajewsky, “Quantum Field Theory. Theoretical Physics IV”.
- [12] W. Heitler, “The Quantum Theory Of Radiation”, London and New York (Oxford Univ. Press) 1944.
- [13] Y.-S. Tsai, Rev. Mod. Phys. **46** (1974) 815.
- [14] S.M. Seltzer and M.J. Berger, Nucl. Instr. Meth. **B12** (1985) 95.